Implementation of the Quantum Hall Effect Based Precision Resistance Measurement System

By

Mporome Brian Maboko

Supervisor:

Assoc. Prof. Mark Blumenthal

A dissertation submitted to the Faculty of Science in fulfilment of the requirements for the Degree in

Master of Science

Department of Physics

University of Cape Town

2019

Plagiarism and Declaration

I, Maboko Mporome Brian, hereby declare that all the information submitted by me in this thesis is correct, true and valid.

Acknowledgments

I had the chance to work with some of the most amazing people on earth and in this section, I'm expressing my gratitude for their support during my Masters. Both here at University Cape Town (UCT) and at National Metrology Institute of South Africa (NMISA), it was wonderful.

Firstly, I would like to thank NMISA for financial support and the amazing opportunity to study such interesting physics. I thank my two supervisor's Mark Blumenthal for the guidance in research and Alexander Matlejoane for all training and support in metrology measurements. They have been a blessing over these past few years. And not forgetting Michael Khoza and Marcus Hlakola who helped me with questions that I was battling with, when it comes to metrology.

Secondly, I would like to thank my family for all the love and support they have given me throughout the years. I thank my sisters, Lerato, Puseletso and Dineo, for being able to encourage me about doing my research. I thank my little sister and niece, Rethabile and Boiketlo for the best times I laughed with them, it helped a lot in fighting stress due to research.

I thank my two mothers Anna and Glenda for encouraging me, telling me that I can make it no matter what. I thank my dad Fanie for being a good role model and always telling me, I can win in life so long as I'm focusing on the goal. I also give thanks to the Southern suburbs family for the best times we had altogether, I enjoyed every outing with them.

Finally, I would like to express gratitude to God for the strength he gave me all these years. Even though those bad and worst days, I managed to pull through against all the odds.

Dedication

This thesis is dedicated to the memory of my dearest mother. Whom I never had a chance to meet, but I always carry her spirit with me and to my father who taught me to work hard, even during difficult days I kept moving forward. May their souls rest in mighty peace. I hope I have made them proud thus far.

Abstract

The integer Quantum Hall Effect (QHE) occurs when a two-dimensional electron gas (2DEG) is subjected to a strong perpendicular magnetic field and when the system is cooled to low temperatures. The QHE harbours a wealth of unique phenomena. Of interest is the existence of the Quantum Hall Resistance (QHR) which had found to be related to two fundamental constants of nature via the von Klitzing constant $\frac{h}{e^2}$, where e is the charge of the electron and h Planck's constant. This thesis investigates the properties of the QHE in a low dimensional electron gas system. The von Klitzing constant is determined as well as the electron density n_{2D} and mobility μ of the material measured. The results are compared to the accepted value of the von Klitzing constant as determined by the metrological community. The average von Klitzing constant obtained is $25\,783.637\,\Omega$ within an accuracy of 1.13×10^{-12}. Our results are further interpreted using the Landau quantum mechanical model of electron transport in perpendicular magnetic field.
The measurement of standard resistances utilising a standard DC resistance measurement system were also undertaken at the National Metrology Institute of South Africa (NMISA). This ties in with the ongoing project of NMISA to develop an in-house quantum Hall measurement system to provide the full traceability for resistance standard measurements in the Republic of South Africa.

The device measured utilised a GaAs/AlGaAs heterostructure structure, grown via Molecular Beam Epitaxy (MBE). A micron sized Hall bar with Ohmic contacts was patterned using standard clean room procedures. Magnetotransport measurements at low temperatures, sub 200 mK were carried out on the device. The transverse and longitudinal resistances were obtained and plotted against the perpendicular magnetic field. Quantum Hall plateaus and Shubnikov de-Haas (SdH) oscillations were observed. Properties of the heterostructure such as the electron density (n_{2D}) and mobility (μ) were determined. The n_{2D} obtained was $2.27 \times 10^{11}\,\mathrm{cm}^{-2}$ with μ at $3.5 \times 10^{5}\,\mathrm{cm}^{2}\mathrm{V}^{-1}\mathrm{s}^{-1}$. All results were compared to current literature values.

Contents

List of Figures

List of Tables

List of Symbols

List of Acronyms and Abbreviations

AES ..... Auger Electron Spectroscopy

CHE ..... Classical Hall Effect

CIPM ..... International Committee of Weights and Measures

ESDM ..... Experimental Standard Deviation of the Mean

GPIB ..... Hewlett-Packard Interface Bus

IEC ..... International Electrotechnical Commission

IEEE ..... Institute of Electrical and Electronic Engineers

ISO ..... International Organization of Standardization

JE ..... Josephson Effect

LCC ..... Leadless Chip Carrier

LEED ..... Low-Energy Electron Diffraction

LIA ..... Lock-In Amplifier

MIL ..... Measuremnt International Limited

MOCVD ..... Metal-Oxide Chemical Vapour Deposition

MOSFET .... Metal-Oxide Semiconductor Field-Effect Transistor

NMISA ..... National Metrology Institute of South Africa

PDF ..... Probability Density Function

PTB ..... Physikalisch-Technische Bundesanstalt

PRT ..... Platinum Resistance Thermometer

QMT ..... Quantum Metrology Triangle

QHE ..... Quantum Hall Effect

QHR ..... Quantum Hall Resistance

RHEED ..... Reflection High-Energy Electron Diffraction

SANAS ..... South African National Accreditation System

SdH ..... Shubnikov-de Haas

SET ..... Single Electron Transport

SIMS ..... Secondary-Ion Mass Spectroscopy

2DEG ..... Two Dimensioanl Electron Gas

UBM ..... Uncertainty Budget Matrix

UCT ..... University of Cape Town

UHV ..... Ultrahigh Vacuum

XPS ..... X-ray Photoelectron Spectroscopy

Chapter Summary

A concise summary of the chapters details in the thesis is given below.

Chapter 1 Introduction

In this chapter, we introduce the field of metrology. The quantum metrology triangle (QMT) is discussed in connection with the three quantum effects which obey Ohm's law with an uncertainty of 10^9 amongst them. We discuss the Josephson effect, responsible for the voltage standard and look into the ongoing research for the electrical current (Ampere) standard via single-electron transport (SET) devices. Finally, the quantum Hall effect (QHE) which is our focus will be discussed.

Chapter 2 Literature Review

The physics of semiconductor heterostructures and two-dimensional electron gas (2DEG) is discussed. Band-gap, modulation-doping of semiconductor materials and an introduction of molecular-beam epitaxy (MBE) are also given. The behaviour of electrons in a magnetic field which leads to Landau levels is included. Finally, the theory of the two quantum effects namely: the quantum Hall plateaus and the Shubnikov-de Haas oscillations are analysed.

Chapter 3 Sample Fabrication

This chapter focuses on the design and fabrication of the device used in this thesis. A brief description of fabrication processes is given. A photograph of the final device fabricated is presented.

Chapter 4 The ^{3}He/^{4}He Dilution Refrigerator and Experimental Setup

This chapter contains details about the dilution refrigerator used for data acquisition. Information about the measurement setup is included with a schematic diagram.

Chapter 5 Device Measurements and Results

This chapter details the experimental results. The obtained results of the quantum Hall plateaus are analysed and compared with literature values, while the electron density and mobility obtained from the Shubnikov-de Haas oscillations were compared with other wafers

to check the behaviour of our wafer.

Chapter 6 NMISA DC Resistance Measurement System and Measurements

This chapter details the techniques currently used at NMISA for standard resistor calibrations and dissemination. Calibrations were carried out and analyses for resistance values, drift rate per day/month, stability due temperature were reported. Temperature coefficients measurements were carried out and the values obtained were compared to the ones on the air standard resistors.

Chapter 7 Conclusion and Suggestion of Future Work

This chapter provides observations made during the study period and answering of the research questions. It conveys what we wish to do in the future to further study this amazing phenomenon. Graphene samples which are capable to allow the observation of the QHE are discussed and the cryogenic current comparator (CCC).

1 | Chapter 1: Introduction

This chapter gives a brief description of the background in metrology and quantum metrology. The Josephson Effect (JE), Single Electron Transport (SET) and the Quantum Hall Effect (QHE) will be introduced. In this project, we will focus more on the QHE due to our interest in the Quantum Hall Resistance (QHR) standard. Other sections cover the foundations required to understand metrology and its science, the sections are as follows: 1.1 Introduction to Metrology, 1.2 Quantum Metrology Triangle (QMT), 1.2.1 The Quantum Hall Effect (QHE), 1.2.2 The Josephson Effect (JE), and 1.2.3 Current standard.

1.1 Introduction to Metrology

Metrology is the science of accurate measurements, it includes all theoretical and experimental characteristics where the uncertainty of measurement results are investigated. A simple picture illustrating how measurements in metrology are accomplished is shown in figure 1.1. Measurements in metrology consist of comparing the unknown standard (or unit under test) A_x of a quantity with a reference standard A_{ref} [52]. When nations started trading or exchanging goods with one another metrology was born. They had to agree on standards to be used for trade. Measurement infrastructures *i.e.* the Nippur cubit and the Royal cubit are some of the examples that were used for measurement of length. Over time more than 30 standards for length were used in different countries and about 50 different standards for mass were available. This, during the eighteenth century made trading amongst nations much more complicated.

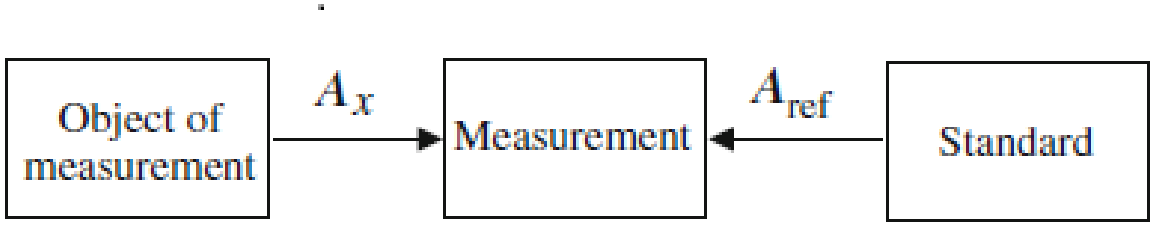

Figure 1.1: Comparison between object and standard [52].

In 1791 the French National Assembly decided on an initiative to redefine trading scales in an attempt to improve the ease and reliability in trading. The field of metrology has worked

to improve the accuracy, reliability and ease of use of all global standards.

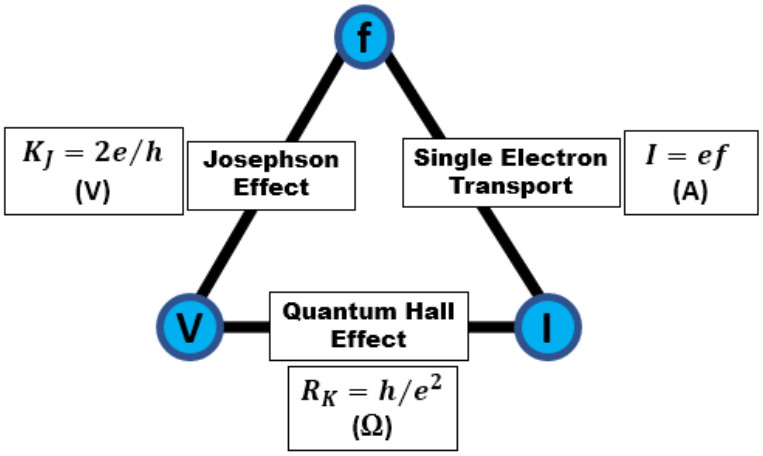

Figure 1.2: Schematic diagram of the Quantum Metrology Triangle illustrating the three quantum effects used to define SI Units Volt, Ohm and Ampere. The representation of Ampere is yet to be formally realised.

1.2 Quantum Metrology Triangle (QMT)

The Quantum Metrology Triangle (QMT) is shown in figure 1.2. Via Ohm's law and using the three-electrical quantum effects; the Josephson effect (JE), the Quantum Hall effect (QHE) and the electrical current standard based on Single-Electron Transport (SET), all three vertices are defined in terms of fundamental constants of nature, the Planck constant h and the electron charge e. Researchers are trying to achieve based on experiments of electron pumps, a standalone current standard. With the application of the fundamental constants an uncertainty of 1 part in 10^9 or better, is expected. A brief description of the three phenomena is discussed below. The ultimate goal is to combine the three quantum effects, and the relevant constants R_H, K_J and Q_X, via Ohm's law to close the quantum metrological triangle within a total uncertainty of the order of a few parts in 10^8 [13].

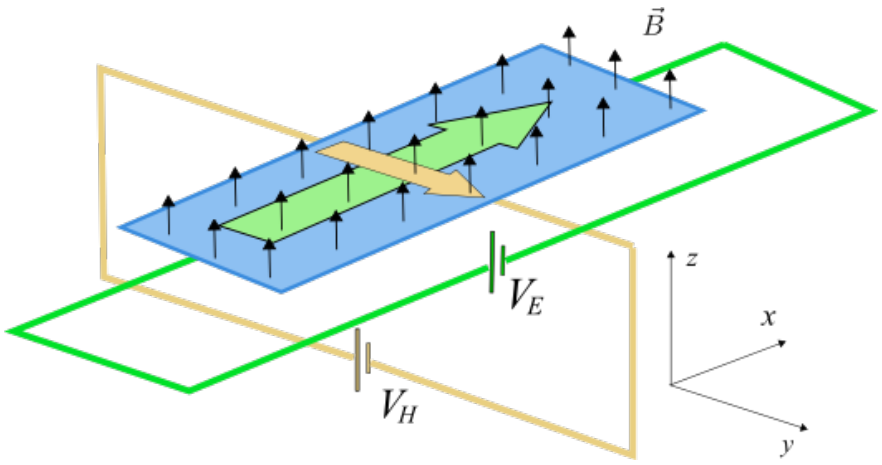

Figure 1.3: A schematic diagram showing how classical measurements are taken. An induced current (green arrow) flowing along the sample and the magnetic field is applied perpendicular (black arrows) to the direction of current flow, where V_E is the longitudinal voltage and V_H is the Hall voltage [77].

1.2.1 The Quantum Hall Effect (QHE)

The QHE was discovered by Klaus von Klitzing in 1980 [40]. In 1990, the QHE was recommended as a primary standard for calibrations of standard resistors. More information about the QHE will be discussed in chapter two. Under this section, we will discuss the classical Hall Effect.

The classical Hall Effect was observed by Edwin Herbert Hall in 1879. Hall was attempting to prove that a magnet directly affects current and not the wire (electrical conductor) bearing the current, as was believed during the 19^{th} century [58]. When a strong magnetic field (black arrows) is placed perpendicular (see figure 1.3) to the direction of the current flow (green arrow), the electrons are pushed to one side of an electrical conductor by what is called the Lorenz force, this force is itself perpendicular to the applied B_z field and direction of current flow.

$$\vec{F}_y = -e\overrightarrow{v_x} \times \overrightarrow{B_z}, \tag{1.1}$$

where v_x is velocity and B_z field applied. The Lorenz force is known as the velocity dependent force that pushes electrons at a right angle to the velocity and right angles to the magnetic field. A voltage drop appears perpendicular due to the build-up of excess charge and is called

the Hall voltage V_H. The appearance of the Hall voltage is known as the Hall Effect [85]. If a surface gate is present on top of the sample, where the sample is denoting a conductor being semiconductor. The Hall voltage decreases with increasing top gate voltage, simply because there is an inverse proportionality between the Hall voltage and the electron concentration with the voltage proportional to the product of the device input current I and the applied magnetic field B [26]. The Hall Effect was a surprising discovery, it occurs under steady-state conditions, meaning that the voltage across the electrical conductor persists even when the current and magnetic fields are time independent. The experimental study of the Hall Effect is an effective method to investigate the motion of charge carriers in metals and semiconductors and determine the concentration of the charge carriers as well as mobility [43]. The Hall field is given by:

$$E_H = R_H J_x B_z, \tag{1.2}$$

where R_H is the Hall coefficient and J_x the current density. Compensation between the Hall field E_H and the Lorentz force (in opposite direction) must occur for electrons to pass through the wire (or the electrical conductor), thus

$$-eE_H = -ev_x B_z. \tag{1.3}$$

Electrons will no longer experience a deflection due to the magnetic field force after the compensation. In the study of Epstein [19], it was stated that after the compensation between the Hall field and the Lorentz force the electron will continue flowing in its original direction as if unaffected by the magnetic field, this equilibrium is accomplished only for the case of current carriers with a single velocity. The Hall voltage can be expressed as

$$V_H = v_x B_z w. \tag{1.4}$$

Here w is the width of the sample (electrical conductor) and the electrical current is given by

$$I_x = n(-e)v_x A, \tag{1.5}$$

where A is the cross-sectional area of the electrical conductor, given by $A = td$, n is the electron density. From equation 1.3 E_H can be given by

$$E_H = B_z v_x. \tag{1.6}$$

It was mentioned above that the Hall voltage is proportional to the current and the magnetic field, this implies that the Hall voltage is linked to the Hall coefficient such that it is given by

$$V_H = -\frac{BI}{net}. \tag{1.7}$$

Equation 1.7 can be expressed in terms of current density and Hall field such that it becomes

$$\frac{E_H}{JB} = R_H = -\frac{1}{ne}. \tag{1.8}$$

Equation 1.8 is negative because the Hall field is in the negative y-direction and indicates that the Hall coefficient is inversely proportional to the carrier density in a Hall device.

1.2.2 The Josephson Effect (JE)

The Josephson effect (JE) is one of the three phenomena that completes the quantum metrological triangle, it takes place at low temperatures in a junction of two weakly coupled superconductors where they are separated by a thin insulating layer. The electrons are paired in each superconductor as (Cooper pairs) and their wavefunction is given by:

$$\Psi = Ae^{i\phi}, \tag{1.9}$$

where A is the amplitude and $e^{i\phi}$ the phase factor. The Josephson effect shows two main characteristics

- The supercurrent is given by $I_J = I_C \sin\phi$, this happens when the Cooper pairs tunnel through the junction at zero voltage drop. Where I_C is a constant and $\phi = \phi_1 - \phi_2$ is the phase difference of the two wavefunctions of the electrons.

- When we have a constant voltage U through the junction, oscillation of the tunnelling supercurrent is induced at a frequency $f = \frac{2e}{h} \times U$.

The first characteristic was observed by Sidney Shapiro [70], and the second Brian Josephson [35]. $I_J = I_C \sin\phi$ is known as the DC Josephson effect equation, it entails that current can flow with a DC voltage across the junction if $I_J < I_C$, and if $I_J > I_C$ a voltage appears across the junction, giving arise to an alternating current of frequency f this is known as the ac Josephson effect [32].

$2e/h$ corresponds to the inverse of the flux quantum ϕ_o. Due to energy change $2eU$ involved during Cooper pair tunnelling, the variation of the phase difference is given by:

$$\frac{d\phi}{dt} = \frac{2e}{\hbar}U. \tag{1.10}$$

From equation 1.10 we get

$$U = \frac{\hbar}{2e}\frac{d\phi}{dt} = \frac{h}{2e}f. \tag{1.11}$$

This results in steps of constant voltage U_n due to the phase locking of the Josephson oscillator to the external frequency

$$U_n = n\frac{h}{2e}f, \tag{1.12}$$

where n is the step number. Rearranging equation 1.12 we obtain the Josephson constant, given by

$$\frac{f}{U} = 483\,597.90\,\text{GHz/V} = K_J \tag{1.13}$$

The International Committee for Weights and Measures (CIPM) has recommended implementing the JE as a voltage standard, using the Josephson constant K_J as an estimate $2e/h$ and for calibration of purpose using the assigned single value $K_{J-90} = 483597.90$ GHz/V with the uncertainty of 4 parts in 10^7. The voltage realised from the JE is independent of the materials of the superconductors, Josephson junction type and its geometry, the temperature and the frequency [28]. Manufacturing companies these days are producing multilayer Josephson junctions that are connected in series for DC applications or programmable voltage standards.

1.2.3 Current standard

Currently, electrical current can be defined indirectly by making use of the JE and the QHE together with Ohm's law. Researchers around the world are working on realising the current standard directly by creating a system which can control the transport of electrons one by one with a known frequency. SET devices provides a means of manipulating individual electrons and detecting them with extraordinary precision [37]. Their potential contribution

to metrology was recognised in the 1980s and in 1990s where SET devices were demonstrated as single electron pumps and turnstiles [37].

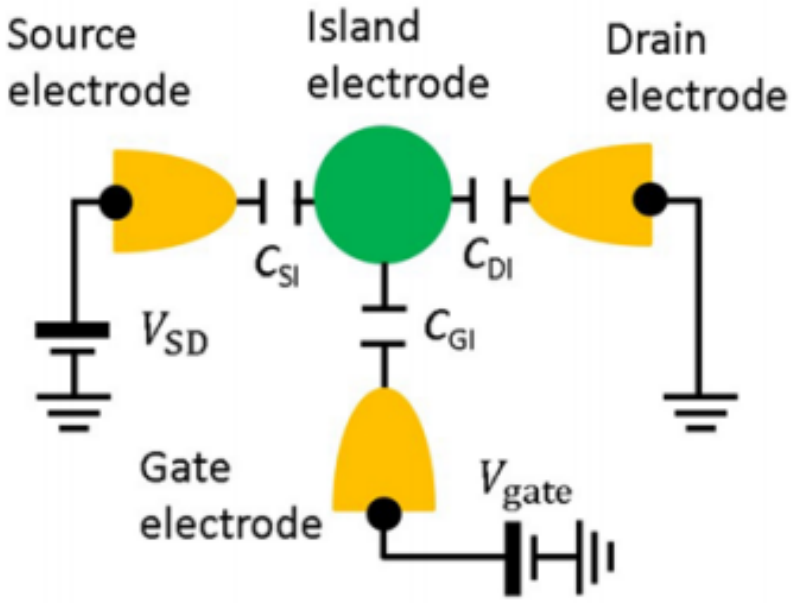

Figure 1.4: Schematic illustration of the SET device [36].

SET transistors [42] and electron pumps [86] have been identified as suitable devices for the realisation of the current standard. They both operate under the principle of Coulomb blockade. Two tunnelling junctions separated by a thin insulator where electrons can tunnel from one electrode to the other, this induces electrostatic energy given by

$$E_C = \frac{e^2}{2C}, \tag{1.14}$$

where C is the total capacitance of the device, which is given by $C = C_{SI} + C_{DI} + C_{GI}$, the capacitances between the source and the island, the drain and the island, and the gate and the island respectively as illustrated in figure 1.4. Electron transport occurs if external energy, larger than E_C is applied to the system. If the applied energy is less, then no conduction through the dot can take place and this is known as Coulomb Blockade. In metallic SET, the devices are created in a way that they have two tunnelling junctions of capacitance C where they isolate the metallic island. For the SET effects to be observed the following needs to happen:

- The metallic island needs to be sensitive to the change of number of electrons, even when millions of electrons are already present on the island.
- The electrostatic charging energy which is the energy needed to add a single electron to the dot must be greater than the thermal energy $k_B T$.
- The tunnel barriers must be sufficiently opaque that the wavefunctions of an extra electron on the island is well localised.

A Scanning Electron Microscope (SEM) image of a SET device is shown in figure 1.5 below [51]. The device contains source (S), drain (D) and three voltage gates labelled A, B and C. Electrons flow through the device from the source to drain shown in red. Two green gates A and B form an island as mentioned above and the blue gate C is used to control the size of the island. Electrons can tunnel into the island by lowering the voltage of gate A. Inside the island electrons occupy different energy levels as the voltage is being raised on gate C.

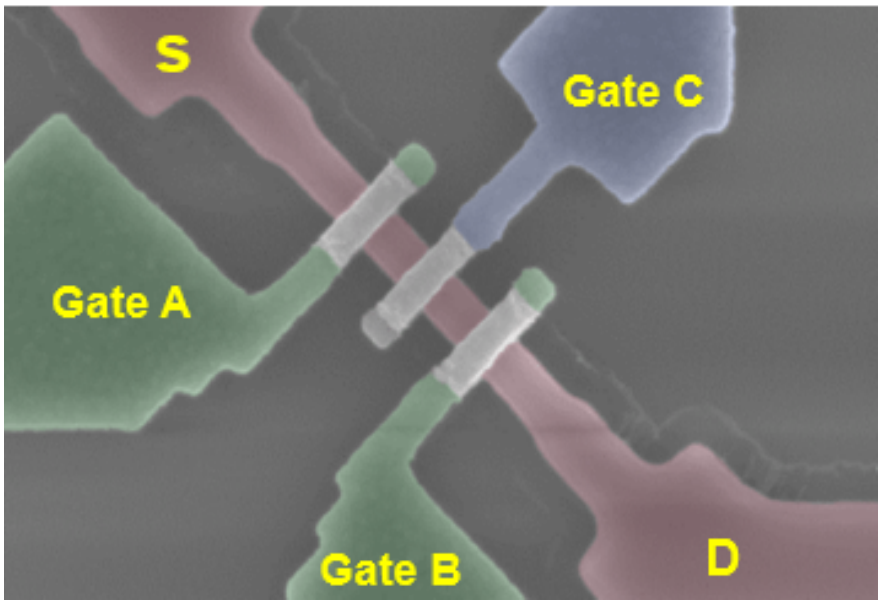

Figure 1.5: A simple single electron transport (SET) arrangement. Electrons travel along the red path. Adopted and modified from [51]

The continuous raising of the voltages on gate A and B allows electrons to enter and exit confined region via tunnelling from the source to the drain. Repeating the process at higher frequency f, electrons will travel one at a time across the device providing a source of current, given by $I = nef$, where n is the number of electrons moved, e the charge and f the frequency. The voltage on gate C determines the size of the dot, which determines the number of electrons (n) captured each cycle.

2 | Chapter 2: Literature Review

In this chapter, we will discuss the Quantum Hall Effect (QHE) with its experimental observations and theoretical interpretations as well as its importance in electrical metrology. The sections discussed are 2.1 Background, 2.2 Semiconductor Heterostructure, 2.2.1 Band Gap Engineering, 2.2.2 Modulation Doping, 2.2.3 Molecular Beam Epitaxy (MBE), 2.3 Quantum Hall Effect, 2.3.1 Quantum mechanics of Electrons in a Magnetic Field, and 2.4 Shubnikov-de Haas Oscillations.

Studies of the QHE provide a wonderful opportunity to study and utilise the physical properties of the macroscopic and two-dimensional electron gas. The results revealed interesting effects in condensed matter physics and electrical metrology. A paper by Landwehr Gottfried [46], has stated that the discovery of the QHE demonstrated that cooperation between theory and experiment is essential, this was highlighted after the discovery of Klaus von Klitzing was brought into question as initially, no theory was available to describe the results.

2.1 Background

The QHE is a most remarkable condensed-matter phenomenon discovered in 1980 [22], at the high magnetic field facility in Grenoble. It rivals superconductivity in its fundamental significance as it provides evidence of quantum mechanics on macroscopic scales [22]. Theoretical work by Ando and Uemura [1], revealed the role of fundamental constants in the magneto-transport properties of a two-dimensional electron gas (2DEG). The QHE takes place in a very thin layer of electrons essentially at a two-dimensional sheet of electrons or electron gas. A 2DEG is formed at a semiconductor-insulator interface in a gallium arsenide (GaAs) heterostructure [67]. The first observation of the QHE was in a Metal-Oxide-Semiconductor Field-Effect Transistor (MOSFET) [78], the electrons are trapped in the inversion layer of silicon and silicon dioxide, where silicon acts as a semiconductor and silicon dioxide as an insulator.

2.2 Semiconductor Heterostructure

The devices of the QHE are Hall bars embodied in Si-MOSFETs or GaAs-AlGaAs heterostructures. Semiconductors are intermediate in their properties between good

conductors and a good insulator, where their resistivity lies between 10^{-4} and 10^{7} Ωm. Semiconductor heterostructures are formed by a junction between two dissimilar solids in a wide range of III-V groups material, forming a 2DEG at a heterojunction, where the composition is varied to control the motion of electrons and holes through band engineering. This helps in obtaining desirable electrical properties of the heterostructures, such as electron density (n) and electron mobility (μ). Heterostructures are fabricated using Molecular Beam Epitaxy (MBE) under ultrahigh vacuum which is presented in subsection 2.2.2. These semiconductors are known as low-dimensional structures; they are referred as "low-dimensional structures" as the free electrons are confined into lower dimensions due to the structural profile of the material [3].

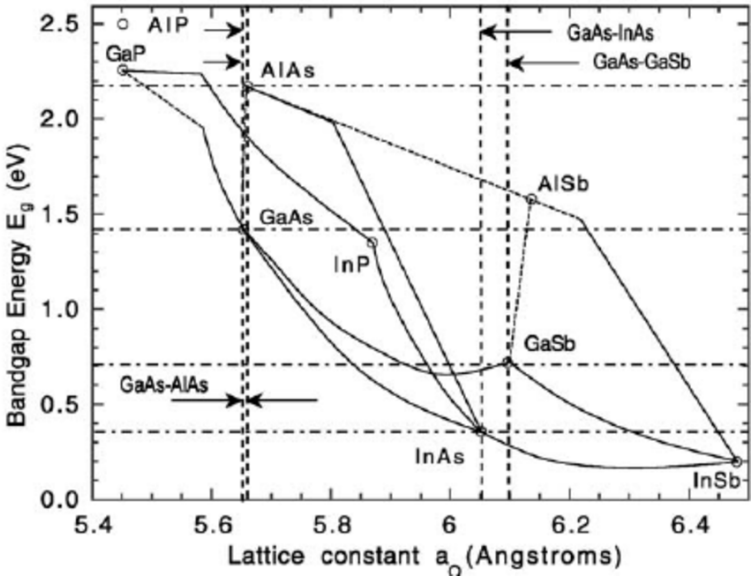

Figure 2.1: Band-gap energy Eg versus lattice constant a_0 for the most common III-V semiconductors [55]. With GaAs setting at a lattice constant of 5.65321 Å , and AlAs at 5.66220 Å.

The properties of these Hall devices are increased widely by using alloys between various compounds, notably the alloy $Al_xGa_{1-x}As$ which is abbreviated as AlGaAs, where x is the fraction of Al in the alloy. Merging the two solids is possible if they have the same crystal structure or at least symmetry and their lattice constants must be very close to one another [12]. In figure 2.1, we see that the GaAs and AlAs lattice constants are almost similar. This means that for fabrication of GaAs-AlGaAs heterostructure will be possible, due to minor

variation of the lattice constants.

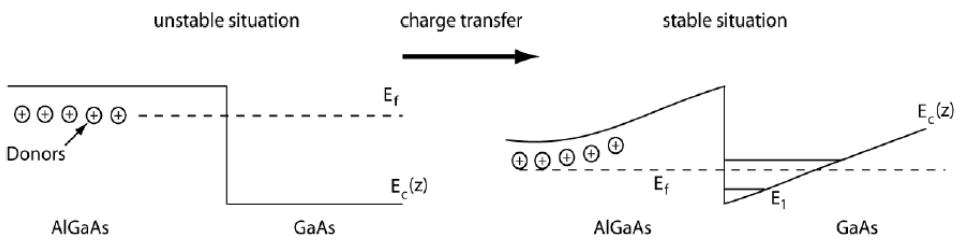

Figure 2.2: Migration of electrons from the aluminium gallium arsenide (AlGaAs) to the GaAs resulting depletion layer in AlGaAs and causing the band of gallium arsenide (GaAs). The schematic diagram is adopted from [73].

2.2.1 Band-Gap Engineering

The ability to tailor band-structure to obtain novel electrical and optical properties is known as band-gap engineering. When considering the fabrication of heterostructures, the lattice constants of the materials are important. Anderson's rule states that the vacuum levels of the two materials of a heterojunction should align [12]. In an undoped semiconductor every electron that migrates from the valence band to the conduction band leaves positive charges behind, this results in a depletion layer in the valence band of AlGaAs, which gives rise to a strong electric field which results in a bend in the conduction band of the GaAs as illustrated in figure 2.2 [73]. In the study of Wang *et al.* [79] it is cited that an ideal model of 2DEGs was first proposed by Peierls in 1933 qualitatively evaluating the de Haas-van Alphen effect in 3D metal. In this study, we focus on 2DEGs that are formed from the heterostructure in a (AlGaAs) material system.

2.2.2 Modulation Doping

Modulation doping is a technique used to achieve high electron mobility in semiconductor heterostructures, this is achieved by separation of donors and the electrons. High electron mobility is important in the QHE since electrons need to follow the sub-band's trajectory. When a 2DEG is in close proximity to positive charges, the mobility of the electrons, is reduced making it difficult to observe the QHE and other related phenomena. A spacer layer is introduced to keep the electrons away from the positive ions as illustrated in figure 2.3b. The spatial separation leads to a strong suppression of scattering caused by positive ions and subsequently increases the electron mobility, especially at the low temperatures.

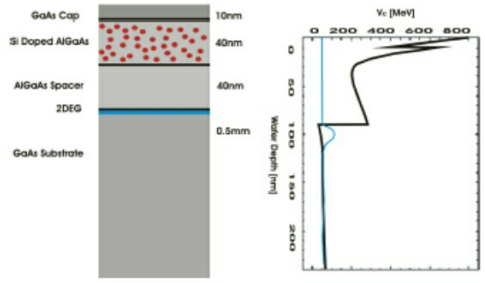

(a) Schematic diagram of heterostructure showing composition of the different layers [5].

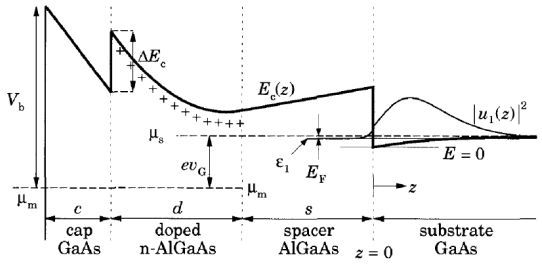

(b) Schematic diagram band-gap diagram showing a spacer layer. [12].

Figure 2.3: The structure picture showing modulation doping between the two-material system of AlGaAs and GaAs. The conduction band E_C of GaAs is dragged below the Fermi level to form a 2DEG indicated with as a triangular well where electrons exists. The relevance of figure 2.3a is to illustrate the composition of the wafer and showing how far is the 2DEG from the surface of the GaAs Cap

2.2.3 Molecular Beam Epitaxy (MBE)

MBE is an advanced system for growing semiconductor heterostructure materials, with ultrahigh accuracy and very low impurities. A schematic diagram and photograph of a typical MBE system are given in figure 2.4. The key component of the MBE system is the chamber with an ultrahigh vacuum. Attached to the chamber are four Knudsen cells also known as effusion cells containing pure starting materials Ga, Al, and As in the solid state as shown in figure 2.4a. The source materials in the cell are heated to a temperature of 1000 °C. When the shutters are opened the gaseous materials are released. They condense on the substrate, where they react with each other. For proper fabrication, the substrate is rotated to avoid variations in composition across the wafer. The reaction between the starting materials is controlled by the temperature of the substrate and the flow rate of the source materials which can be adjusted by the temperature of the Knudsen cell. A temperature of 600 °C is required at the substrate to ensure the growth of a GaAs crystal with a complete ratio of 1:1. MBE is considered as a slow process because of its growth rate of 1 µm per hour or growing material at 1 monolayer per second.

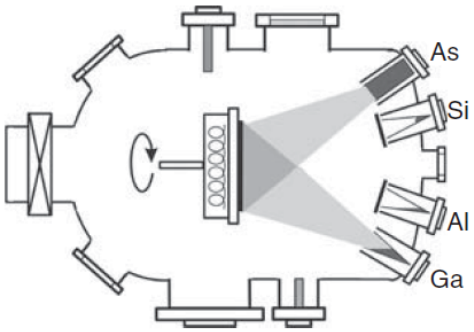

(a) Schematic diagram of MBE [23].

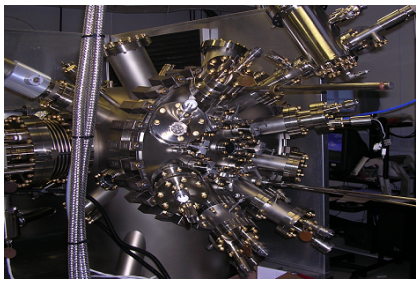

(b) Exterior of an MBE Chamber [7].

Figure 2.4: Schematic representation of an MBE chamber (2.4a) for the epitaxial growth of GaAs-$Al_xGa_{1-x}As$ heterostructures and a photograph showing the exterior of an MBE Chanber (2.4b).

Essential to MBE is the ultrahigh vacuum (UHV) in the system chamber, which is typically 5×10^{-11} mbar or better [12]. UHV conditions are used in MBE simply because the process involves the evaporation of elemental sources at a controlled rate onto a substrate surface held at a suitable temperature [61]. There are two main advantages in using UHV. Firstly, the source materials can reach the growth surface or substrate in a very clean condition [61]. Secondly, the growth process can be monitored in-situ a monolayer at a time, using Reflection High-Energy Electron Diffraction (RHEED) [23; 61; 12]. Auger Electron Spectroscopy (AES), X-ray Photoelectron Spectroscopy (XPS), Low-Energy Electron Diffraction (LEED), Secondary-Ion Mass Spectroscopy (SIMS) and Ellipsometry are further techniques that can be used to monitor the growth in-situ [61].

2.3 Quantum Hall Effect (QHE)

Firstly, we will recap the classical Hall effect (CHE), with the experimental setup shown by figure 1.3. The CHE describes the development of the Hall field E_H perpendicular to the direction of current flow. Then due to the constant magnetic field that deflects the electrons, a velocity driving force known as the Lorentz force is established. It was mentioned that electrical force and the Lorentz force compensate each, by equation 1.3. In this regard the electrons can no longer be deflected as a steady-state is reached, from this we are able to measure the Hall voltage V_H and the longitudinal voltage V_{xx}. From this, we can determine the Hall coefficient R_H which is linked to the Hall voltage, the current and the magnetic field given by equation 1.8.

2.3.1 Quantum mechanics of Electrons in a Magnetic Field

In a magnetic field, an electron will precess around the field flux. The inverse of the frequency ($^1/_f$) is referred to as the time electrons take to complete one orbit cycle, but we are interested in describing what happens to electrons in a magnetic field from the quantum mechanical point of view. The Schrödinger equation is used to describe this, considering the applied magnetic field perpendicular to the direction of electron flow in a 2DEG. This leads to an effect in one of the remaining non-confined directions (x and y) in a 2DEG. The Schrödinger equation for the magnetic field takes on the form:

$$\frac{1}{2m}[p_x^2 + (p_y - eB)^2]\psi = E\psi. \tag{2.1}$$

The components of the momentum vector $p = (p_x,p_y)$ are given by:

$$p_x = -i\hbar\frac{\partial}{\partial x} \quad \text{and} \quad p_y = -i\hbar\frac{\partial}{\partial y}. \tag{2.2}$$

The vector potential is given by $\mathbf{A} = B(0, x, 0)$. Equation 2.1 can be transformed into a time-independent Schrödinger equation of a Harmonic oscillator

$$\left[\frac{1}{2m}\frac{\partial^2}{\partial x^2} + \frac{1}{2}m{\omega_c}^2(x + kl_B)^2\right]\psi = E\psi, \tag{2.3}$$

where ω_c is the cyclotron frequency given by eB/m^*, e is the electron charge, B is the magnetic field with m^* the effective mass. This is the frequency with which the electron completes one orbit, k is the wavevector in the y-direction, and $l_B = \sqrt{\hbar/eB}$ is the magnetic length, where $\hbar$ is the reduced Planck's constant. If we consider the orbital motion of electrons only, then equation 2.3 results in eigenfunctions of allowed eigenvalues of energy levels for the electrons which is given by:

$$E_n = (n + \frac{1}{2})\hbar\omega_c, \quad (n = 0, 1, 2, 3,). \tag{2.4}$$

Here n is a new quantum number called the Landau level index. These energy levels are quantised and are known as Landau levels, named after Lev Landau who in 1930 was the first to apply quantum mechanics to the study of metallic systems and the quantum treatment of electronic motion in a static uniform magnetic field [47]. The Landau quantisation (Landau Levels) is caused by a strong magnetic field perpendicular to the 2DEG, which results in

the quantised energy spectrum [78]. From equation 2.4 it is observed that an increase or decrease in magnetic field leads to a shift in the energy levels. This is given by $\hbar\omega_c$ the spacing between Landau levels.

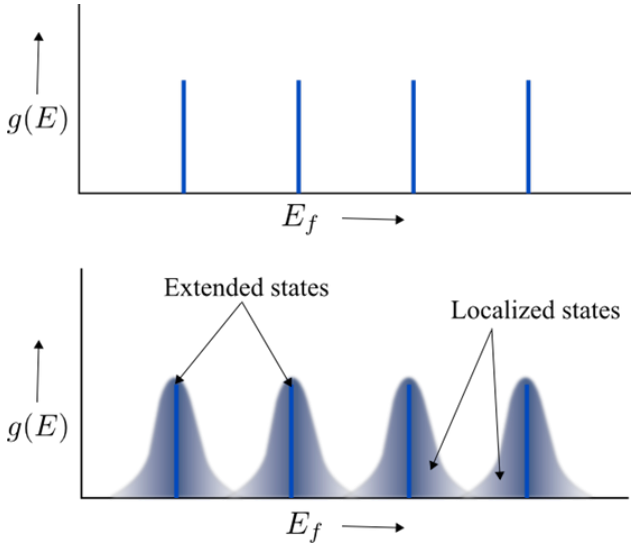

Figure 2.5: Landau levels of a 2DEG in a clean system (top) and in a disordered system (bottom) [77]. Observing the top diagram with the absence of disorder, Landau Levels appear as equidistant delta functions which are defined by cyclotron energy given as $\hbar\omega_c$. In the presence of disorder localised and extended states are observed (bottom). In both clean and disordered system $g(E)$ corresponds to number of states with energy and E_f is the Fermi emery.

The material system (Hall devices) are not perfect even though they were fabricated utilising MBE. We have a disordered system that leads to more complexity in the Landau levels. This leads to the formation of extended and localised states shown in figure 2.5 bottom. These localised states help explain the observations made in the QHE.

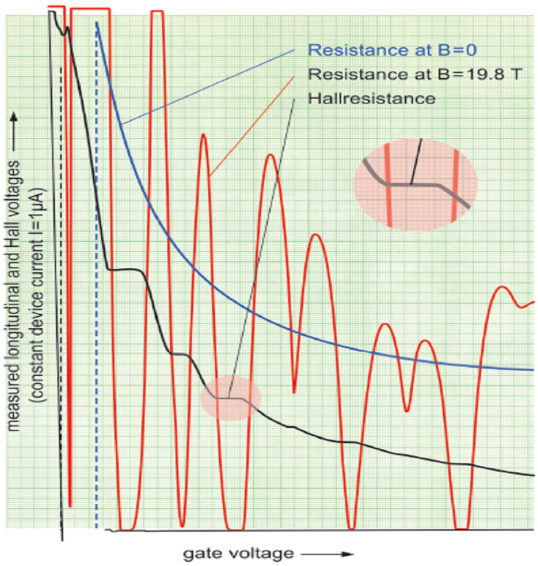

(a) QHE measurements in a MOSFET by von Klitzing [78].

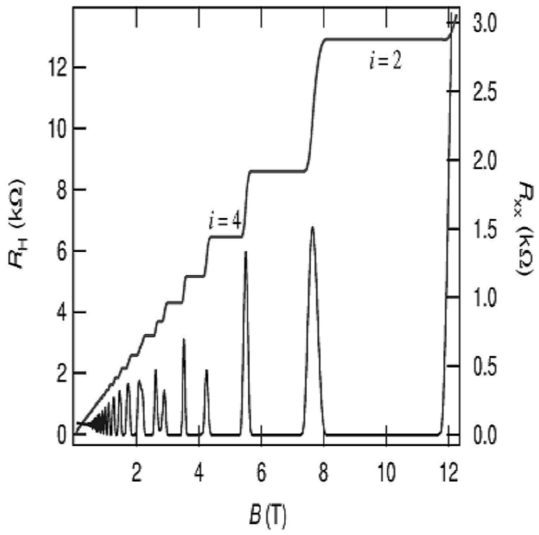

(b) QHE measurement in a GaAs/AlGaAs heterostructure Jeckelmann *et al.* [33].

Figure 2.6: Both figures show Hall resistance and longitudinal resistance in different samples at liquid helium temperature, figure 2.6a as a function of gate-voltage and figure 2.6b as function of the applied magnetic field $\boldsymbol{B}$.

2.3.2 Transition to the QHE

When a 2DEG is exposed to a strong perpendicular magnetic field the following is observed. Both figure 2.6a and figure 2.6b shows the SdH oscillations and the quantum Hall plateaus from different samples. Where the resistance is constant and given by h over e^2. When the device is cooled down below 4 K the QHE is observed. At low temperatures disturbances due to scattering originating from electron-phonon interactions are suppressed [78]. This fascinating observation is explained with Landau levels as mentioned in subsection 2.3.1. Since we have the extended and localised states they both play a different role in the QHE.

The localised states are responsible for the vanishing of the longitudinal conductivity σ_{xx} and longitudinal resistance R_{xx}, while the extended states are responsible for the transverse resistivity ρ_{xy} and conductivity σ_{xy} as they carry current during the experiment. At low temperatures, the Hall resistance develops a series of plateaus at a resistance that is defined by fundamental constants of nature, Planck's constant (h) and the electron charge (e). The flatness of the plateau is increased in width when the temperature is lowered or the magnetic field is increased [17]. It is also observed that the values of R_{xx} and R_{xy} are

constant at magnetic fields when the Fermi level is between Landau levels in the localised states, corresponding to exactly an integer value of the filling factor [23], where the filling factor is determined by the number of completely filled Landau levels.

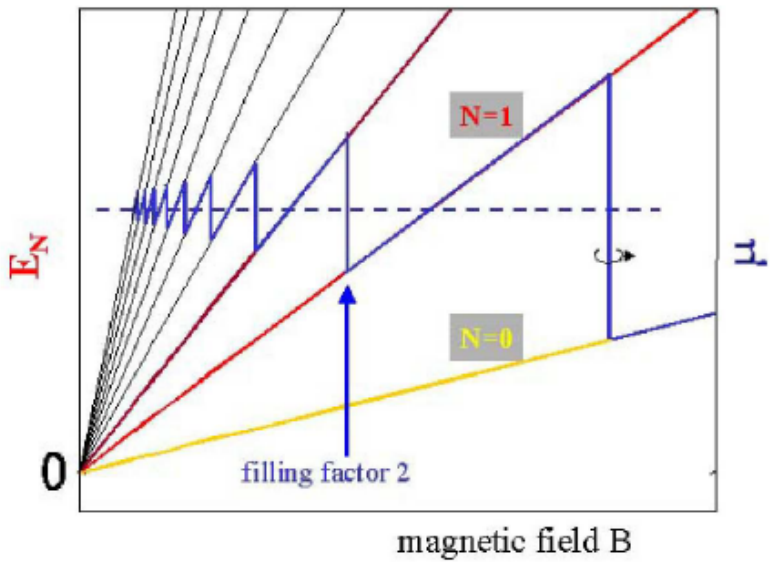

Figure 2.7: Variation of the Fermi level in a 2DEG as a function of magnetic field. The Fermi level (blue line) jumps between Landau levels at integer filling factors with the electron density remaining constant all the time [78].

The QHE experiments are performed with n_{2D} held constant, implying that the number of occupied Landau levels are bound to change. This is illustrated in figure 2.7, where it's evident that the Fermi level E_F (which is given by the red line), moves with the density of states to keep the number of electrons constant [12]. von Klitzing has stated that the Fermi level E_F locates at special values of the magnetic field in energy gaps between Landau levels so that observation of the QHE can be fulfilled [78].

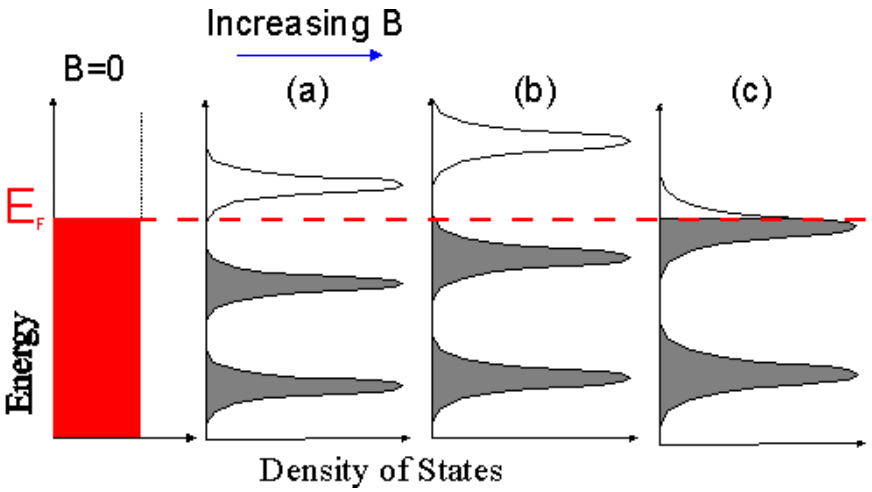

Figure 2.8: Energy level versus the number of free-states that electrons can occupy for increasing magnetic field strength [44].

Consider figure 2.8, starting with $B = 0$, the density of states is constant up to the Fermi energy, since the energy spectrum is continuous. Increasing the magnetic field the energy spectrum becomes quantised and the allowed number of states in each Landau level becomes

$$n_B = v\frac{eB}{h}. \tag{2.5}$$

Here v is the filling factor, an integer number of Landau levels filled with electrons. Substituting equation 2.5 into equation 1.8 results in

$$R_{xy} = \frac{B}{en} = \frac{h}{ve^2}. \tag{2.6}$$

When the Landau levels are fully occupied, the Hall resistance is an integer fraction of the quantity $\frac{h}{e^2}$. When experiments are performed in a 2DEG, wide plateaus at high magnetic fields are observed, where the centres of the plateaus mark complete filling of the corresponding integer number of Landau levels and this entails a minimum in the Shubnikov-de Haas oscillations shown in both figure 2.6a and figure 2.6b. The ratio in equation 2.6 was discovered by von Klitzing in 1980 having a value of 25 812.807 Ω. Since the ratio has the SI units of resistance, it was in 1990 when the CIPM announced the representation of resistance as given by equation 2.6. The QHE is used to maintain the standard electrical resistance in metrology institutes around the world [22] known as Quantum Hall resistance

(QHR). The SI Unit Ohm (Ω) is referred as a modern unit, since it is not affected by external parameters like ambient conditions, does not drift with time [33] and is independent of the sample properties of the 2DEG [16]. This is, unlike standard wire resistors, that can have any value, depending on the material and geometry of the wire [17]. The QHR is stable which contributes to its suitability as the standard for electrical resistance.

2.4 Shubnikov-de Haas Effect

The Shubnikov-de Haas Effect (SdH) is the oscillatory behaviour of the magneto-resistance appearing in degenerate semiconductors and semi-metals at low temperatures and in high magnetic fields [65]. In 1930 Shubnikov and de Haas observed the first oscillations in the electrical resistivity as a function of magnetic fields [66]. The discovery of the SdH oscillations led to the development of an entire branch of physics of oscillations of both kinetic and thermodynamic characteristics of metals, alloys, and degenerate semiconductors having different symmetry, composition and size, and shape of the Fermi surface. The resistivity is constant at low magnetic fields but develops strong oscillations with zeros at high fields [12]. According to Chou *et al.* [10], in strong magnetic fields the longitudinal resistivity ρ_{xx} no longer oscillates, but exhibits wide zeros and with sharp peaks in between. In-order to observe the SdH effect oscillations, the following condition needs to be met.

$$\hbar\omega_c \gg k_B T \implies T \ll \frac{\hbar\omega_c}{k_B}, \tag{2.7}$$

$$\omega_c \tau \gg 1. \tag{2.8}$$

The observations of the SdH oscillations requires that the thermal energy broadening, $k_B T$ and the scattering-induced energy broadening, $\omega_c \tau$ should be smaller than the Landau level spacing, $\hbar\omega_c$ where k_B is the Boltzmann constant, T is the temperature, and τ is the momentum relaxation time. To satisfy this condition one needs a low temperature and high magnetic fields appropriate to the Fermi level E_F which is affirmed by equation 2.7. The SdH oscillations have an inverse field $^1/_B$ dependence and the peaks in the SdH oscillations occur at the same magnetic field as the changes in the quantum-Hall resistivity. The SdH oscillations can be used to characterise the material system since the resistivity minimum corresponds to the filled Landau level with electron density in the 2DEG given by

$$n_{2D} = v\frac{eB_v}{h}, \tag{2.9}$$

where v the number of filled Landau level, B_v corresponds to the magnetic field minimum of the SdH oscillation in the low magnetic field regime. When analysing adjacent minima in figure 2.6a and figure 2.6b the equation 2.9 becomes

$$\Delta\left(\frac{1}{B}\right) = \left(\frac{1}{B_{v+1}} - \frac{1}{B_v}\right) = \frac{e}{hn_{2D}} = \frac{1}{\phi_o n_{2D}}, \tag{2.10}$$

where $\phi_o \equiv {}^{e}/_{h}$ is the magnetic flux quantum. The resistivity ρ is often considered rather than the resistance R since the resistivity characterise the physical properties of the material. The longitudinal resistivity is given by

$$\rho_{xx} = \frac{1}{n_{2D}e\mu}, \tag{2.11}$$

where the electron mobility is defined by $\mu = e\tau/m^*$, τ is the relation time and m^* is the effective mass. From Göbel *et al.* in 2D space the longitudinal resistance [23] is given by

$$R_{xx} = \rho_{xx}\frac{L_x}{L_y}. \tag{2.12}$$

The analysis for the electron mobility in the low magnetic field regime, after rearranging equation 2.12 and substituting the resulting equation into equation 2.11 we get

$$\mu = \frac{1}{n_{2D}e}\frac{L_y/L_x}{R_{xx}(B=0)} = \frac{1}{n_{2D}e\rho_{xx}(B=0)}, \tag{2.13}$$

here L_y and L_x are the dimensions of the material system used.

3 | Chapter 3: Sample Fabrication

In this chapter, we will discuss the samples and the techniques behind the sample fabrication. The sections are as follows: 3.1 Growth and Design of Wafer Structure, 3.1.1 Mesa Fabrication, 3.1.2 Ohmic Contacts, and 3.2 Mounting and Testing.

3.1 Growth and Design of Wafer Surface

In terms of fabrication of the devices, we give thanks to our Nanoelectronics UCT research members Dr. Hume Howe and Associate Professor Mark Blumenthal for their great collaboration with the Cavendish laboratory at the University of Cambridge for allowing them to use the state of art facilities to fabricate devices. A series of processes are required for the fabrication of the devices; namely wafer growth, lithography and etching processes. Notable the features that need to be taken into consideration during sample design are a current path for electrons to flow through the device and Ohmic contacts to connect to the 2DEG.

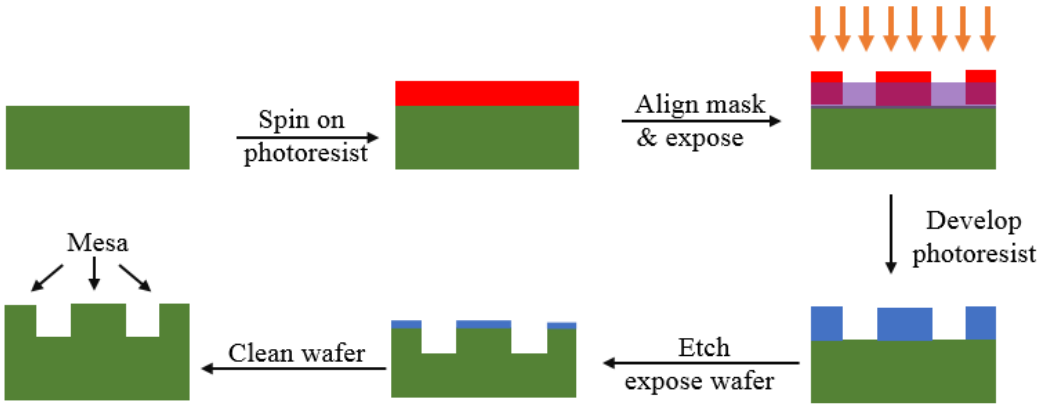

Figure 3.1: Mesa fabrication process.

3.1.1 Mesa Fabrication

The mesa is a region of the wafer with 2DEG that remains after the unwanted 2DEG material has been removed by etching the dopant layer. It is a way of isolating a 2DEG region. Photolithography was used to create a mesa; the process is detailed in figure 3.1. The wafer was coated with a photoresist. A chrome mask which defines the mesa pattern was aligned over the wafer as it was exposed to UV radiation. The dissolving agent known

as a developer was utilised to dissolve away the soluble photoresist. Regions of the wafer that are not covered by the photoresist were etched away by hydrogen peroxide, hydrogen chloride and water solution, then finally cleaned by acetone to leave the surface pattern of the mesa visible.

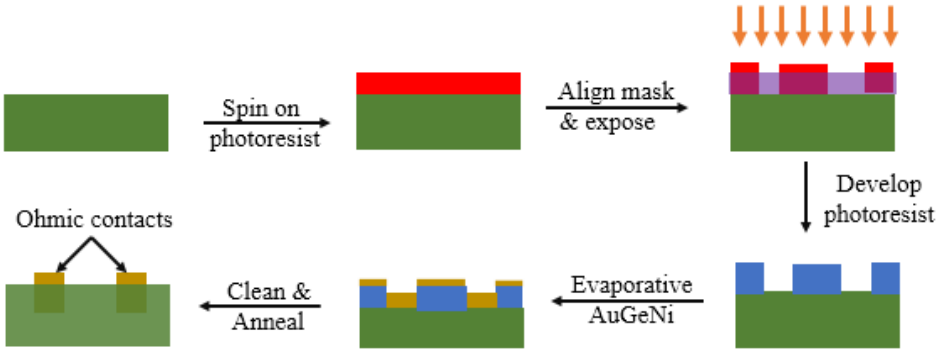

Figure 3.2: The Ohmic contacts method.

3.1.2 Ohmic Contacts

Ohmic contacts play a major role in the signal transfer to and from the semiconductor and the external circuitry [62]. The important fact to consider when fabricating Ohmic contacts is their resistance, it should be low or negligible. To access a 2DEG which is 90 nm (see figure 2.3a) below the surface of the wafer, the Ohmic contacts should demonstrate Ohmic behaviour. The electrical current should showcase a linear behaviour, which is directly proportional to the applied voltage. Photolithography was used to fabricate Ohmic contacts, the method is outlined in figure 3.2. Ohmic contacts were processed after the successful fabrication of the mesa. Fabrication of Ohmic contacts was processed in the same fashion as the mesa as outlined in figure 3.1. The difference here was that the materials were deposited instead of being etched away. Evaporation of the desired material onto the wafer was made, where it binds to the topmost surface of the wafer, then the residual resist or the materials were cleaned away with acetone. Gold-germanium-nickel (AuGeNi) was the entrusted material for Ohmic contacts. An additional step known as annealing was applied, this causes the gold, germanium and nickel alloy to diffuse into the wafer to form contact to the 2DEG, in our case 90 nm below the surface of the wafer.

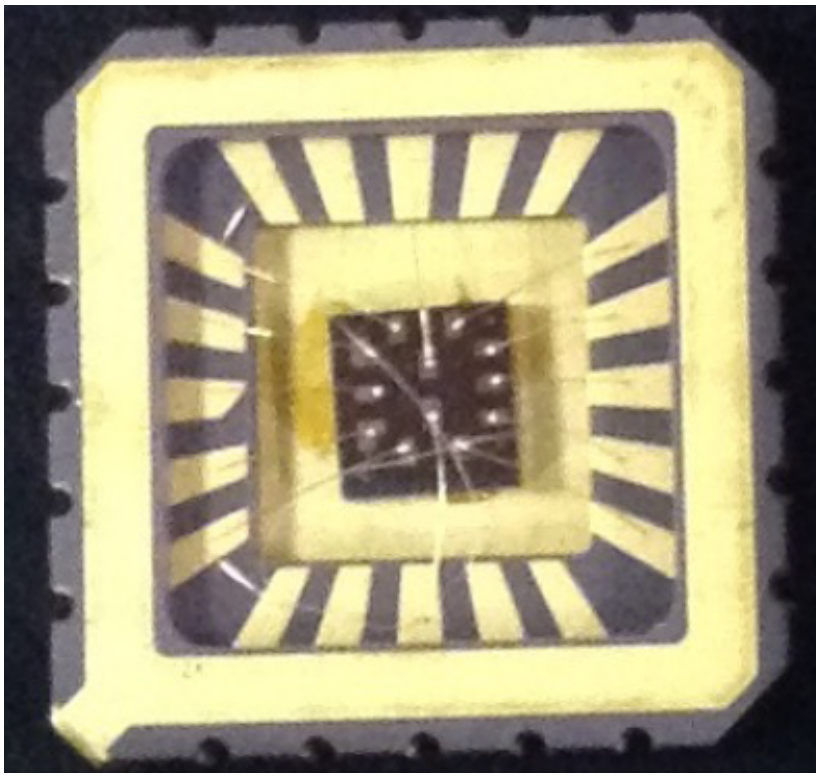

Figure 3.3: Photograph of a heterostructure device (black wafer in the centre) placed in a leadless chip carrier (LCC). With visible gold wires that connect the contacts on the device to the LCC terminals [83].

3.2 Mounting and Testing

The wafer was first cleaved and then packaged inside a Leadless Chip Carrier (LCC), it was rounded by 20 pins through the edges of the ceramic, a photograph is shown in figure 3.3. 25 µm gold wire was utilised to bond the terminals of the LCC together to the Ohmic contacts. In our case, the samples arrived here in South Africa at UCT as wafers, they were cleaved and packaged using a MPP-4522 ball bonder. Trial testing in liquid nitrogen was carried out at several stages of the process, including after being packaged to ensure that the whole device and the Ohmic contacts are well connected. If the Ohmic contacts are in good condition each pair will obey Ohm's law at room temperature. Post growth testing is carried out at Cavendish laboratory to determine the wafer's electrical properties, such specification for the device we measured were not available [83].

4 | Chapter 4: The ^{3}He/^{4}He Dilution Refrigerator and Experimental Setup

In the ever-changing field of research, ultra-low temperatures are required, one such instrument for these low temperatures is a dilution refrigerator [76]. The dilution refrigerator was suggested by Heinz London in 1952 and it was at Leiden University in 1964 when it was realised [11]. The coldest place in Africa is at the UCT Physics Department in the Nanoelectronics Research Lab, due to its dilution refrigerator. It has a theoretical base temperature of 6 mK and 1100 μW cooling power at 110 mK (see figure 4.1). The manufacturer of the dilution refrigerator Leiden Cryogenic, is a leader in low-temperature techniques.

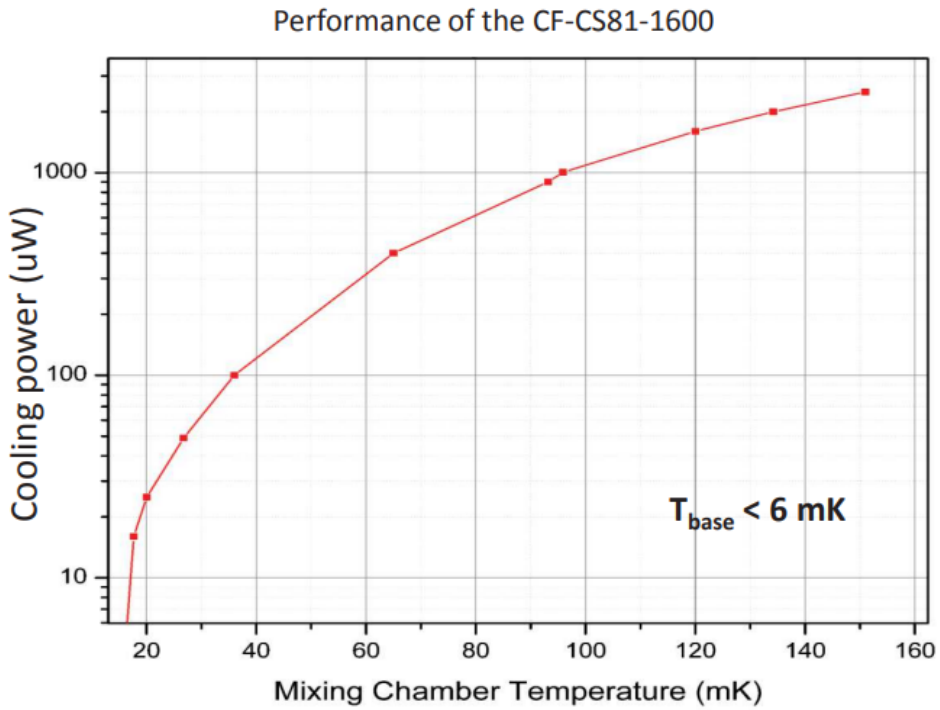

Figure 4.1: Screenshot of the performance graph of the dilution refrigerator model number CF-CS81-1600, showing the base temperature and the cooling power [48].

4.1 Helium Isotopes Phase Diagram

Our dilution refrigerator uses a mixture of ^{3}He/^{4}He to achieve low temperatures. ^{4}He is regarded as a Boson due to its nuclear spin of $I = 0$ (with a boiling point of 4.21 K), while ^{3}He is a Fermion because of its nuclear spin of $I = 1/2$ (with a boiling point of 3.19 K).

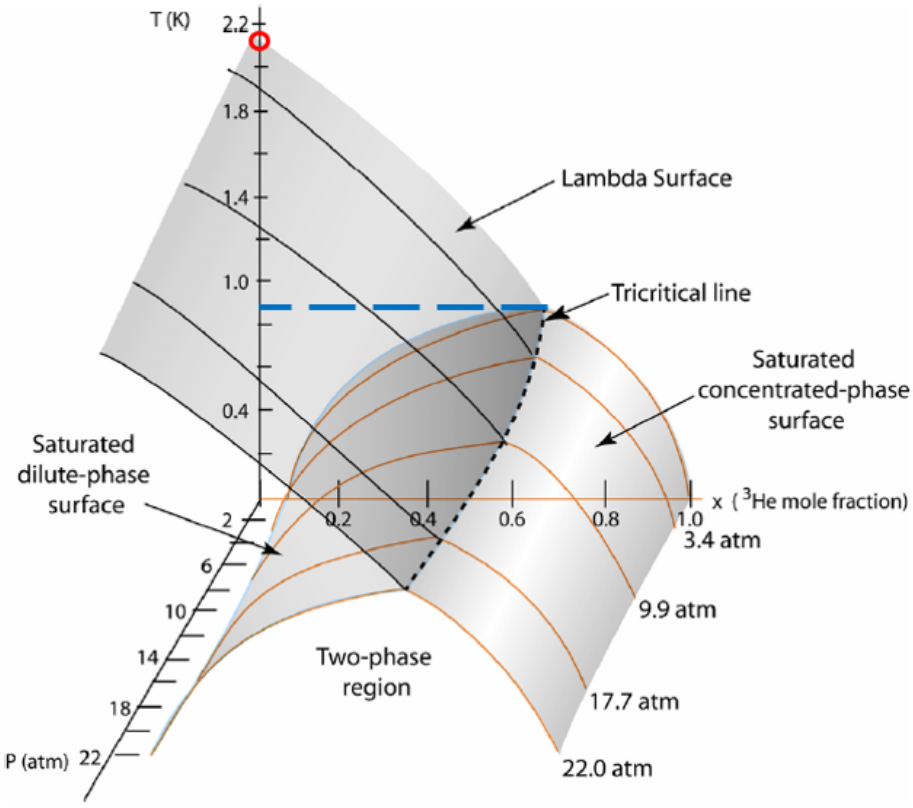

Figure 4.2: Helium phase diagram. Adopted and modified from [8].

Based on figure 4.2, ^{4}He becomes a superfluid at a temperature T = 2.177 K (red circle) at the λ surface, while ^{3}He shows no phase of transition in that temperature range, but at mK ranges superfluid phases are observed. At 0.867 K (blue dash line) the λ surface meets the saturated dilute-phase surface, with $x > 6.6\%$ (where x is the ^{3}He mole fraction), and the phase separation takes place when the temperature is below 0.867 K. ^{3}He will float on top of ^{4}He due to its lower density. This is illustrated by figure 4.4c in section 4.3. The advantage of using liquid helium isotopes in the dilution refrigerator is due to the fact that they have no triple point co-existence and the low temperatures can be maintained for a long period.

Table 4.1: Overview of used temperature Sensors with temperature range [64].

Name	Sensor	Temperature Range
Platinum thermometer	PT 1000	> 10 K
Ruthenium Oxide thermometer	RuO_2	< 30 K
Twin-Temp thermometer	TT	< 6 K
Cerium-Magnesium Nitrate thermometer	CMN	< 300 mK

4.2 Structure and Features

The main components of the dilution fridge are the gas handling system and fridge unit, excluding the pulse tube compressor which works as a helium heat exchange unit (see figure 4.3). The gas handling system constitutes two turbopumps and a scroll pump as well as an upper and lower tank for storing ^{3}He and ^{4}He. Our dilution fridge rests on a four feet table mount on the floor, the fridge can be raised and lowered anytime. The cross-section of the fridge is given by figure 4.3. The Inner Vacuum Chamber (IVC) and Outer Vacuum Chamber (OVC) of the dilution refrigerator are designed in a fashion that prevents unwanted heating via radiation, convection and conduction. All the plates are electroplated with gold. A cold finger known as the tail is connected to the Mixing Chamber (MC) plate and houses the dock where the device is connected. The shuttle containing the sample is "docked" to the dock and remains inside the fridge. The cold finger is at the centre of a superconducting Niobium-titanium (NbTi) magnet with a field up to 10 T. A range of temperature sensors are indicated in table 4.1, and are distributed at strategical locations in the dilution fridge. There are different temperature sensors used for different temperature ranges. The PT 1000, the TT and the CMN are contained in the mixing chamber, they monitor the temperature changes during the cooling of the fridge. RuO_2 is on other plates (see figure 4.3) labelled as 300 K plate, on the still plate and the 50 mK plate.

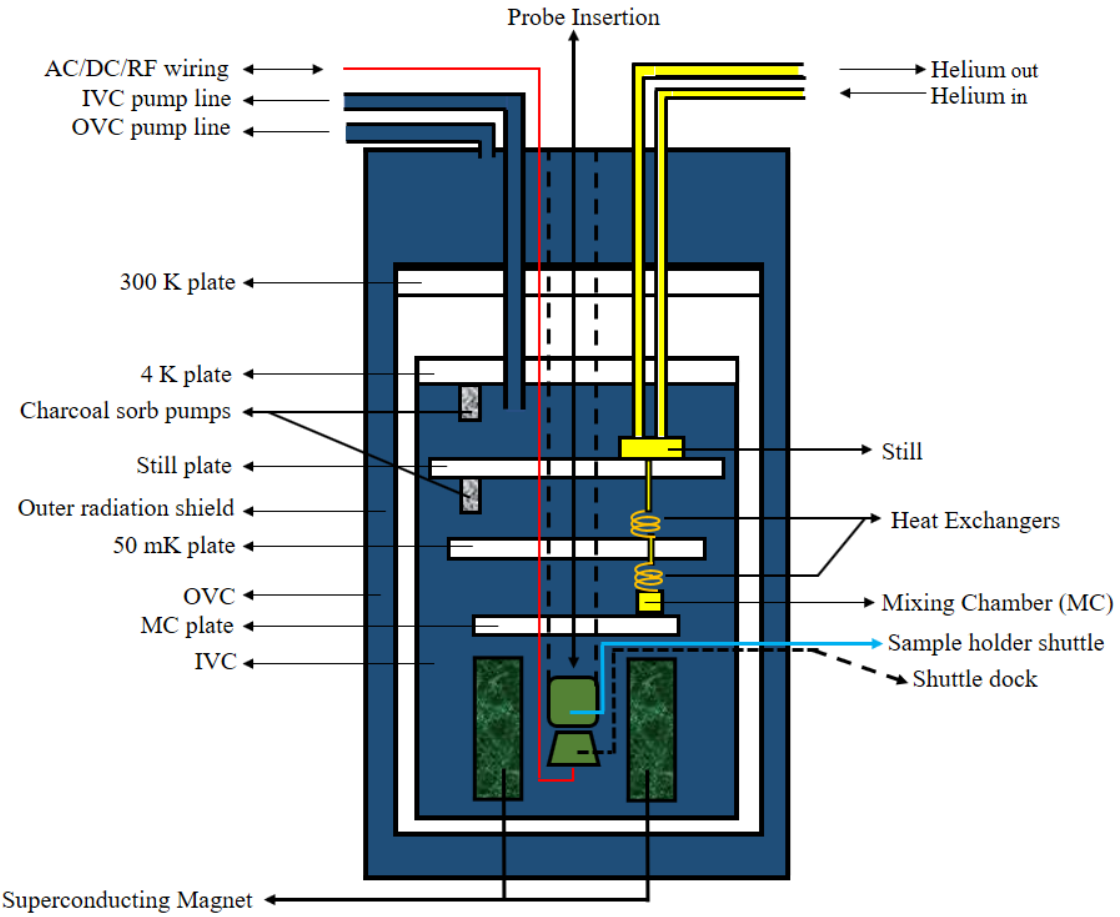

Figure 4.3: General view of the dilution refrigerator. Subsystems indicated by colours: blue - evacuation, yellow - helium, and red and green – electrical.

4.3 Cooling Process

The dilution refrigerator at UCT is operated as a closed cycle system. The cryogen is coupled with the heat exchange unit used to remove heat from the recirculating gas. After closing, the fridge is evacuated. The air in the OVC and IVC is purged utilising a scroll and turbo pump, this aids in avoiding air condensation during the cooling process. With the system purged, ^{4}He gas of 15 mbar is added into the IVC to act as an exchanger gas during cool down. This couples all the thermally isolated plates to the 3 K plate where the pulse tube is bolted. The pulse tube is used to bring the IVC temperature down from 300 K to 4 K (see figure 4.4a). Via Joule-Thomson cooling the volume of ^{4}He expands causing the temperature to drop according to Ideal Gas Law. Once the 4 K plate is at 4 K, charcoal sorb

pumps are used to evacuate the ^{4}He exchange gas in the IVC, this thermally decouples the plates from each other and enables subsequent separation cooling of all the plates. A mixture of ^{3}He/^{4}He (see figure 4.4b) is introduced after the interior reaches 4 K. Subsequent cooling takes place via evaporative cooling at the mixing chamber, where the lowest temperatures can be reached. Here the most energetic molecules of helium in the mixing chamber are preferentially removed.

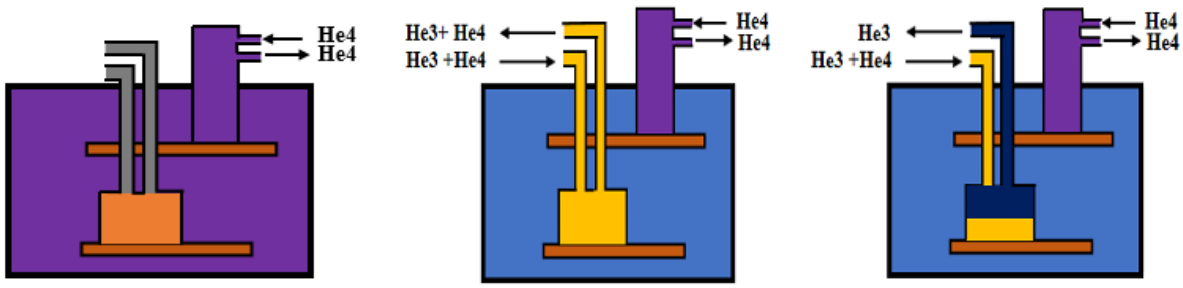

(a) Thermal coupling of the interior.

(b) A mixture introduction of ^{3}He/^{4}He.

(c) Separation of the mixture showing ^{3}He and ^{4}He.

Figure 4.4: The cooling process of the dilution refrigerator illustrated in three-stages.

For the final stage of cooling, the separation of the ^{3}He/^{4}He mixture into two phases must occur. Cooling the mixture down to 800 mK via the turbo-pumps and evaporative cooling, by pumping on the ^{3}He/^{4}He mixture leads to a superfluid transition. Here the mixture separates into two phases ^{3}He rich phase floating on the top of a ^{4}He phase with 4% ^{3}He (see figure 4.4c). Pumping from the bottom (yellow in figure 4.4c) of the mixing chamber, the ^{3}He will preferentially pump implying that the turbo-pump will pump ^{3}He before ^{4}He, this due to the higher ground state energy of ^{3}He atoms over ^{4}He. Pumping away ^{3}He the ratio of the mixture at the bottom of the mixing chamber changes. This leads to a state of equilibrium being lost between the two phases. The equilibrium state is reinstated by ^{3}He (blue in figure 4.4c) diffusing down to balance the ratio, but ^{3}He needs energy to do so. The plate gives away its energy to the mixing chamber, such that ^{3}He changes phase and enters the dilution phase (yellow in figure 4.4c). This results in the plate cooling down to mK temperatures.

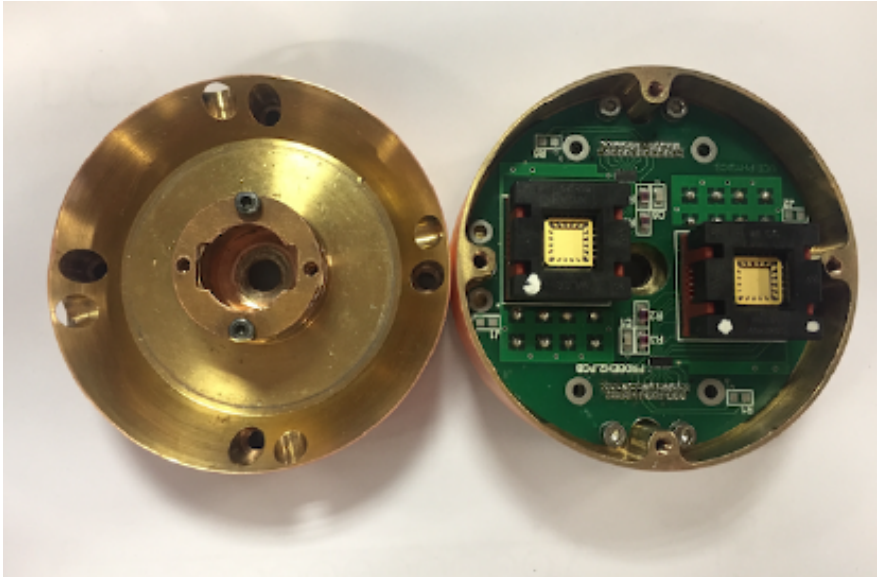

Figure 4.5: Photograph of the shuttle. On top of the shuttle, gaps for the screwing mechanism are visible. Gaps are used for attaching and detaching to the probe. The inside of the shuttle is shown as well, containing two samples (shorting plugs) [64].

4.4 Sample loading and unloading

The LCC carrying the device is loaded into the sample holder shuttle unit. Figure 4.5 is the sample holder shuttle opened, showing the printed circuit board and two sample LCC sockets. After the samples are loaded in the sockets, the shuttle unit is closed. It is then mounted to the bottom of the probe (see figure 4.6, red arrow) of length 1.42 m with a flange-lock mechanism .

Figure 4.6: The probe used to deliver the shuttle to the bottom of the cold finger and secure it to the dock, where the top end is indicated by the yellow arrow, the shuttle in figure 4.5 is attached to the bottom indicated by the red arrow [64].

The probe and the shuttle alignment is important to ensure correct "docking". The probe is attached to the bellows on the top of the fridge platform, it can move up and down via computer control. The bellows and the fridge are separated by a gate valve, which is

manually operated. Two motors are used to operate the probe, one motor for lowering the probe and the shuttle and the other motor to attach and detach the shuttle to the dock. Once the shuttle is docked and unloaded from the probe, the probe is extracted. It takes approx. 6 hours for the fridge to cool back down to 4 K after inserting the shuttle. Once measurements are complete, the shuttle can be removed from the fridge. Following the loading process in a reverse manner, the probe is lowered and attached to the shuttle so that it can be unscrewed from the dock. The probe is then retracted back with the bellows, where it warms up to room temperature after closing the gate valve. The device can be removed from the sample holder. The main advantage of the probe, is that the dilution refrigerator is warmed up to room temperature during sample loading and unloading, this leads to quicker loading and unloading and therefore quicker sample turn around. This probe and shuttle system was designed in the Nanoelectronics group at UCT.

4.5 Experimental Setup: Electrical Characterisation and Measurement Apparatus

This section gives a brief description of the experimental setup, measurement apparatus and data acquisition software used. Quantum effects studied in this thesis are only observable at low temperatures. Measurements on the device were carried out below 800 mK. This minimises the thermal smearing of energy levels allowing quantum mechanical effects to be observed.

4.5.1 Lock-in Amplifiers

In the QHE one desires to measure the voltage across the device while varying the external magnetic field and keeping the source-drain constant (electrical current). Lock-in amplifiers ensure a high signal to noise ratio by locking into a reference signal set by the user. Any signal that enters the lock-in at a different frequency will be rejected [87]. Lock-in amplifiers are used as sensitive voltmeters capable of carrying out phase-locked voltage measurements, where the amplitude of an AC signal at a specific frequency using phase sensitive detection to single out the specific reference frequency and phase is measured. Using a lock-in amplifier requires a reference frequency, which is fixed for a specific experiment. Experiments are excited with a periodic signal at a reference frequency ω_r which is expressed as $V_s \sin[(\omega_s t + \phi_s)]$, where V_s is the signal's amplitude and ϕ_s is the signal's phase. The measured signal is expressed by $V_m \sin[(\omega_m t + \phi_m)]$, where V_m is the measured amplitude, ω_m is the measured

frequency and ϕ_m is the measured phase. A phase sensitive detector is used to multiply the two signals which results in

$$V_{psd} = V_s V_m \sin(\omega_r t + \phi_s) \sin(\omega_m t + \phi_m) \tag{4.1}$$

$$= \frac{1}{2} V_s V_m \cos([\omega_r - \omega_s]t + \phi_s - \phi_m) - \frac{1}{2} V_s V_m \cos([\omega_r + \omega_s]t + \phi_s + \phi_m). \tag{4.2}$$

The multiplied signal is then low-pass filtered, removing all the AC signals at frequencies $(\omega_r \pm \omega_m)$. Low-pass filters are chosen to give a clean output without significantly degrading the reference signal. The signal-to-noise ratio could be enhanced with heavier filtering [82]. When $\omega_r = \omega_m$, the phase sensitive detection voltage V_{psd}, a DC signal is given by

$$V_{psd} = \frac{1}{2} V_s V_m \cos(\phi_s - \phi_m). \tag{4.3}$$

4.5.2 Circuit Setup

The experimental procedure essential for measurements to calculate the Quantum Hall resistance and the longitudinal resistance (SdH resistance) is shown in figure 4.7. The Hall voltage V_H and the SdH V_{xx} were measured across the corresponding terminals of the device used in figure 4.7, with a Stanford Research System SR830. A Stanford Research Systems SR750 current amplifier was used to convert a given electrical current to a potential difference. A constant current was ensured by connecting a 10 MΩ resistor to the circuit in series since the Hall bar resistance is only of the order of kΩ at low temperatures.

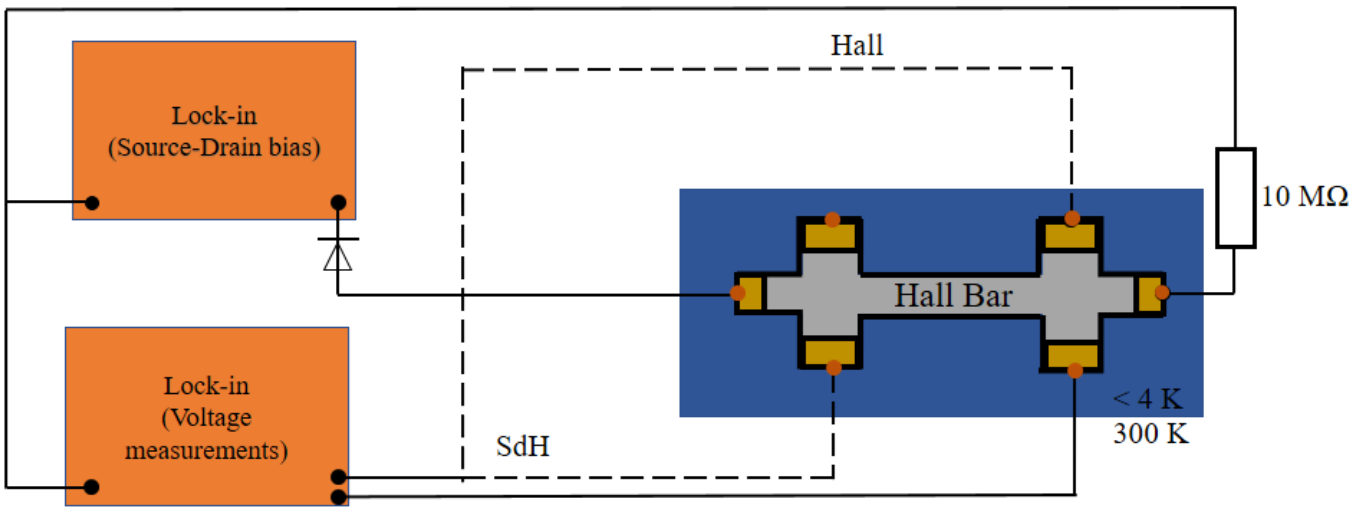

Figure 4.7: Circuit diagram setup to measure Hall and SdH voltage, with the blue region indicating the dilution refrigerator environment, while the 300 K indicating the outside environment.

The lock-in amplifier for the source-drain bias was coupled with the preamplifier to monitor any change in current over the entire experiment. The second lock-in amplifier was used to record the Quantum Hall and SdH voltages during separate runs. Making use of a third lock-in amplifier in the system would allow for the QHE and SdH to be measured simultaneously. The EG & G 7220 lock-in amplifier was used to generate the reference signal and measure the current via the preamplifier with the resultant potential difference measured relative to the reference ground, while the SR830 lock-in amplifier was used to measure the voltage drops across the sample indicated by the chosen Ohmic contacts as shown in figure 4.7. For our measurements, we set the reference frequency at 77 Hz to ensure maximum rejection of the dominating noise in the room, which would be due to the mains power at 50 Hz. A photograph of all instruments used is shown in figure 4.8. PC Communication was possible via GPIB.

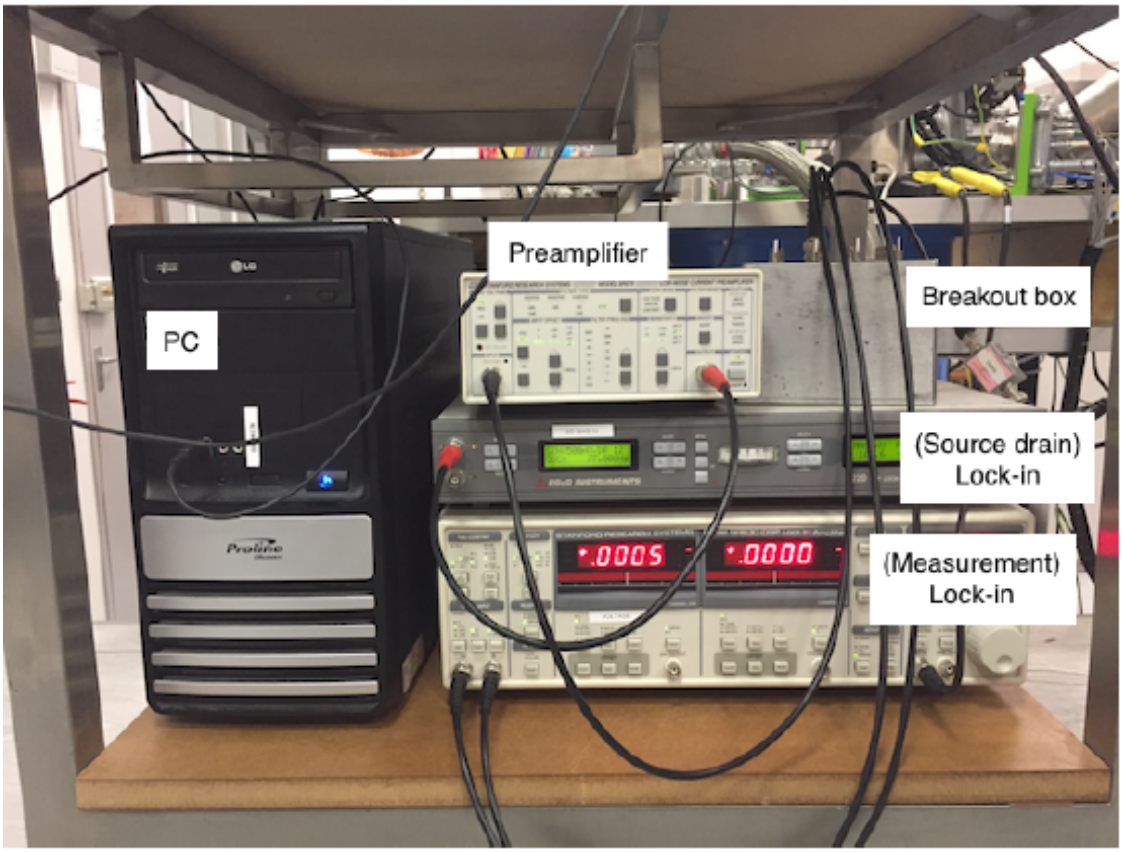

Figure 4.8: A photograph of the instruments used for our experiments, showing both lock-in amplifiers. The Hall and SdH voltages were measured by the (Measurement) lock-in, with the breakout box connecting the device inside the fridge. All the connections of the instruments were made using BNC cables [64].

4.6 Data Collection and Software

The data acquisition software used was LabVIEW based developed at Physikalisch-Technische Bundesanstalt (PTB) and known as Modulab with all the drivers developed at UCT. The software interface is shown in figure 4.9. Modulab was configured to control the reference frequency and reference amplitude of the lock-in amplifiers and take readings from both lock-in amplifiers and set the magnetic field strength. All this was communicable via the GPIB interface. The ramping rate of the magnetic field was set to ensure that quenching of the magnetic field was avoided. Quenching refers to a sudden loss of magnet's superconductivity to a resistive state. Our NbTi magnet tends to superconductor at approximately 10 K. The current at this temperature entering the magnet will superconduct close to zero resistance. The amount of current the magnet can have circulating

in a superconductor is determined by two properties namely the magnetic field it's in and temperature. When the magnet is ramped at a fast rate this induces eddy currents. Eddy currents lead to Ohmic heating and the magnet heating up. When the magnet heats up above 10 K its superconducting properties are lost. The fridge will shut down in this situation to prevent damage.

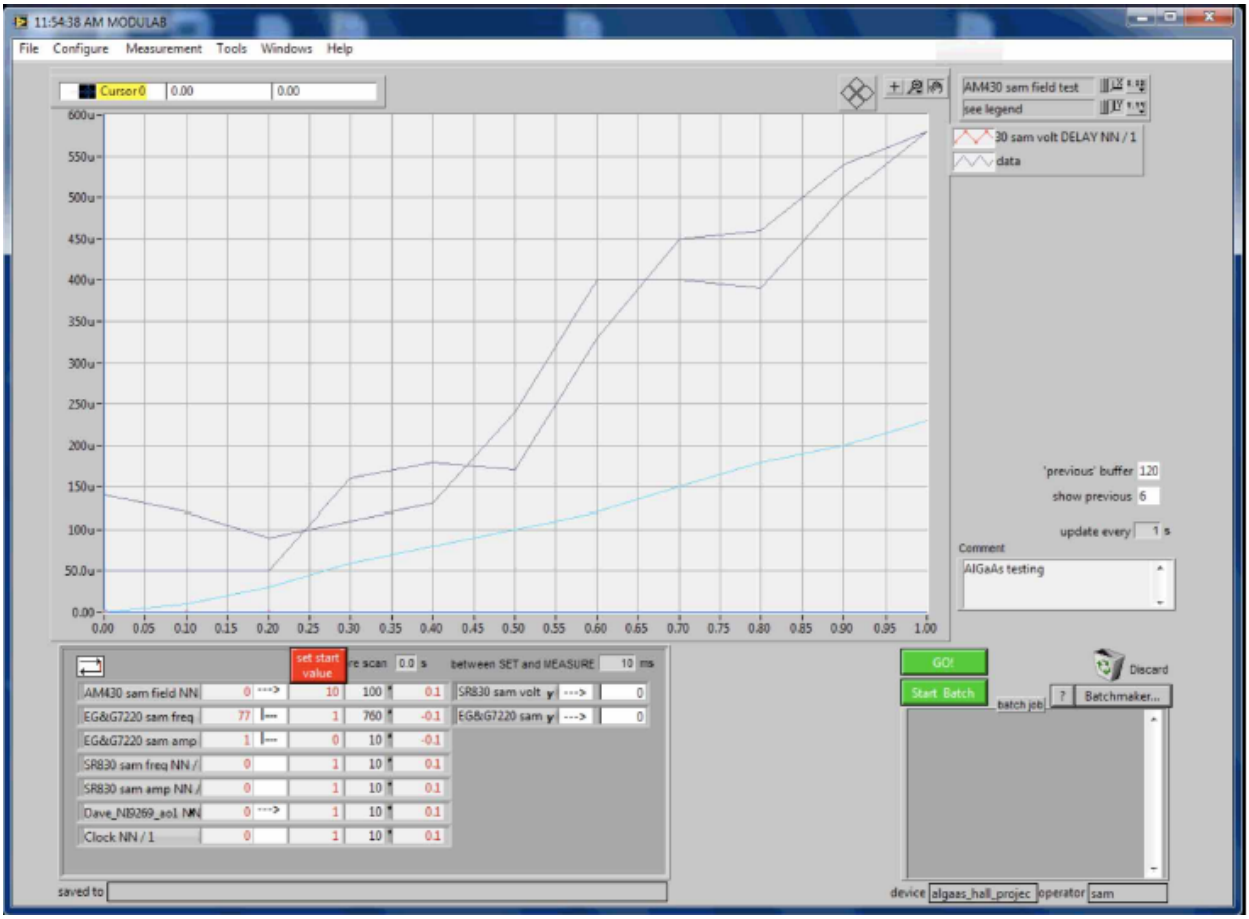

Figure 4.9: The Modulab interface, showing the main graphs with results in real time (cyan colour) and allows comparison with previous (grey colour) results [83].

5 | Chapter 5: Device Measurements and Results

In this chapter, we present results obtained from the measurements that were carried out. The analysis made in this chapter forms the building blocks of the implementation of the quantum Hall resistance (QHR) standard at NMISA and understanding the factors that are crucial for the observation of the QHE to be within the required limits of uncertainties.

Analysis of both the quantum effects (SdH oscillations and QHE plateaus) are presented in this chapter in an AlGaAs/GaAs Hall bar. With the help of applying a constant source-drain bias (electrical current) across the Hall bar, both the Hall and SdH voltages were measured with magnetic field applied in a perpendicular direction to the direction of current flow, the strength of the magnetic field was varied from 0 to 10 T. Hall plateaus at high and low magnetic field as well as SdH oscillations were observed. The data was used to characterise the device by calculating the electron density and mobility, and results were compared with literature. The von Klitzing constant was calculated and compared to literature. Our results presented in this chapter were carried out during the initial stages of the probe and shuttle development and modification. The device was cooled down to approximately 200 mK.

5.1 Measurements of AlGaAs/GaAs Hall Bar

The AlGaAs/GaAs heterostructure to be measured, was a multiterminal patterned (typically 12-terminals) Hall bar. Our electronic measurement setup is outlined in section 4.5.2 in figure 4.7. After placing the device inside the dilution refrigerator, it was cooled to a temperature of around 200 mK. The magnetic field was ramped up to 10 T while measuring the Hall voltage and the magnetic field was ramped back down to 0 T while measuring the SdH voltage. During the process of taking measurements, there was a temperature fluctuation. This was due to Eddy currents. Kittel [39], has stated that eddy currents are a significant source of heating in dilution refrigerators. The heat is due to dissipated current induced by changing magnetic fields. The power dissipated by the current flow in a resistance loop is given by $P = I^2R$ Ohmic heating [39].

The longitudinal and transverse resistances of the sample as a function of the perpendicular magnetic field strength are shown in figure 5.1, both quantum resistances were calculated

via

$$R = \frac{V_{\text{volatge(LIA)}}}{V_{\text{current(LIA)}} \times [\text{preamplifier factor}]}, \tag{5.1}$$

where $V_{\text{volatge(LIA)}}$ is the measured voltage (V_{xy} or V_{xx}), $V_{\text{current(LIA)}}$ is the current, and the preamplifier factor used was $1\,\mu\text{A/V}$ (all instrument settings are given in Appendix A on page 73).

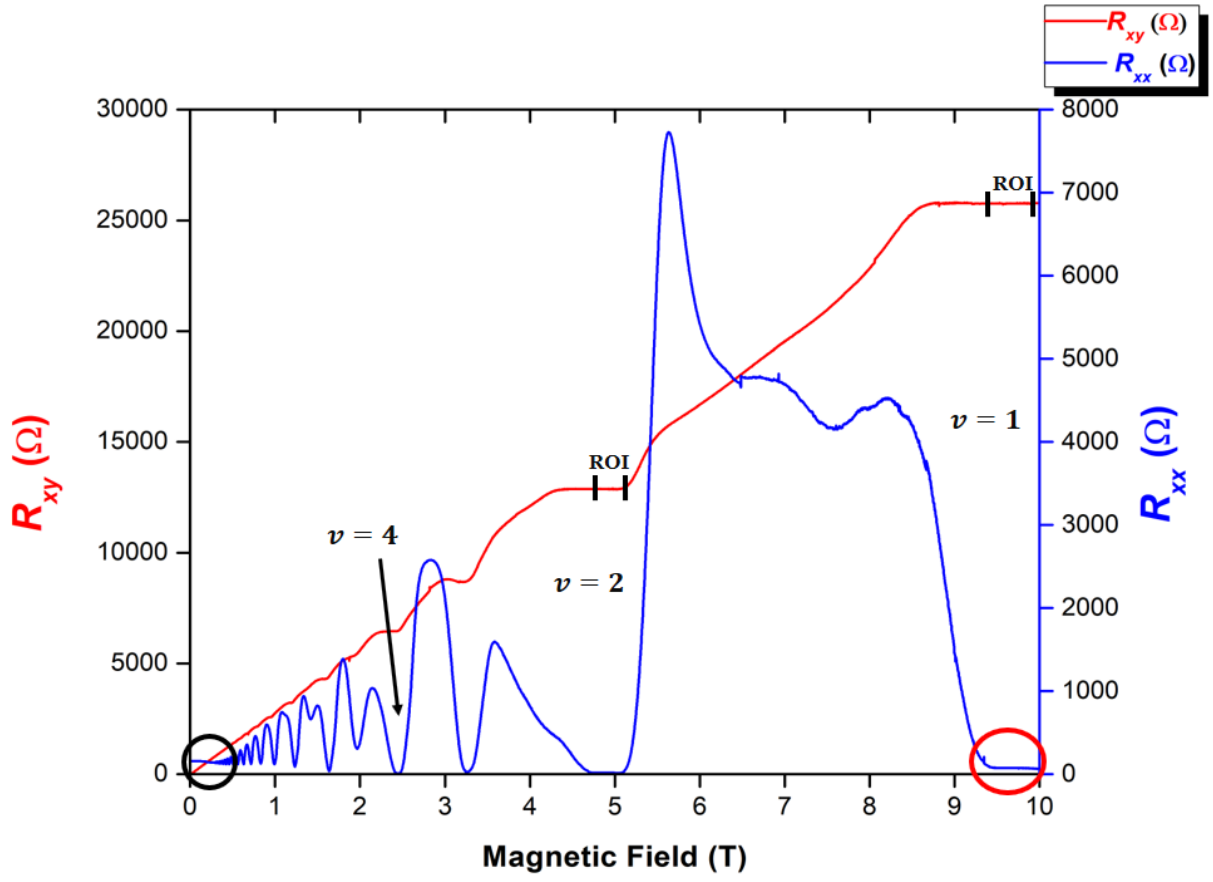

Figure 5.1: The Hall (R_{xy}, red) and SdH (R_{xx}, blue) resistances of an AlGaAs/GaAs heterostructure Hall bar as a function of the perpendicular applied magnetic field. With observable Hall plateaus and SdH oscillations.

What's evident here for both the transverse and longitudinal resistivity, at low magnetic fields (black circle figure 5.1), is that they behave as expected in the classical Hall regime. It's only around 0.5 T where we start to see the formation of the quantum states as seen by the SdH oscillations and the quantum Hall plateaus. A lack of stability was observed

especially at higher magnetic field values. As can be seen in figure 5.1 the observations of non-zero minima in the SdH oscillations (indicated by the red circle) is an indication of destabilisation observed in the high magnetic field. This destabilisation might be associated with temperature fluctuations and high current density.

Table 5.1 gives all the uncertainties which were accounted for. A four terminal measurement was carried out eliminating the resistance of the connecting wires, and only uncertainties associated with the measuring instruments were considered. The majority of these were obtained directly from their technical specification operating manuals.

Table 5.1: Uncertainties of instruments noticed prior to measurements being carried out.

Device	**Source of Uncertainty**	**Value**
SR830 LIA	Reading precision	470 nV
	Measurement Error	0.20 %
	Input noise	5 nV
EG-G7220 LIA	Reading precision	0.1 nV
	Measurement Error	0.50 %
	Input noise	0.5 nV
SR750 preampilifier	Gain accuracy	0.50 %
AM430 magnet controller	Readout precision	0.1 mT

The readout precision of the Lock-in amplifier was dependent on the instrument's sensitivity setting. The sensitivity settings were such as not to overload the lock-in amplifier inputs during the entire experiment. This resulted in a proportionally larger coarse-graining for small voltage measurements that would have been possible if these measurements had been taken in isolation. A triangular probability density function (pdf) was used to account for uncertainties of the readout precision around the corresponding readings. Both noise uncertainties of lock-in amplifiers and the magnetic controller were regarded as negligible, all the included uncertainties were combined at the level of raw data from the voltage readings.

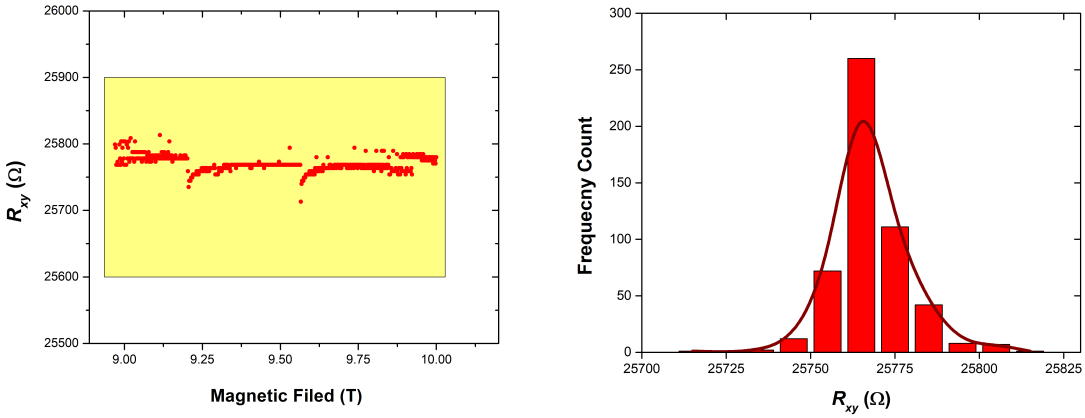

(a) Data points of the region of interest (ROI) for plateau $v = 1$, the dataset extracted from figure 5.1.

(b) Histogram of the Hall resistance values of the data points in figure 5.2a.

Figure 5.2: Both above figures are analysis for the $v = 1$ plateau for Hall resistance data.

5.2 Hall Resistance Analysis

Observing figure 5.1, it is possible to calculate the von Klitzing constant

$$R_H = \frac{h}{ve^2} = 25\,812.807\,\Omega. \tag{5.2}$$

In our case, we have determined the average resistance at each plateau in figure 5.1 and multiplied by the fitting Landau level index v. The von Klitzing constant is given by equation 5.2 as discussed in subsection 2.3.2, and it can be used to determine and improve the accuracy of the fine structure constant α [40; 57]. α and $\frac{h}{e^2}$ are related by the defined quantities $\frac{h}{e^2} = \frac{\mu_0 c}{2\alpha}$ both having the same relative uncertainty [72].

The length of each plateau was estimated directly from the graph in figure 5.1. Data points in the ROI of the first plateau ($v = 1$), along with a histogram of the Hall resistance (which is used for representation of the data distribution and also to give of a sense of the density of the distribution of the data based on the ROI) are shown in figure 5.2a and figure 5.2b.

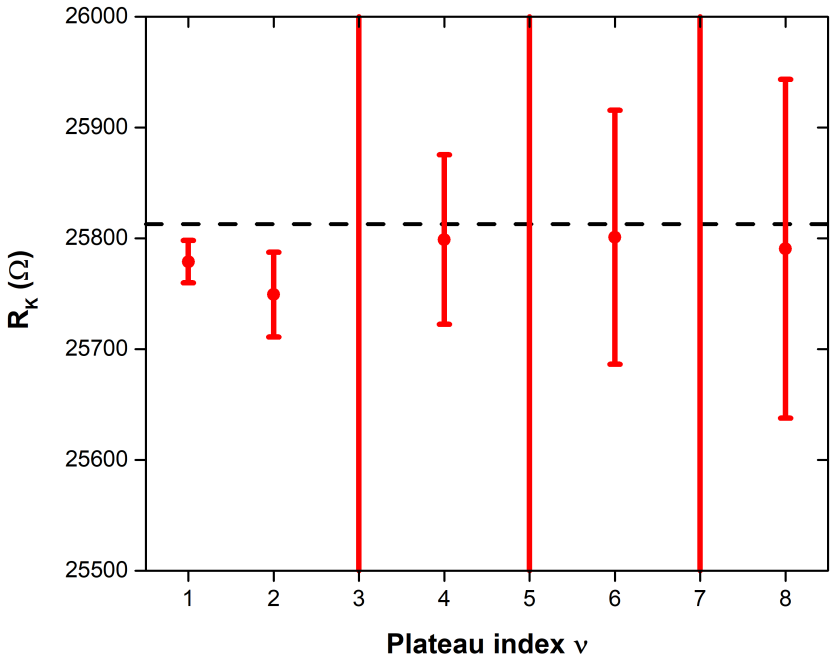

Figure 5.3: Averages of resistance values from ROI datasets (from figure 5.1), multiplied by the plateau v and compared to the von Klitzing constant R_K represented by the black dotted line.

The analysis of each plateau was carried out separately (each dataset is specifically given by $v = \{1, \ldots, 8\}$ indicated in figure 5.1). All R_K values in figure 5.3 were estimated by averaging all Hall resistance values falling within the limits of the plateau and then multiplied by the appropriate Landau level index v. Figure 5.3 shows the R_K estimated values, which are compared to the recommended value by the CIPM (black dotted line). A certain degree of destabilisation was observed as mentioned above in figure 5.1 on the dataset plotted, this was perceived in plateaus coinciding with Landau level index $v = 3$, 5 and 7 which do not flatten out to any significant extent to become plateaus, the uncertainties are too large relative to what is expected. The non-at nature of these plateaus is due to the broadening effect stated by Qiu *et al.* [60]. The average von Klitzing constant is 25 783.634 Ω with the standard deviation of ±21.112 Ω when all the plateaus (v =1,2,4,6 & 8) that can be used for resistance standard are considered. Plateaus v =3, 5, & 7 were not included because they are out of the von Klitzing constant range. The accuracy of all the datasets is obtained from $(\frac{h}{e^2} - R_{(\mathrm{AlGaAs/GaAs})})/(\frac{h}{e^2})$ and is equal to 1.13×10^{-12}. The average von Klitzing constant is weighted down by the temperature destabilisations that were mentioned earlier.

5.3 Shubnikov-de Haas Oscillations Analysis

The importance of SdH oscillations in this study was to grant an opportunity to characterise the sample by determining the 2DEG electron density (n_{2D}) and mobility (μ) which are obtainable via the relationship given by equations 2.10 and 2.13.

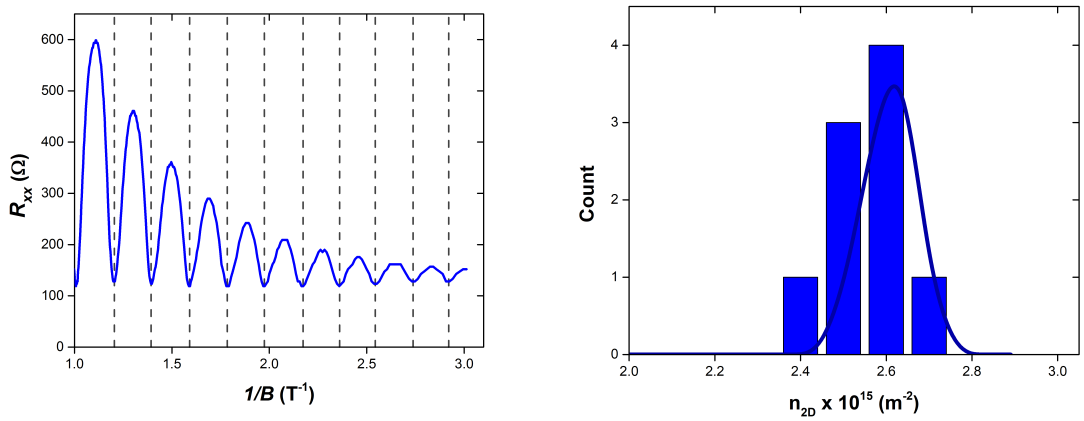

(a) Low-field SdH Oscillations data shown here is a subset of the full dataset in figure 5.1, the minima of resistance are indicated by dashed vertical lines.

(b) Histogram of calculated n_{2D} values for adjacent minima in figure 5.4a.

Figure 5.4: SdH oscillation minima analysis, the periodicity of the minima figure 5.4a is utilised to obtain the 2DEG electron density.

From figure 5.4a a pair of minima gives an estimate of n_{2D} by utilising equation 5.3. After obtaining n_{2D}, it is possible to calculate the μ using equation 2.13.

Rearranging equation 2.10, we get the following:

$$n_{2D} = \frac{2e}{h\Delta(\frac{1}{B})} = \frac{4.83 \times 10^{14}}{\Delta(\frac{1}{B})}. \tag{5.3}$$

A single sweep of B field up to 10 T, yields several SdH oscillations, which can be plotted against gate voltage if a top gate is present, magnetic field or inverse of the magnetic field. In our case, we were varying magnetic field such that our SdH oscillations are plotted against the inverse of the magnetic field. Strong SdH oscillations with a period $1/B$ are completely developed at a magnetic field less than 3 T, however glancing at high magnetic field, no

pronounced oscillations can be observed, due to lower mobility (see figure 5.1). The research project was limited to n_{2D} and μ calculations.

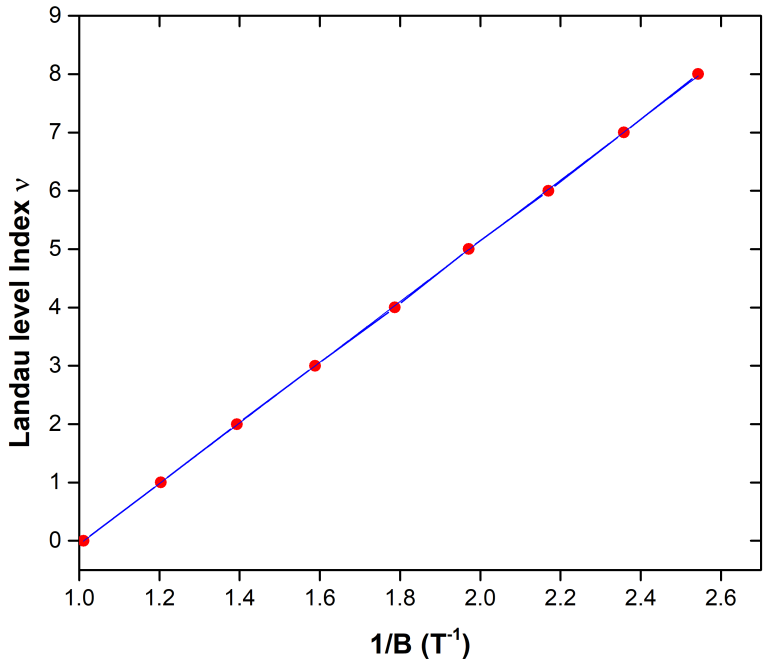

Figure 5.5: Landau fan diagram, dataset extracted from figure 5.4a. Each data point (colour = red) represent a minima in oscillation amplitude.

In the SdH measurements the Fermi level E_F will move as explained in subsection 2.3.2 as the density of electrons remains fixed, this results in $1/B$ period oscillations. By measuring V_{xx} we can get $\Delta(1/B)$ from the ramped magnetic field and we can make a plot of R_{xx} against $\Delta(1/B)$ or B (see figure 5.4a). The Landau fan diagram is shown in figure 5.5 by plotting, Landau level index v against the values of $1/B$ where the minima of R_{xx} occurred, all the data points fall onto a line that can be extrapolated towards the zero intercept indicating the standard phase of oscillations in figure 5.4a.

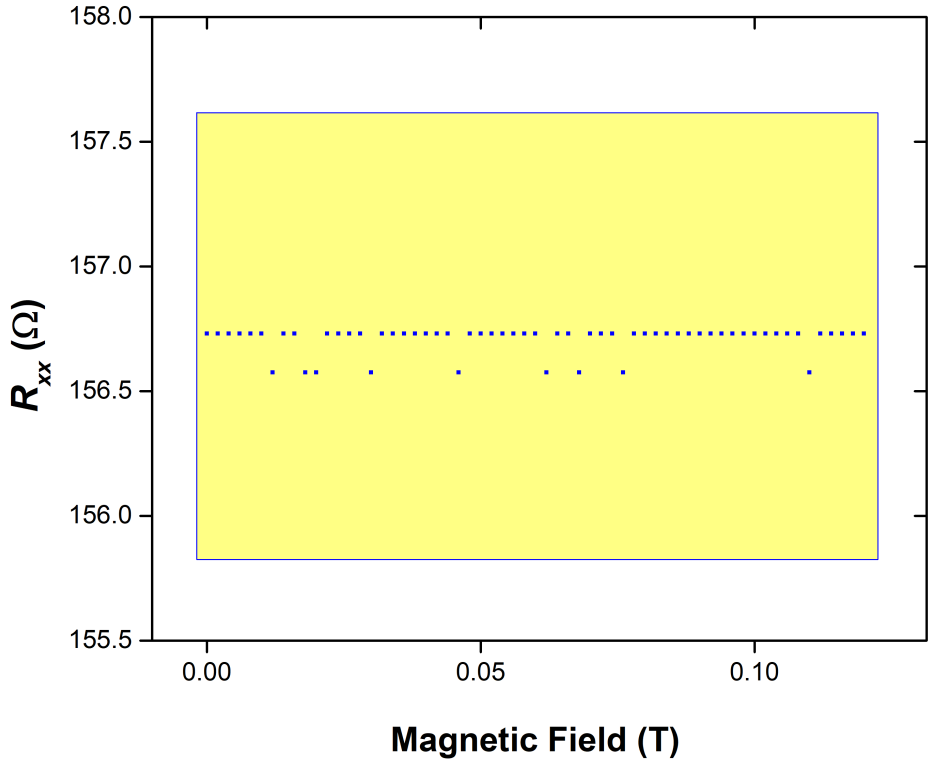

Figure 5.6: Extremely low-field SdH resistance (from figure 5.1) with 1σ uncertainty shown by shading, data utilised to estimate zero field SdH resistance value.

Figure 5.6 shows data for the low magnetic field regime of the SdH oscillations. Clear constant linear behaviour with no oscillations is observed. This is the classical Hall effect and links to the theory discussed in subsection 1.2.1. It is only at low magnetic fields in such low dimensional systems that this is observed. At higher magnetic fields the quantum mechanical effects dominate. the 1σ uncertainty is illustrated by the shaded yellow region.

Due to noise, such as the 50 Hz mains power (that cannot be avoided) in nanoelectronic experiments of this nature, the oscillations had to be enhanced by directly measuring V_{xx} with a lock-in amplifier. The observed SdH oscillations are due to the Landau quantisation of the 2DEG in the channel. Observing from figure 5.1 and figure 5.4a, when the magnetic field is greater than 3 T the oscillations become weak. This is caused by "parallel conduction" in the heavily doped AlGaAs layer. The signature of parallel conduction is that the minima in R_{xx} does not vanish to zero in the quantum Hall limit [24]. As expected the resistance is independent of B. The oscillation period is independent of temperature and the amplitude

manifests as a diminishing trend [60] rising with the inverse of the magnetic field (see figure 5.4a).

Table 5.2: Summary of the results for the AlGaAs-GaAs material characterisation analysis from the SdH resistance data and the results are compared with other research results of similar parameters used.

	Our work	[9]	[84]	[2]
Temperature (K)	0.20	1.5	1.5	0.27
$n_{2D} \times 10^{11}\,(\mathrm{cm}^{-2})$	2.27	7.5	1.7	1.8
$\mu \times 10^{5}\,(\mathrm{cm}^{2}\mathrm{V}^{-1}\mathrm{s}^{-1})$	3.9	18.9	12.0	16.0

As mentioned in section 5.1, temperature can have an effect on the Hall resistance. But surprisingly, for the SdH oscillations dataset, the temperature did not affect the low-field regions as seen is by the well-developed oscillation minima in figure 5.4a. The characterisation results on the device are shown in table 5.2 where they are compared with values obtained by other researchers of a similar study and experimental conditions but different wafers. From the analysis of the SdH oscillations, it is evident that the n_{2D} and μ are robustly dependent on factors such as dopant concentration and temperature. However, Saku *et al.* have mentioned that the dopant concentration may not be highly important for the n_{2D} if other structural parameters are adequately optimised [63].

5.4 Summary

Strong 2D confinement was realised due to the observations of quantum effects. The QHE was observed in AlGaAs/GaAs for the first time at UCT and well developed SdH oscillations were probed under low-field regions. Our work attested the intriguing electronic structure of AlGaAs/GaAs through quantum transport and demonstrated the high quality of the 2DEG material system which may be appropriate for the quantum Hall resistance measurement system. Under scrutiny, our Hall resistance results lack stability. The n_{2D} obtained was $2.27 \times 10^{11}\,\mathrm{cm}^{-2}$ and the μ was $3.9 \times 10^{5}\,\mathrm{cm}^{2}\mathrm{V}^{-1}\mathrm{s}^{-1}$. Observing Table 5.2, our n_{2D} is higher than the wafers used in reference [84] and [2], but it comes at the expense of having low μ. Our sample has both low μ and n_{2D} when compared with reference [9], which is an impressive wafer with both high μ and n_{2D}.

6 | Chapter 6: NMISA DC Resistance Measurement System and Measurements

This chapter gives a brief description of the National Metrology Institute of South Africa's (NMISA)'s DC resistance measurement system. NMISA is currently running a project to implement the quantum Hall resistance (QHR) standard based on the QHE. Studying the present NMISA DC resistance measurement system will inform on how the present system performs in terms of stability, drift, and temperature dependence of the standard resistors. This will help inform on the key requirements for the new quantum Hall system to ensure a clear and smooth traceability chain for the final resistance standard system. We will present results taken during a research visit to NMISA where we calibrated standard resistors (oil type) from 1 mΩ to 1 kΩ. We monitored their stability, drift per day, and calculated the resistance deviation from the nominal value, then interpreted the results graphically. Air type standard resistors where calibrated to obtained their temperature coefficients.

6.1 Background

NMISA was established under the Measurement Units and Measurement Standards Act No 18 of 2006 [54]. The institution is responsible for maintaining the SI units and to maintain and develop primary scientific standards of physical quantities for South Africa and compare those standards with other national standards to ensure global measurement equivalence. The institute furthermore must provide reference analysis in the case of a measurement dispute and maintain and develop primary methods for chemical analysis to certify reference materials for South Africa and the region [54]. Maintaining national standards in accordance with different ISO/IEC procedures.

6.2 Procedure

The procedures for calibrating the DC standard resistors is compiled in a way that ensures competence. Every detail is outlined well in the calibration systems manuals [50]. The operation of the system can be found in Appendix B (on page 74). NMISA have three automated primary resistance bridges with model numbers: 6010D, 6010C and 6000B. All the automated resistance bridges can establish a ratio of two resistors and assign a value to the unknown resistor based on the value of the reference standard resistor. The 6010D

resistance bridge is designed for both resistance metrology and thermometer applications. Ratios allowed by the automated resistance bridges are as follows: 1:1 and 1:10, if a 1 Ω reference standard resistor is used for calibration. Note for the 1:1 ratio measurements, equal currents will flow through the reference standard resistor and the Unit Under Test (UUT). For a 1:10 measurements if 1 Ω reference standard resistor is used to calibrate a 10 Ω UUT, current 10 times greater will flow in the reference standard resistor.

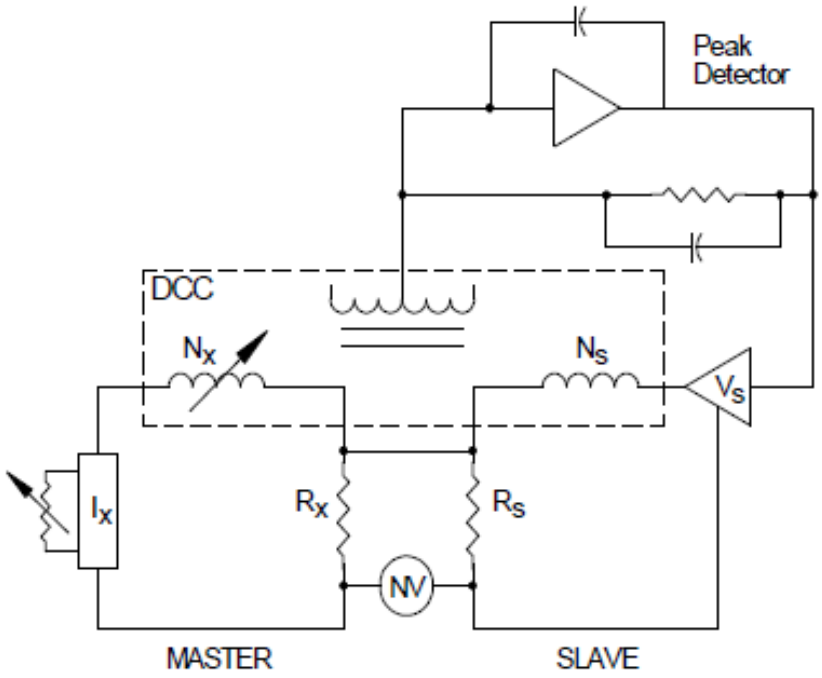

Figure 6.1: Illustration of the resistance ratio bridge block diagram [6]

6.2.1 Automated DC Resistance Bridge

The resistance ratio bridge is a standalone primary resistance measuring system equipped with a Direct-Current-Comparator (DCC). Figure 6.1 illustrates a resistance ratio bridge block diagram. One can see the system is made-up of the primary/master and secondary/slave section. The standard resistor R_X represents the UUT, R_S represents the reference standard resistor that we will be using to calibrate R_X. Both the master and the slave contains a coil, with N_X turns in the master and N_S turns in the slave. N_S is fixed and N_X is changed accordingly or can be changed. The system contains a current source which provides current I_X to the master and a voltage source V_S is used to supply the slave current I_S. The DCC is utilised to obtain an ampere-turn between the primary/master and the

secondary/slave windings by adjusting the primary/master (N_X) and the secondary/slave current (I_S) to achieve zero flux between two standard resistors. The automation balancing facilitates the operation of the bridge by using a current source for the primary/master supply and a voltage source for the secondary/slave supply. A balanced DCC is expressed as

$$I_S N_S = I_X N_X \Rightarrow \frac{I_S}{I_X} = \frac{N_X}{N_S}. \tag{6.1}$$

The relationship between the two currents and the windings is given by equations 6.1 and this implies that in terms of standard resistors equation 6.1 becomes

$$R_X N_S = R_S N_X \Rightarrow R_X = \left(\frac{N_X}{N_S}\right) R_S. \tag{6.2}$$

The advantage of the resistance bridge is that only the primary and reversal rate is needed to be set by the user and simultaneously N_X and I_S balances automatically.

6.2.2 The Calibration Method for 4-terminal Standard Resistors ($0.001\,\Omega$ to $0.1\,\Omega$)

The experimental setup is given by figure 6.2. A model MIL 6010D (Automated DC Resistance Bridge) is used in conjunction with the following apparatus: Low Thermal Four Terminal Matrix Scanner model 4220A/30, MIL 6011B 100 Ampere Range Extender and the Linear DC power supply model 6100A. The measurement system is connected to Measurements International (MI) 6010SW software -Version 1.8.2 via a GPIB USB IEEE-488. The power supply is used to produce current (I_X) which is sent to the primary turn switch. The system control software sets the required N_X turns. I_S is used to balance the comparator which is produced by the salve voltage source.

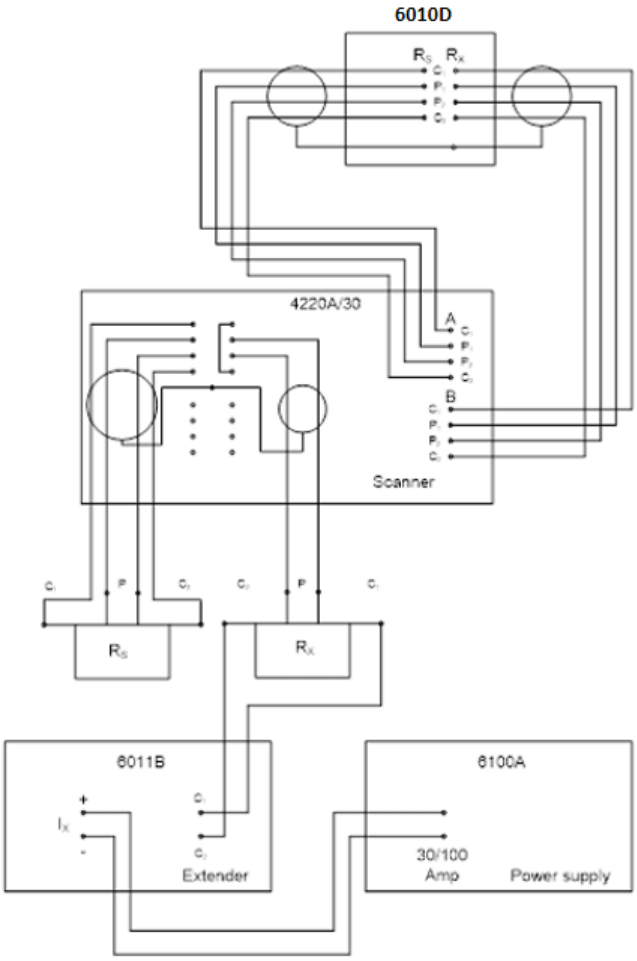

Figure 6.2: Circuit diagram for calibrations of less than 1 Ω standard resistors [38].

I_X is reversed which helps in eliminating thermal voltages. This leads to an equal and opposite current in the primary (master) and secondary (slave) of a DCC, and zero flux is achieved. From this point, measurements can be taken. The R_X value is achieved by calculating the ratio against R_S as R_X/R_S, after obtaining the ratio using equation 6.2 we get R_X. Verification of the measurement system is undertaken by measuring a characterised reference standard resistor and the results compared with the certified value of the reference standard resistor used [38].

6.2.3 The Calibration Method for 4-terminal Standard Resistors (1 Ω to 10 kΩ)

A automated DC Resistance Bridge model 6010C is used in conjunction with a MIL Low Thermal Four Terminal Matrix Scanner Model 4220A/30, the measurement system is connected to MI 6010 Software-version 7.2.3 A via a GPIB USB IEEE-488. The circuit

diagram is shown below:

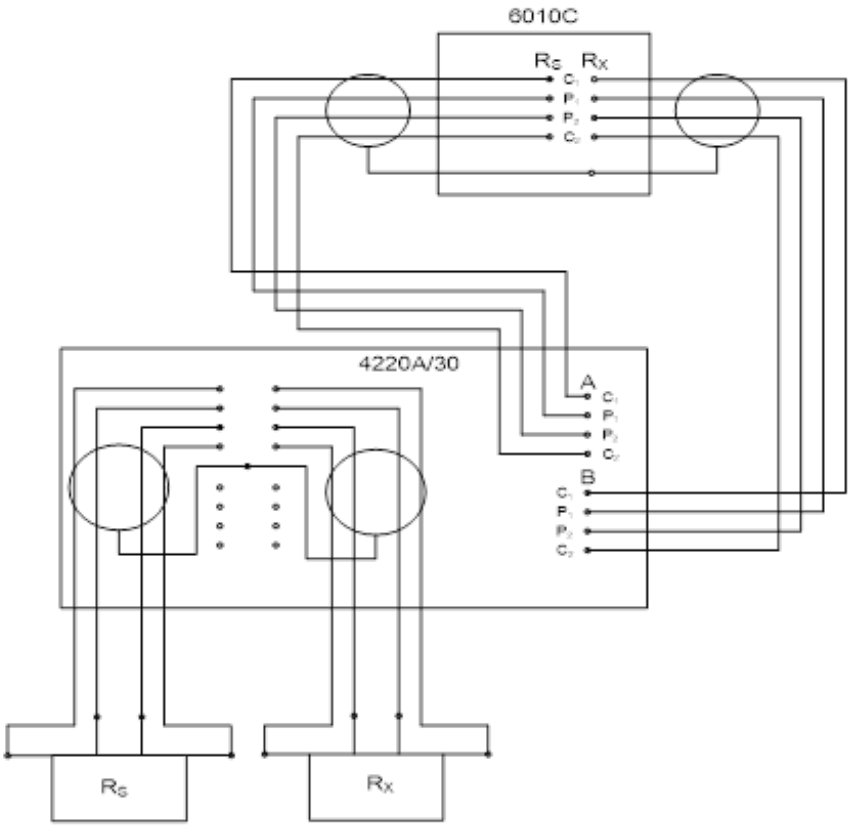

Figure 6.3: Circuit diagram for calibrations of 1 Ω to 10 kΩ standard resistors [50].

Since we mentioned that a automated resistance bridge is a standalone device, the 6010C is suitable for standalone operations for calibrating 1 Ω to 10 kΩ standard resistors. The bridge is coupled with a matrix scanner and measurements are carried out as mentioned in subsection 6.2.2. Verification of the measurement system is undertaken by measuring a characterised reference standard resistor and the results compared with the certified value of the reference standard resistor used [50].

6.3 Temperature Coefficient Determination

Every standard resistor is manufactured with its own temperature coefficient, so metrologists can use it to reduce the uncertainty of their measurements system. To determine the temperature coefficients of air standard resistors, the method in section 6.2.3 was used to calibrate the standard resistors, but in this case the UUT $R_X$was placed inside an air bath and the temperature of the air bath model 9300A was varied from 18 °C to 28 °C with an increment of 0.5 °C. By using appropriate equations we can determine the temperature

coefficients. Applying temperature corrections to standard resistors after calibrations lead to the achievement of low uncertainties of resistance measured values as mentioned above. To apply the temperature corrections, we need the temperature coefficients, α and β. This is simply because the calibrations on the UUT are dependent on keeping the measurement procedure uncertainty within the minimum standard requirements [27].

α and β are mathematical constants linked with the standard resistors, where they are defined as a resistance change per degree of change in temperature. Temperature characterisation of standard resistor due to resistance change is given by

$$R_T = R_{ref}[1 + \alpha(T - T_{ref}) + \beta(T + T_{ref})^2], \tag{6.3}$$

where R_T is the resistance at the measured temperature, T is the temperature in degree Celsius, R_{ref} is the resistance of the standard resistor at the reference temperature, T_{ref} is the reference temperature, α is given by ppm per degree Celsius and β by ppm per square degree Celsius. From the Fluke instruction manual of the 742A Series standard resistors, their temperature coefficients are established when they are calibrated at temperatures 18 °C, 23 °C and 28 °C by using both equations below

$$\alpha = \frac{(R_{28} - R_{18})}{\Delta T} \quad \text{and} \quad \beta = \frac{\frac{(R_{28}+R_{18})}{2} - R_{23}}{\left(\frac{\Delta T}{2}\right)^2}. \tag{6.4}$$

All the results obtained are discussed in the section below.

6.4 Measurement Results

In this section, we have analysed the results of all standard resistors that were calibrated at NMISA during the time spend when visiting for vacation work. The full calibration was done during December 2017 and January 2018. The majority of the standard resistors calibrated are oil standard resistors which are kept in an oil bath of standardisation and kept at the same temperature. Air standard resistors were calibrated for temperature coefficients in section 6.4.4.

The results are analysed quantitatively by using the statistical techniques such as Gaussian probability density function (also known as Gaussian pdf's). We then calculated the average for each measurement set and averaged the final results. Standard deviation and

Experimental Standard Deviation of the Mean (ESDM) was then calculated. We converted the ESDM to ppm, then imported the ESDM (ppm) into the Uncertainty Budget Matrix (UMB). The UMB automatically calculated the combined uncertainty as mentioned in appendix section 5. The accepted uncertainties for our standard resistors can be referred to in Appendix C (on page 88) (Annexure A). Item 2.1 and 2.2 are accredited by the South African National Accreditation System (SANAS) [49].

6.4.1 Analysis of Standard Resistors Resistance

Table 6.1: Results of all less than 1 Ω standard resistors calibrated.

SERIAL NUMBER	NOMINAL VALUE	NOMINAL TEST CURRENT	MEASURED RESISTANCE	UNCERTAINTY (±)
133665	1 mΩ	5 mA	0,999 902 mΩ	6×10^{-6}•R
101810	10 mΩ	5 A	10,001 13 mΩ	2×10^{-6}•R

Table 6.2: Results of all less than 10 kΩ standard resistors calibrated.

SERIAL NUMBER	NOMINAL VALUE	NOMINAL TEST CURRENT	MEASURED RESISTANCE	UNCERTAINTY (±)
098707	1 Ω	50 mA	0,999 982 2 Ω	$0,2 \times 10^{-6}$•R
143625	10 Ω	5 mA	9,999 874 Ω	$0,3 \times 10^{-6}$•R
150539	100 Ω	0,5 mA	99,996 23 Ω	$0,4 \times 10^{-6}$•R
128767	1 kΩ	0,05 mA	1,000 0321 kΩ	$0,7 \times 10^{-6}$•R
		0,5 mA	1,000 0321 kΩ	$0,5 \times 10^{-6}$•R

Table 6.1 and table 6.2 shows the resistance values obtained from the calibration of the standard resistors, from 1 mΩ to 1 kΩ using measurements systems described in subsections 6.2.2 and 6.2.3 respectively. Both tables have five columns namely: serial number, nominal value, nominal test current, measured resistance and uncertainty. Table 6.1 lists the results for 1 mΩ to 10 mΩ standard resistors. The values measured at 23 °C with nominal test currents of 5 mA and 5 A listed in column two. The resistance values in column four are simple mean values of the 25 measurements taken per each set of calibration. Column five lists the uncertainty (±) of the resistance values obtained. Table 6.2 lists the measurement data for the 1 Ω to 1 kΩ standard resistors, in a form like that of table 6.1.

Since all the standard resistors are kept inside an oil bath the temperature of the oil is monitored by placing a platinum resistance thermometer (PRT) inside the oil bath. This is connected to a Keysight 34401A digital multimeter to measure the resistance on the PRT during measurements.

$$T(^{\circ}\mathrm{C}) = 23 + (23.1 - 23) \times \frac{(R - 108.969)}{(109.008 - 108.969)}. \tag{6.5}$$

Equation 6.5 is used to convert the resistance of the oil measured with the PRT into the temperature of the oil, where R is the resistance of the oil. For our measurements, the temperature must be maintained to (23 ± 2) °C. The measured temperature during our measurements was (23.00 ± 0.002) °C which shows that it is within the accepted temperature ranges for resistance calibrations. The expanded uncertainty of measurements was obtained by the import of the standard deviation or the ESDM (ppm) into the UMB, where they were multiplied by a coverage factor of $k = 2$ with a level confidence of 95.45 %. According to Hogan [31], with a 95.45 % confidence interval, we want 95 measurement results out of 100 to be within the limits of your uncertainty estimates. With a 95.45 % confidence, we are accepting a 1 in 20 failure rate.

6.4.2 Monitoring Stability of Standard Resistors

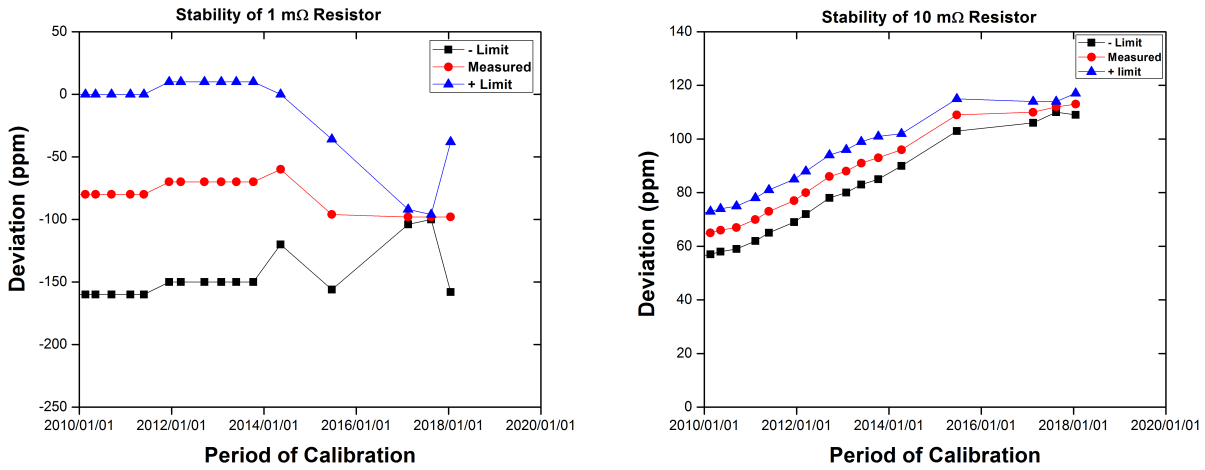

(a) Stability of 1 mΩ

(b) Stability of 10 mΩ

Figure 6.4: Both graphs 6.4a and 6.4b illustrate the stability of less than 1 Ω standard resistors, the red graphs represents the measured value of the standard resistor, while the blue and the black graphs represents the calculated deviation from the nominal value of the standard resistor.

All the graphs illustrated from figure 6.4a to figure 6.5e are plotted to monitor the stability of working standard resistors as a function of time. This is achieved by calculating the deviation of the calibrated standard resistor value from the nominal value of the standard resistor. The upper and lower limit values of the deviation which are presented by the red and the black graph respectively are then calculated. All these values are reported in parts per million (ppm). From the results, since the year 2010, the resistance values obtained from calibrations were constant until 2015. After 2015 the resistance values obtained from calibration showed some fluctuation. This fluctuation in standard resistors is due to overheating of the oil bath. In general, the stability of, or predictability of, the standard resistors varies greatly [15], this is evident by observing figure 6.4a to figure 6.5e. Even though the resistance value changed due to overheating, the temperature detected with the PRT is safe and within acceptable range for calibrating the standard resistors. The overheating of the oil may have been caused by the Lab ventilation system not cooling the lab properly.

6.4.3 Monitoring Drift Rate per Day

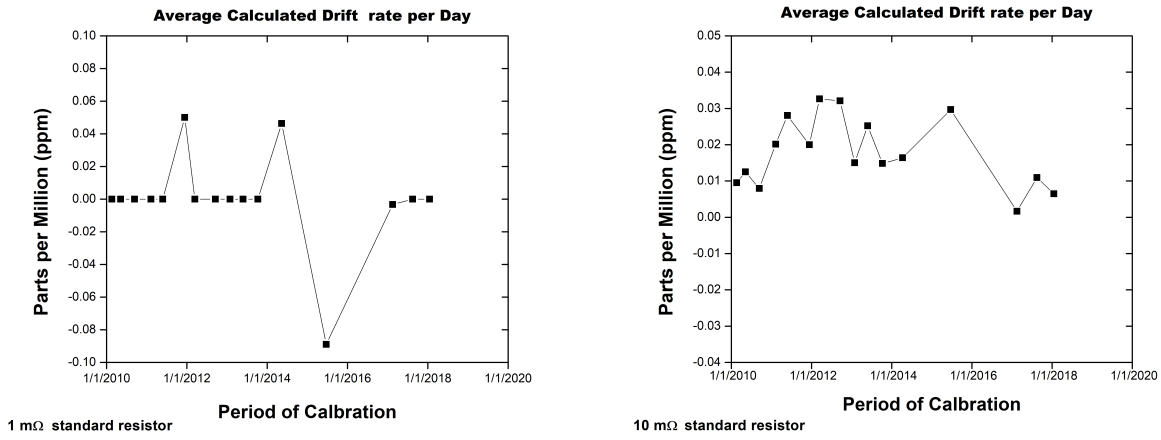

(a) Drift rate per day of 1 mΩ

(b) Drift rate per day of 10 mΩ

Figure 6.6: Both graphs 6.6a and 6.6b illustrate the drift rate per day since the last calibration date of less than 1 Ω standard resistors.

The graphs plotted from figure 6.6a to 6.6b above and in figure 6.7a to 6.7e below shows the averaged calculated drift per day, which is calculated from the number of days since the last calibration divided by the difference between the last deviation and newly calculated

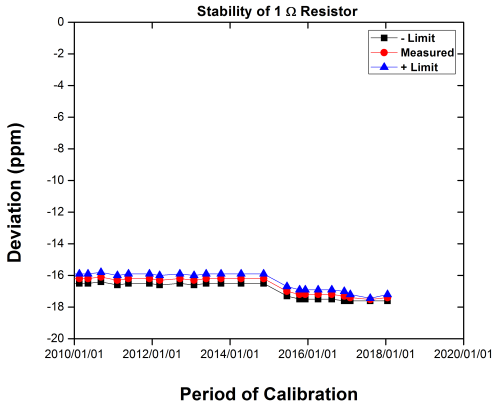

(a) Stability of 1 Ω

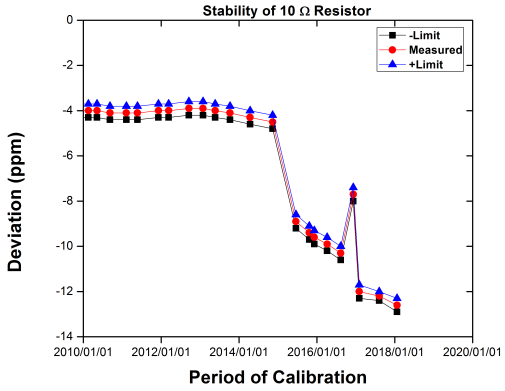

(b) Stability of 10 Ω

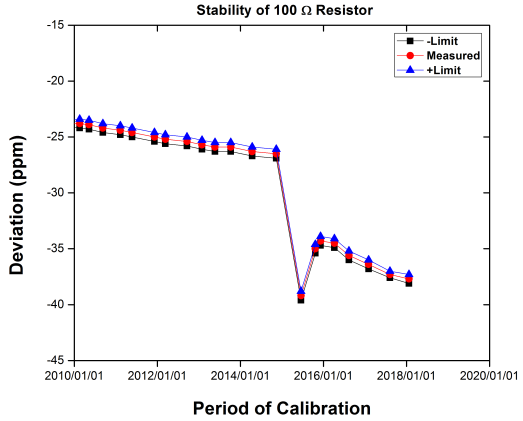

(c) Stability of 100 Ω

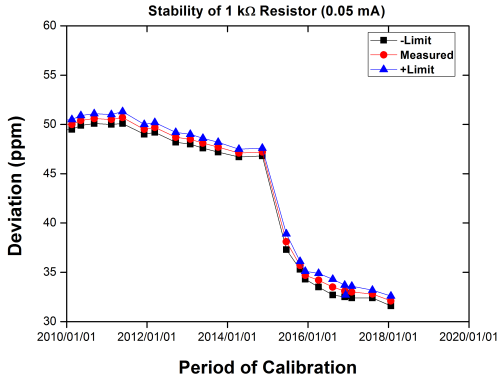

(d) Stability of 1 kΩ

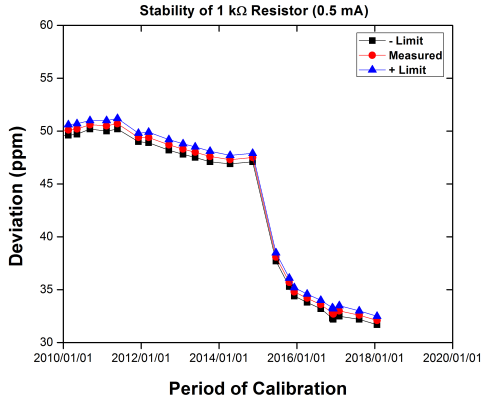

(e) Stability of 1 kΩ

Figure 6.5: Stability of (1 Ω - 1 kΩ), the red graphs represents the measured value of the standard resistor, while the blue and the black graphs represent the calculated deviation from the nominal value of the standard resistor.

deviation that is mentioned above. The drift rate is expected, since every standard resistor has its own drift rate per day. The drift rate before calibration is compensated for. Observing figure 6.6a to figure 6.7e a significant drift rate per day fluctuation is noticed. Note that it's not consistent with the established drift rate per day expectations. These drift rate per day fluctuation might be caused by fluctuations in the stability of the standard resistors.

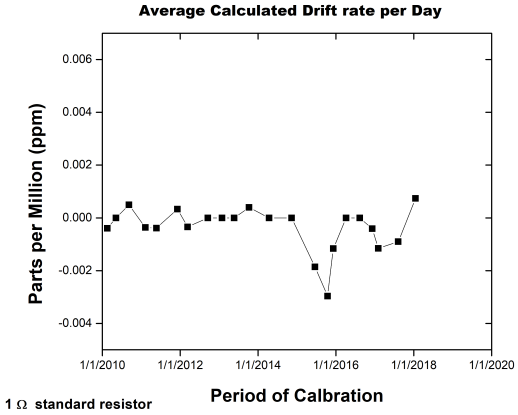

(a) Drift rate per day of 1 Ω

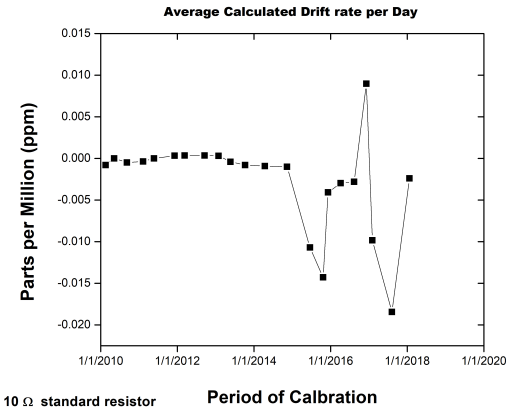

(b) Drift rate per day of 10 Ω

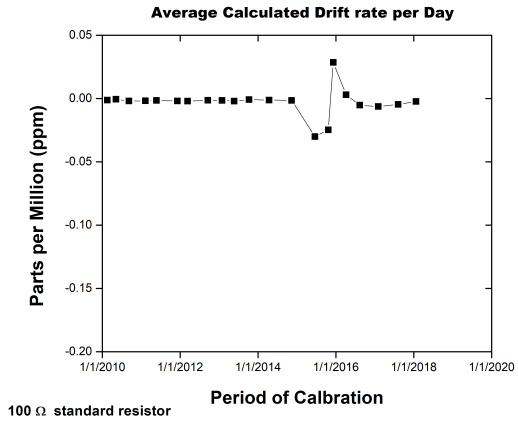

(c) Drift rate per day of 100 Ω

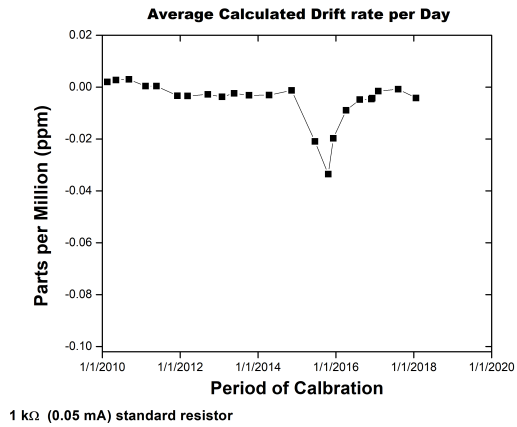

(d) Drift rate per day of 1 kΩ

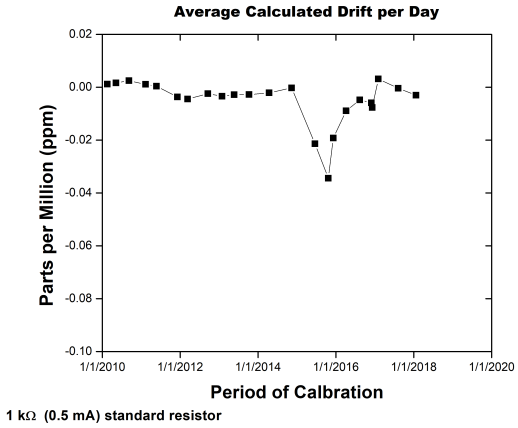

(e) Drift rate per day of 1 kΩ

Figure 6.7: Graphs from 6.7a to 6.7e showing average calculated drift rate per day for (1 Ω - 1 kΩ) standard resistors.

6.4.4 Determination of Temperature Coefficient

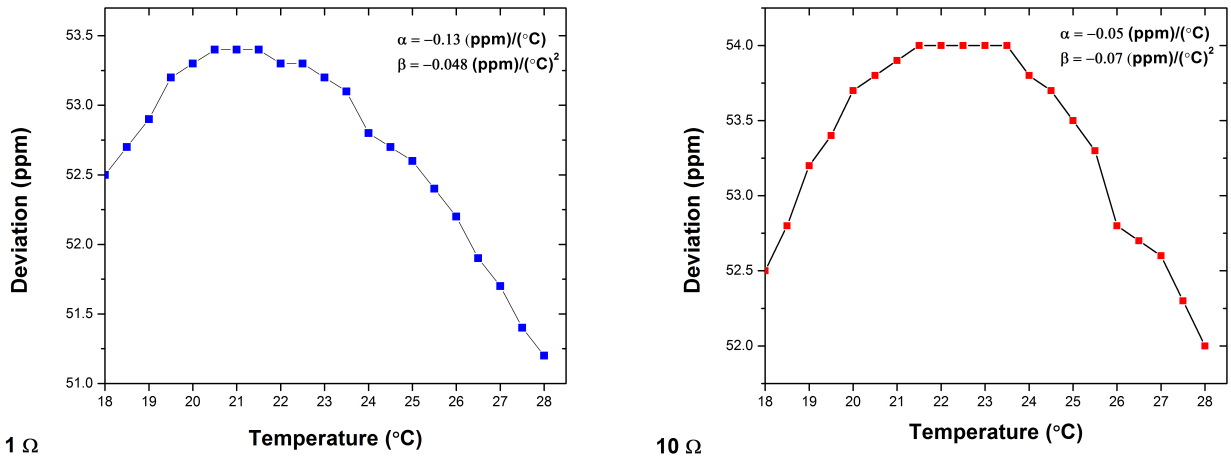

(a) Temperature Coefficient of 1 Ω

(b) Temperature Coefficient of 10 Ω

Figure 6.8: Graphs of resistance deviation value (in ppm) against temperature for a standard resistor of 1 Ω and 10 Ω resistance.

The temperature response of Fluke-742A series standard resistors is illustrated in both figure 6.8a (*for* 1 Ω) and 6.8b (*for* 10 Ω). The value of the first order is assigned to α and the second order to β respectively. The values obtained for 1 Ω standard resistor are 0.13 ppm /°C for α and -0.054 ppm /°C^2 for β, and for 10 Ω standard resistor -0.05 ppm /°C for α and -0.07 ppm /°C^2 for β. The resistance shows a trend of a pure metal by being directly proportional to temperature until 23 °C, above 23 °C the resistance values decreases. This confirms that our resistors have negative coefficients values. The results obtained illustrate that the 724A series standard resistors have small temperature coefficients of resistance. With the use of equation 6.3 with α and β values we can get the values of resistance at temperatures 18 °C to 28 °C.

7 | Chapter 7: Conclusion and Future Work

7.1 Research Summary and Conclusion

The focus of this thesis was the QHE, observed in a 2DEG. The CHE is a room temperature phenomenon observed by E.H Hall in 1879 where the resulting resistivity's ρ_{xx} and ρ_{xy} when plotted against magnetic field results in a linear trend shown in figure 7.1.

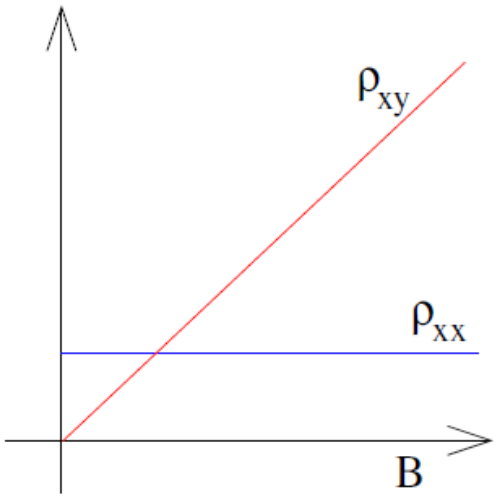

Figure 7.1: Classical Hall Effect curve illustrating the transverse (ρ_{xy}) and longitudinal (ρ_{xx}) resistivity's [74].

The QHE occurs at low temperatures under a strong perpendicular magnetic field. When the resulting ρ_{xx} and ρ_{xy} are plotted against magnetic field the resulting plot depicts the Hall plateaus (ρ_{xy}) and the SdH oscillations (ρ_{xx}) as seen in figure 5.1. This is led by the formation of the Landau levels which results from the behaviour of electrons under a strong magnetic field. In ideal material systems, the Landau levels are a series of δ-functions which are separated by $\hbar\omega_c$, while in real material systems there's disorder that cannot be prevented, this leads to Landau levels broadening into extended and localised states. We have seen that the energies of the Landau levels have the same trend as those of a linear harmonic oscillator given by equation 2.4. The localised states do not contribute to conduction and resistivity, resulting in the Hall voltage remaining constant. Hence the observation of the Hall plateaus over a range of magnetic field where the longitudinal resistance is zero.

The SdH oscillations were observed at low magnetic field. This requires that the thermal energy broadening and the scattering induced energy should be smaller than the energy separation of the Landau levels. Modulation doping was incorporated to minimise electron scattering. Two semiconductor materials were chosen to form a heterostructure, the important part for this is to consider their band gaps and lattice constants. This helps in minimising mismatch problems during sample growth. The material systems used to fabricate the semiconductor heterostructure were AlGaAs and GaAs. AlGaAs is grown on top of GaAs using MBE, which enables high-precision growth of atomic layers of the semiconductor substrate. Growth by MBE was chosen due to its fine ability to control over the electronic characteristics of the heterostructure wafer. For experimental observation of the QHE (meaning both Hall plateaus and SdH oscillations), low temperatures were required to suppress thermal excitations permitting electrons to escape the confining potentials. The cooling of the device was achieved by our dilution refrigerator that uses a ^{3}He/^{4}He mixture. Work was also carried out at NMISA in investigating the current resistor calibration methods, which have a direct traceability to the QHE.

A AlGaAs/GaAs Hall bar was studied over the course of this project. The transverse and longitudinal resistances were measured under a strong magnetic field up to 10 T. Characteristic features of the QHE (both Hall and SdH resistances) were observed in figure 5.1. The von Klitzing constant was calculated for different plateaus and multiplied by appropriate Landau index v as observed in figure 5.3 and we found that quantised resistance values agree with literature value within the expected uncertainty. The n_{2D} and μ was obtained from the SdH oscillations data. We compared the values obtained with other studies as seen in table 5.2. Our n_{2D} was high compared to those of reference [84] and [2], but this comes at the expense of having low μ.

7.2 Future Work

7.2.1 Cryogenic Current Comparator (CCC)

For the QHE implemented in AlGaAs to be used as a standard for electrical resistance, a CCC needs to be incorporated into the measurement system as is standard in metrology labs around the world where the QHR is operational. In future measurements the devices we studied should be measured in conjunction with a CCC.

A CCC is a device for comparing two electrical currents. CCC provides a very accurate way

of scaling the electrical units of current, voltage and resistance and has become an essential component of precision electrical metrology [80]. According to Sesé *et al.* a CCC is a three-superconducting winding transformer with two primaries and one secondary [69]. The idea of using a CCC for resistance ratio measurements was made by [80; 29] and national metrology institutes (NMIs). Different bridges are available such as commercial bridges based on the DCC and potentiometric bridges as discussed in chapter 6, but a CCC bridge coupled with a Superconducting Quantum Interference Device (SQUID) is preferred since it gives lowest measurement uncertainties [57], it outperforms DCC bridges by a few orders of magnitude. CCC's are used in highly precise comparative measurements of resistors or to measure extremely small currents of a few pico-amperes (pA).

A SQUID is a device that is utilised to detect a change in magnetic flux. Their design is a superconducting ring that is interrupted by one or more Josephson junctions [20]. The basic element of a SQUID is the Josephson junction. A RF SQUID contains one Josephson junction and a DC SQUID has two Josephson junctions, which is more sensitive than the counterpart. The ability of a SQUID sensor to measure the change in magnetic fields and current is based on four effects namely: Superconductivity, Meissner effect, flux quantisation, and Josephson Effect [68].

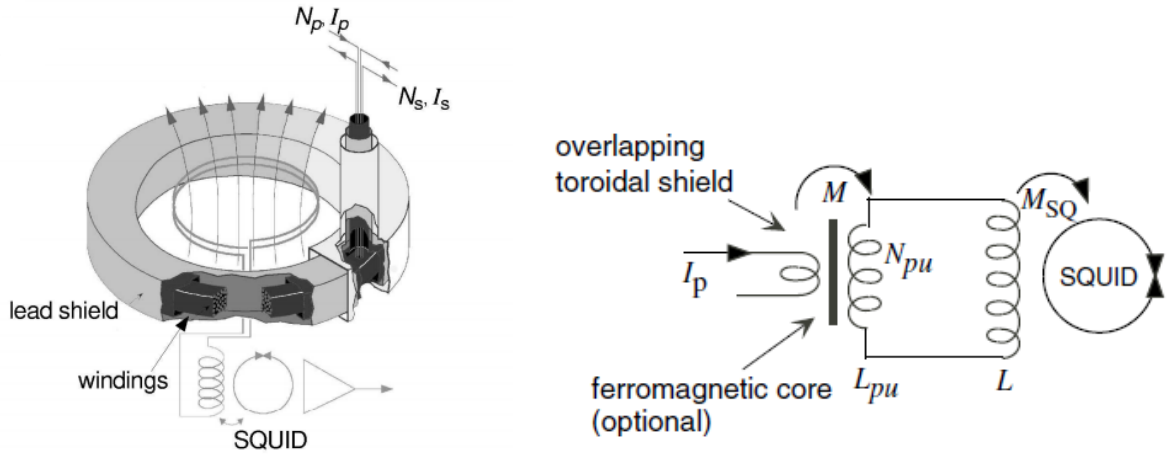

(a) CCC incorporated with a SQUID. **(b)** Circuit of a SQUID in a CCC.

Figure 7.2: A setup of a CCC configured with SQUID is illustrated and a SQUID circuit [33].

A CCC coupled with a SQUID is shown in figure 7.2a and a SQUID circuit in a CCC with N_{pu}, the number of turns, L_{pu} the inductance in a pick-up coil and L the inductance of

the input coil is illustrated in figure 7.2b [33]. The flux is detected by the SQUID through the pick-coil placed in the flux. The superconducting flux transformer incorporated with the SQUID to shield current flowing on the overlapping toroidal is depicted in figure 7.2b. Optimum current resolutions obtained when L_{pu} is equal to L [33]. A SQUID is used in other applications as a low noise current amplifier rather than a magnetic sensor [18]. The exact workings of a SQUID are beyond the scope of this thesis.

7.2.1.1 Basic principle of a CCC

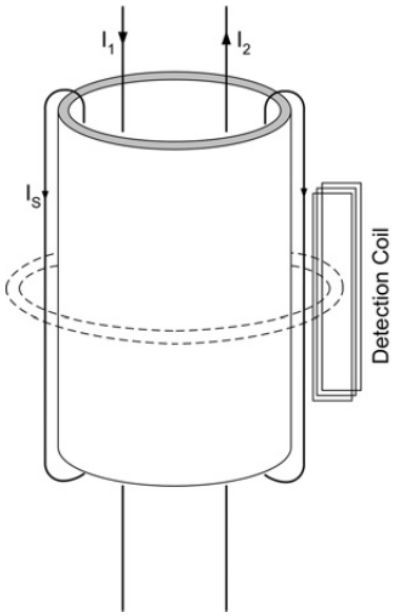

Figure 7.3: General principle of CCC [80].

A CCC makes use of the principle of superconductivity. Superconductivity was discovered by Heike Kamerlingh Onnes in 1911 when he was investigating the cooling of material at low temperatures three years after he liquefied helium. The disappearance of the electrical resistance below a critical temperature T_C is due to superconductivity and the expulsion of magnetic fields from the interior of a superconducting material is due to Meissner effect [23]. Before a CCC was developed to what it is today, it was constructed as depicted figure 7.3. A simple tube of a superconducting material surrounding two current-carrying wires (I_1 and I_2). A current through one of the wires results in an equal and opposite current on the inner surface of the tube. The current returns on itself via the external surface of the tube and one thus obtains the ideal condition wherein the same current flowing through different

windings generates identical fields outside the cable [80; 29]. The current distribution varies around the circumference of the tube, but Ampere's law prescribes that the sum of all the screening current (I_s) filaments plus I_1 and I_2 must be equal to zero, thus:

$$\oint \mathbf{B}d\mathbf{s} = \mu_0 \sum I_i, \tag{7.1}$$

$$\oint \mathbf{B}d\mathbf{s} = \mu_0 \sum (I_1 - I_2 + I_s). \tag{7.2}$$

Since $\boldsymbol{B} = 0$ and μ_0 the magnetic constant of a vacuum ($\mu_0 = 1$), we get the following equation:

$$I_s = I_1 - I_2. \tag{7.3}$$

Equation 7.3, results because of the Meissner effect. The position of the wires inside the tube influences the current distribution, while on the outside it is more uniform away from the ends of the tube. If zero flux is detected by a magnetic flux detector or a superconducting pickup coil as illustrated in figure 7.3, this implies that

$$I_1 = I_2. \tag{7.4}$$

The above design had problems with achieving high current ratios. The main design of the CCC had limitations. More wires were needed inside the tube to achieve integer current ratios higher than 10 : 1 [80]. A CCC was modified to overcome the limitations of not reaching high current ratios.

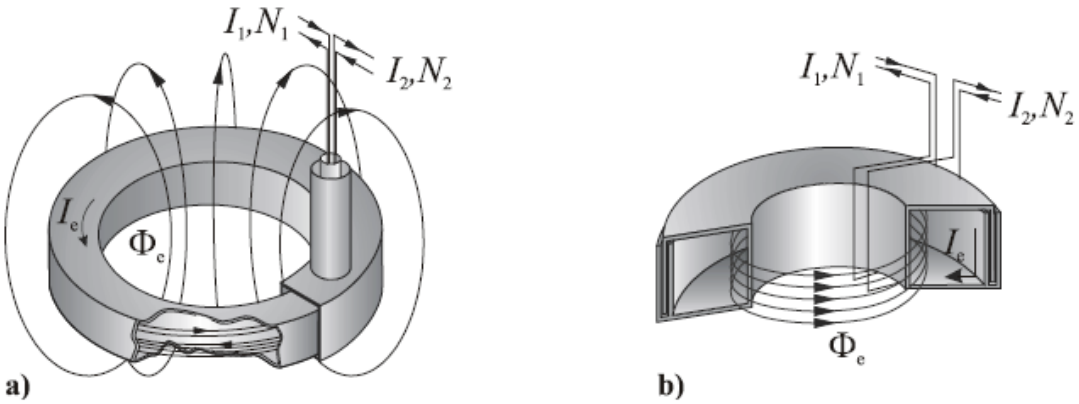

Figure 7.4: a). Type I CCC, b). Type II CCC (both from [59])

Two different approaches were designed to shield the sensing coil from direct coupling with the primary winding [69]. The first approach is known as type I [71], the superconducting shield is of the form of an overlapping tube with the current-carrying wires on the inside and the detector windings on the outside. The second approach is known as type II [25]. The superconducting shield is toroidal in shape with an overlapped gap region. The detector windings are on the inside, and the current-carrying windings are wound on the outside. A CCC uses the high magnetic flux sensitivity of a SQUID as a means of sensing and maintaining precise current ratios.

7.2.1.2 Resistance Bridges based on a CCC

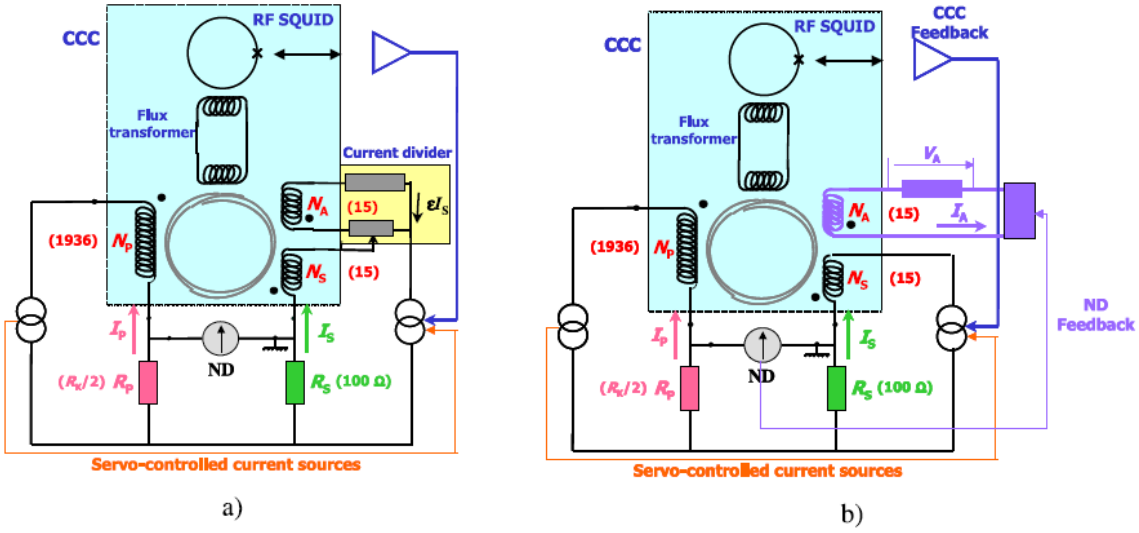

Figure 7.5: a). Resistance Bridge based on a CCC and a current divider. b). Resistance bridge based on a CCC, including an additional feedback between the auxiliary winding and the null detector [57].

Here we discuss the basic principle of resistance bridge based on a CCC. The bridges have two current sources which are an improvement from what was described by Delahaye [14]. The two resistors of resistances R_P and R_S to be compared, are both fed by the primary and secondary currents I_P and I_S from two servo-controlled current sources [21; 57], and the ratio of the two currents is chosen to be in a reciprocal ratio of the resistance values so that the voltage drop across the two resistors is the same [81] or less than 10^{-5} V [57]. The two currents I_P and I_S are also passed through the windings on a CCC with the number of

turns N_P and N_S, respectively, chosen to be in the same ratio as the resistors ratio so that the net flux in a CCC is zero. N_P and N_S are also chosen so that the ratios $\frac{N_P}{N_S}$ and $\frac{R_P}{R_S}$ are close within some few parts in 10^5 [57]. The bridge of figure 7.5(a) has a current divider with an auxiliary winding number of turns N_A which provides a fraction ε of the current I_S. The external feedback regulates the I_S so that screening current I_{CCC} is zero and ε is chosen so that the voltage measured by a null detector is zero. At balance, the primary to secondary resistor ratio is determined from the two equalities that describes the operation as given below.

$$R_P I_P = R_S I_S, \tag{7.5}$$

$$N_P I_P = N_S I_S + \varepsilon N_A I_S. \tag{7.6}$$

Combining these two equations results in a ratio of resistors in terms of the number of turns on a CCC and the ratio of the balancing auxiliary winding N_A of the winding N_S:

$$\frac{R_S}{R_P} = \frac{N_S}{N_P}(1 + \varepsilon \frac{N_A}{N_S}). \tag{7.7}$$

Such a resistance comparison bridge can calibrate a wire resistor with resistance R_S in terms of R_H with a relative uncertainty of 1 part in 10^9. Despite the complexity and the high cost of a CCC with a SQUID system, clear benefits for the metrology community are gained.

7.2.2 QHR utilising Graphene

In an attempt to reduce the cost of equipment and operational costs as well as reduce complexity. New graphene based systems are being explored that remove the need of a CCC for high accuracy measuremnts. Graphene is a 2DEG honeycomb lattice of carbon. For the last decade, graphene has attracted the attention of the metrology and low-dimensional physics community. Currently graphene is being explored as an alternative material/sample for QHR realisation via the QHE [53; 45; 34; 75]. Graphene has several advantages Quantum effects are observable at higher temperature and lower magnetic field of around 5 T. It was demonstrated by He *at el.* that graphene QHR systems can be achieved with accuracy under less demanding experimental conditions and with the advantage of using a cryogen-free system [30].

Graphene QHR systems can also be operated by using a Direct-Current-Comparator (DCC) resistance bridges with uncertainty a few parts in 10^{-8} [56]. All this leads to a simple operation of the QHR system. Another advantage of using graphene samples is that high current can be used to compare to the counterpart samples of GaAs. Lower noise for measurements and lower uncertainty are observed when using graphene samples [4]. Electrical standards based on the QHE have produced high accuracy but still no full benchtop system for metrology has been introduced[41].

Bibliography

[1] Ando, T. and Uemura, Y. (1974). Theory of quantum transport in a two-dimensional electron system under magnetic fields. i. characteristics of level broadening and transport under strong fields. *Journal of the Physical Society of Japan*, 36(4):959–967.

[2] Astley, M., Kataoka, M., Ford, C., Barnes, C., Anderson, D., Jones, G., Farrer, I., Ritchie, D., and Pepper, M. (2007). Energy-dependent tunneling from few-electron dynamic quantum dots. *Physical review letters*, 99(15):156802.

[3] Balkanski, M. and Yanchev, I. (2012). *Fabrication, Properties and Applications of Low-Dimensional Semiconductors*, volume 3. Springer Science & Business Media.

[4] Bergsten, T. and Eklund, G. (2016). Comparison between gaas and graphene qhr standards for resistance realisation at sp. In *Precision Electromagnetic Measurements (CPEM 2016), 2016 Conference on*, pages 1–2. IEEE.

[5] Blumenthal, M. D. (2007). *Gigahertz Quantised Charge Pumping*. PhD thesis, Wolfson College, Univeristy of Cambridge.

[6] Brown, D., Wachowicz, A., and Huang, S. (2010). AccuBridge™ towards the development of a DC Current Comparator resistance ratio standard. In *Precision Electromagnetic Measurements (CPEM), 2010 Conference on*, pages 639–640. IEEE.

[7] Cavendish Laboratory (2018). University of Cambridge, Department of Physics The Cavendish Laboratory mbe description. https://www.phy.cam.ac.uk/research/research-groups-images/sp/images/mbe1.png. Accessed: 2018-05-11.

[8] Chaudhry, G. and Brisson, J. (2009). Thermodynamic properties of liquid 3 he-4 he mixtures between 0.15 k and 1.8 k. *Journal of Low Temperature Physics*, 155(5-6):235–289.

[9] Chorley, S. J. (2007). *Electron Transport in Free-Standing Low-Dimensional Electron Systems*. PhD thesis, University of Cambridge.

[10] Chou, S., Antoniadis, D., and Smith, H. (1987). Application of the Shubnikov-de Haas oscillations in the characterization of Si MOSFET's and GaAs MODFET's. *IEEE Transactions on Electron Devices*, 34(4):883–889.

[11] Das, P., de Ouboter, R. B., and Taconis, K. (1965). A realization of a London-Clarke-Mendoza type refrigerator. In *Low Temperature Physics LT9*, pages 1253–1255. Springer.

[12] Davies John, H. (1998). *The physics of low-dimensional semiconductors: an introduction*. Cambridge University Press.

[13] De Wilde, Y., Gay, F., Piquemal, F. P., and Genevès, G. (2001). Measurements of single electron transistor devices combined with a CCC: progress report. *IEEE Transactions on Instrumentation and Measurement*, 50(2):231–234.

[14] Delahaye, F. (1978). A double constant current source for cryogenic current comparators and its applications. *IEEE Transactions on Instrumentation and Measurement*, 27(4):426–429.

[15] Delahaye, F., Bournaud, D., and Witt, T. (1992). Report on the 1990 international comparison of 1 Ω and 10 kΩ resistance standards at the BIPM. *Metrologia*, 29(4):273.

[16] Delahaye, F. and Jeckelmann, B. (2003). Revised technical guidelines for reliable dc measurements of the quantized Hall resistance. *Metrologia*, 40(5):217.

[17] Devreese, J. T. and Peeters, F. M. (2012). *The physics of the two-dimensional electron gas*, volume 157. Springer Science & Business Media.

[18] Drung, D., Abmann, C., Beyer, J., Kirste, A., Peters, M., Ruede, F., and Schurig, T. (2007). Highly sensitive and easy-to-use SQUID sensors. *IEEE Transactions on Applied Superconductivity*, 17(2):699–704.

[19] Epstein, M. (1967). Hall-effect devices. *IEEE Transactions on Magnetics*, 3(3):352–359.

[20] Fagaly, R. (2006). Superconducting quantum interference device instruments and applications. *Review of scientific instruments*, 77(10):101101.

[21] Gallop, J. and Piquemal, F. (2006). SQUIDs for standards and metrology. *The SQUID Handbook: Applications of SQUIDs and SQUID Systems, Volume II*, pages 95–137.

[22] Girvin, S. M. (2005). Introduction to the fractional quantum Hall effect. *PROGRESS IN MATHEMATICAL PHYSICS*, 45:133.

[23] Göbel, E. O. and Siegner, U. (2015). *Quantum Metrology: Foundation of Units and Measurements*. John Wiley & Sons.

[24] Grayson, M. and Fischer, F. (2005). Measuring carrier density in parallel conduction layers of quantum Hall systems. *Journal of applied physics*, 98(1):013709.

[25] Grohmann, K., Hahlbohm, H., Lubbig, H., and Ramin, H. (1974). Ironless cryogenic current comparators for ac and dc applications. *IEEE Transactions on Instrumentation and Measurement*, 23(4):261–263.

[26] Grubbs, W. (1959). Hall effect devices. *Bell Labs Technical Journal*, 38(3):853–876.

[27] Gust, J. (2000). Guide for Calibration Standard Resistors. ,.

[28] Haensch, T., Leschiutta, S., and Wallard, A. (2007). *Metrology and Fundamental Constants*, volume 166. IOS Press.

[29] Harvey, I. (1972). A precise low temperature dc ratio transformer. *Review of Scientific Instruments*, 43(11):1626–1629.

[30] He, H., Janssen, T., Rozhko, S., Tzalenchuk, A., Lara-Avila, S., Yakimova, R., and Kubatkin, S. (2016). Fabrication of graphene quantum hall resistance standard in a cryogen-table-top system. In *Precision Electromagnetic Measurements (CPEM 2016), 2016 Conference on*, pages 1–2. IEEE.

[31] Hogan, R. (2015). Expanded Uncertainty And Coverage Factors for Calculating Uncertainty by isobudgets.

[32] Jeanneret, B. and Benz, S. (2009). Application of the josephson effect in electrical metrology. *The European Physical Journal Special Topics*, 172(1):181–206.

[33] Jeckelmann, B. and Jeanneret, B. (2001). The quantum Hall effect as an electrical resistance standard. *Reports on Progress in Physics*, 64(12):1603.

[34] Jiang, Z., Zhang, Y., Tan, Y.-W., Stormer, H., and Kim, P. (2007). Quantum hall effect in graphene. *Solid state communications*, 143(1-2):14–19.

[35] Josephson, B. D. (1962). Possible new effects in superconductive tunnelling. *Physics letters*, 1(7):251–253.

[36] Kaneko, N.-H., Nakamura, S., and Okazaki, Y. (2016). A review of the quantum current standard. *Measurement Science and Technology*, 27(3):032001.

[37] Keller, M. W. (2000). Standards of current and capacitance based on single-electron tunneling devices. *Proc Fermi School CXL VI:"Recent Advances in Metrology and Fundamental Constants*.

[38] Khoza, M. (2015). *Calibration of Standard Resistors from* 0.001 Ω *to* 0.1 Ω. National Metrology Institute of South Africa.

[39] Kittel, P. (1990). Eddy current heating in magnetic refrigerators. In *Advances in Cryogenic Engineering*, pages 1141–1148. Springer.

[40] Klitzing, K. v., Dorda, G., and Pepper, M. (1980). New method for high-accuracy determination of the fine-structure constant based on quantized Hall resistance. *Physical Review Letters*, 45(6):494.

[41] Kruskopf, M. and Elmquist, R. E. (2018). Epitaxial graphene for quantum resistance metrology. *Metrologia*, pages R27–R36.

[42] Kumar, O. and Kaur, M. (2010). Single electron transistor: Applications & problems. *Int J VLSI Des Commun Syst (VLSICS)*, 1(4):24–29.

[43] Kuzmina, K. et al. (2013). Quantum Hall effect in 2 dimensional GaInAs structure. Master's thesis, Lappeenranta University of Technology, Lappeenranta.

[44] Kwok, D. (2011). The Quantum Hall Effect in Graphenea physicist's mishaps in beijing, researching graphene-based nanoelectronics, amongst other things. https://physicsresearchinbeijing.wordpress.com/2011/07/18/the-quantum-hall-effect-in-graphene/. Accessed: 2018-05-11.

[45] Lafont, F., Ribeiro-Palau, R., Kazazis, D., Michon, A., Couturaud, O., Consejo, C., Chassagne, T., Zielinski, M., Portail, M., Jouault, B., et al. (2015). Quantum hall resistance standards from graphene grown by chemical vapour deposition on silicon carbide. *Nature communications*, 6:6806.

[46] Landwehr, G. (2003). 25 Years quantum Hall effect: how it all came about. *Physica E: Low-dimensional systems and Nanostructures*, 20(1):1–13.

[47] LEDERER, P. and GOERBIG, M. O. (2006). Introduction to the Quantum Hall Effects. *Lecture notes*.

[48] Leiden Cryogenics BV (2017). Leiden Cryogenics BV: Leader in Low Temperature Techniques, croygen-free models. https://www.leiden-cryogenics.com/images/LC-Floder-2017.pdf. Accessed: 2018-05-20.

[49] Markus, M. (1992). CRITERIA FOR LABORATORY ACCREDITATION IN THE FIELD OF ELECTRICAL DCLF METROLOGY. http://www.sanas.co.za/manuals/pdfs/TR%2011-02.pdf?manualsOrder=Sorter_doc_category&manualsDir=ASC&manualsPage=2. Accessed: 2018-11-23.

[50] Matlejoane, A. (2015). *Calibration of Standard Resistors from* 1 Ω *to* 10 kΩ. National Metrology Institute of South Africa.

[51] National Institute of Science and Technology (2017). Ampere: The Future. https://www.google.com/search?q=single+electron+transport+devices&rlz=1C1GGRV_enZA751ZA751&source=lnms&tbm=isch&sa=X&ved=0ahUKEwjbisyW6r7fAhU7SRUIHRqWAYMQ_AUIDigB&biw=1366&bih=664#imgrc=m5JnZyBscb-sJM:. Accessed: 2018-08-30.

[52] Nawrocki, W. (2007). *Introduction to Quantum Metrology*. Springer.

[53] Novoselov, K. S., Jiang, Z., Zhang, Y., Morozov, S., Stormer, H. L., Zeitler, U., Maan, J., Boebinger, G., Kim, P., and Geim, A. K. (2007). Room-temperature quantum hall effect in graphene. *Science*, 315(5817):1379–1379.

[54] of South Africa, R. (2007). Measurement Units and Measurement Standards Act No. 16 2006. https://www.gov.za/sites/default/files/a18-06_0.pdf. Accessed: 2018-11-17.

[55] Owens, A. and Peacock, A. (2004). Compound semiconductor radiation detectors. *Nuclear Instruments and Methods in Physics Research Section A: Accelerators, Spectrometers, Detectors and Associated Equipment*, 531(1):18–37.

[56] Panna, A. R., Kraft, M. E., Rigosi, A. F., Jones, G. R., Payagala, S. U., Kruskopf, M., Jarrett, D. G., and Elmquist, R. E. (2018). Uncertainty of the ohm using cryogenic and non-cryogenic bridges. In *2018 Conference on Precision Electromagnetic Measurements (CPEM 2018)*, pages 1–2. IEEE.

[57] Poirier, W., Schopfer, F., Guignard, J., Thévenot, O., and Gournay, P. (2011). Application of the quantum Hall effect to resistance metrology. *Comptes rendus physique*, 12(4):347–368.

[58] Popovic, R. (1991). Hall Effect Devices, ser. *The Adam Hilger Series on Sensors. Bristol: lOP Pub lishing Ltd.*

[59] Porcar, B. and Elena, M. (2002). *Cryogenic current comparators with optimum SQUID readout for current and resistance quantum metrology.* University of Twente.

[60] Qiu, G., Wang, Y., Nie, Y., Zheng, Y., Cho, K., Wu, W., and Ye, P. D. (2018). Quantum Transport and Band Structure Evolution under High Magnetic Field in Few-Layer Tellurene. *arXiv preprint arXiv:1806.08229.*

[61] Razeghi, M. (1995). *The MOCVD Challenge: Volume 2: A Survey of GaInAsP-GaAs for photonic and electronic device applications*, volume 2. CRC Press.

[62] Roccaforte, F., La Via, F., and Raineri, V. (2005). Ohmic contacts to sic. *International journal of high speed electronics and systems*, 15(04):781–820.

[63] Saku, T., Hirayama, Y., and Horikoshi, Y. (1991). High electron mobility in AlGaAs/GaAs modulation-doped structures. *Japanese journal of applied physics*, 30(5R):902.

[64] Scherf, A. (2017). Quantum Hall Measurements on a GaAs/AlGaAs Heterostructure. unpublished thesis.

[65] Schleijpen, H. M. A. (1987). *The Shubnikov de Haas effect in narrow-gap semimagnetic semiconductors.* PhD thesis, Technische Universiteit Eindhoven.

[66] Schubnikow, L. and De Haas, W. (1930). A new phenomenon in the change of resistance in a magnetic field of single crystals of bismuth. *Nature*, 126(3179):500.

[67] Schurr, J. (2016). AC and DC quantum Hall resistance-simple and beautiful. *IEEE Instrumentation & Measurement Magazine*, 19(1):24–26.

[68] Seidel, P. (2015). *Applied Superconductivity: Handbook on Devices and Applications.* John Wiley & Sons.

[69] Sesé, J., Camón, A., Rillo, C., and Rietveld, G. (1999). Ultimate current resolution of a cryogenic current comparator. *IEEE Transactions on Instrumentation and Measurement*, 48(6):1306–1313.

[70] Shapiro, S. (1963). Josephson currents in superconducting tunneling: The effect of microwaves and other observations. *Physical Review Letters*, 11(2):80.

[71] Sullivan, D. and Dziuba, R. F. (1974). A low-temperature direct-current comparator bridge. *IEEE Transactions on Instrumentation and Measurement*, 23(4):256–260.

[72] Taylor, B. and Witt, T. (1989). New international electrical reference standards based on the Josephson and quantum Hall effects. *Metrologia*, 26(1):47.

[73] Thangaraj, M. P. S. (2008). *Transport measurements in Two Dimensional Electron-Hole Bilayer Devices*. PhD thesis, Wolfson College, Univeristy of Cambridge.

[74] Tong, D. (2016). Lectures on the quantum Hall effect. *arXiv preprint arXiv:1606.06687*.

[75] Tzalenchuk, A., Lara-Avila, S., Kalaboukhov, A., Paolillo, S., Syväjärvi, M., Yakimova, R., Kazakova, O., Janssen, T., Fal'Ko, V., and Kubatkin, S. (2010). Towards a quantum resistance standard based on epitaxial graphene. *Nature nanotechnology*, 5(3):186–189.

[76] Uhlig, K. (2008). Dry dilution refrigerator with high cooling power. In *AIP Conference Proceedings*, volume 985, pages 1287–1291. AIP.

[77] Vaid, D. (2012). Quantum hall effect and black hole entropy in loop quantum gravity. *arXiv preprint arXiv:1208.3335*.

[78] Von Klitzing, K. (2005). 25 Years of quantum Hall effect QHE a personal view on the discovery, physics and applications of this quantum effect. In *The Quantum Hall Effect*, pages 1–21. Springer.

[79] Wang, L. and O'Connell, R. (1989). Ideal Two-Dimensional Electron Gas in a Magnetic Field and at Non-Zero Temperatures. An Alternative Approach. *physica status solidi (b)*, 153(1):343–359.

[80] Williams, J. (2011). Cryogenic current comparators and their application to electrical metrology. *IET science, measurement & technology*, 5(6):211–224.

[81] Williams, J., Janssen, T., Rietveld, G., and Houtzager, E. (2010). An automated cryogenic current comparator resistance ratio bridge for routine resistance measurements. *Metrologia*, 47(3):167.

[82] Wolfson, R. (1991). The lock-in amplifier: A student experiment. *American Journal of Physics*, 59(6):569–572.

[83] Wolski, S. P. (2017). mK-scale Cooling and the Quantum Hall Effect. unpublished thesis.

[84] Wright, S., Blumenthal, M., Gumbs, G., Thorn, A., Pepper, M., Janssen, T., Holmes, S., Anderson, D., Jones, G., Nicoll, C., et al. (2008). Enhanced current quantization in high-frequency electron pumps in a perpendicular magnetic field. *Physical Review B*, 78(23):233311–4.

[85] Wysokinski, K. I. (2000). Integer and fractional quantum Hall effects. *European Journal of Physics*, 21(6):535.

[86] Yamahata, G., Giblin, S. P., Kataoka, M., Karasawa, T., and Fujiwara, A. (2017). High-accuracy current generation in the nanoampere regime from a silicon single-trap electron pump. *Scientific Reports*, 7:45137.

[87] Zurich Instruments (2016). Principles of lock-in detection and state of the art. white paper zurich instruments. https://www.zhinst.com/sites/default/files/li_primer/zi_whitepaper_principle_of_lock-in_detection.pdf. Accessed: 2018-05-22.

Appendix A

Since the EG & G7220 lock-in amplifier is equipped with an efficient internal signal generator, then it was used for setting the reference frequency and providing the source-drain bias to our device during measurements. 77 Hz was the reference frequency chosen, because it was enough to eliminate more noise associated with our experimental setup.

Lock-in amplifiers settings:

Parameter	**SR830**	**EG&G7770**
Reference source	external	internal
Reference frequency	-	77.000 Hz
Reference amplitude	-	1.000 V RMS
Source	A-B	A
Time constant	300 ms	200 ms
Sensitivity	1 mV	10 mV
Reserve	low noise	low nioise
Filter dB/oct.	24 dB	24 dB
Grounding	float	float
Coupling	AC	AC

Current pre-amplifier settings:

Parameter	**SR570**
Sensitivity	1 μA/V
Gain mode	low noise
Filter	off
Input offset	off
Bias voltage	off

Appendix B

3 Calibration Software and Undertaking a Measurement

After clicking the icon of MI 6010C software on the taskbar, the interface below will be displayed, we can observe the measurement System Setting Files, Resistor ID Files, and the Program Files Selection Menu.

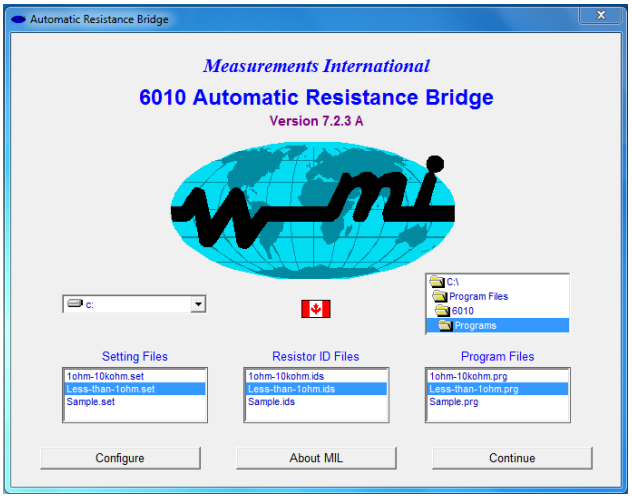

Figure 7.6: MI 6010C Opening Menu Screen

The preview of all the software's of the resistance measurement systems is the same they only differ by version. Let's say we are on to calibrate a UUT of less than 1 Ω with a reference standard resistor of 1 Ω. The details for setting the program for calibration are given as follows. We select "Less than 1 ohm" from the Setting Files field, select "Less than 1 ohm transfer.ids" from the Resistor ID Files field and select "Less than 1 ohm transfer.prg" from the Program Files field. We are permitted to click "Continue" and the following main menu screen below will be displayed:

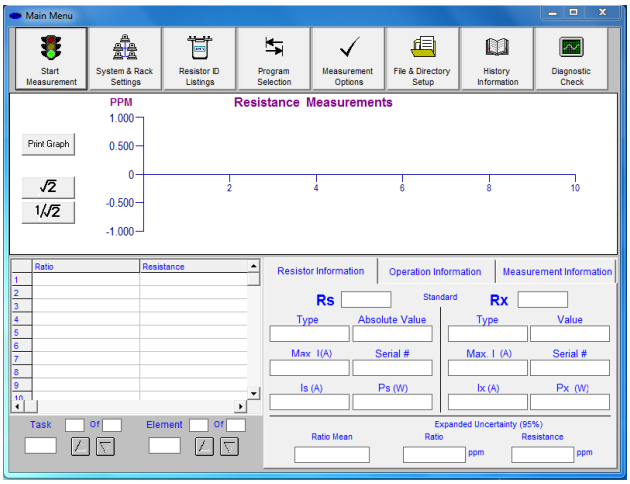

Figure 7.7: MI 6010C Main Menu Screen

Select "Systems and Rack Settings" from the main menu to display the following Systems and Rack Settings screen:

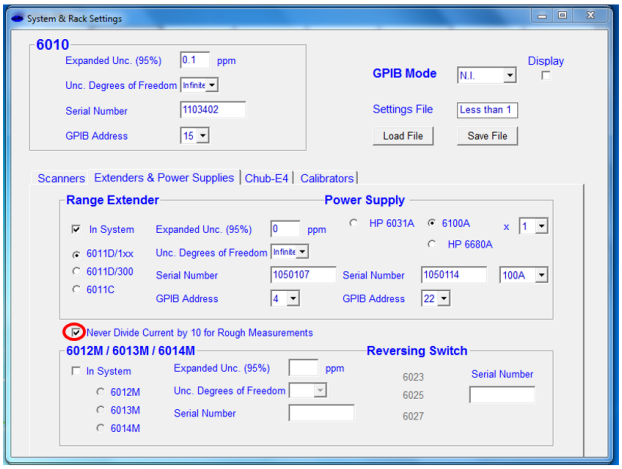

Figure 7.8: MI 6010C Systems and Rack Settings Screen

Select "Extenders and Power Supplies" and check the "Never Divide Current by 10 for Rough Measurements" as circled, when measuring 1000:1 ratio. For 10:1 and 100:1 ratios uncheck the box. Return to the main menu by closing the "Extenders and Power Supplies", then select "Resistor ID Listings" from the main menu to display the following Resistance ID Listing screen below.

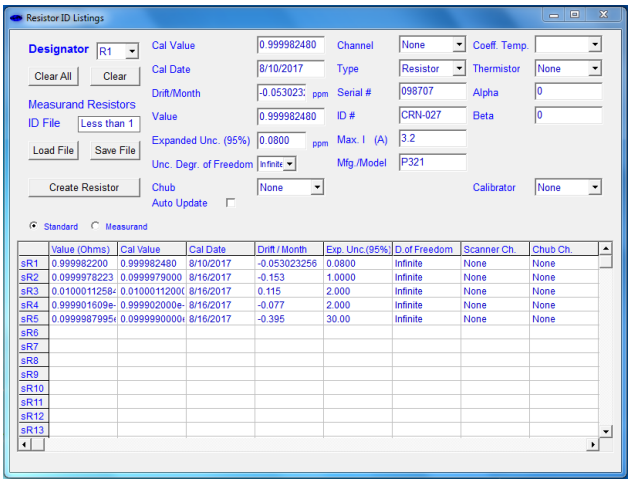

Figure 7.9: MI 6010C Resistor ID "Standard" Listings Screen

The operator is permitted to switch between "Standard" and "Measurand" by highlighting the required option. Switch to "Standard" field by selecting "Standard" on the Resistance ID Listing menu screen. Update reference standard resistor information fields including the latest calibration data and select "Create Resistor". Select the "Measurand" to display the following window:

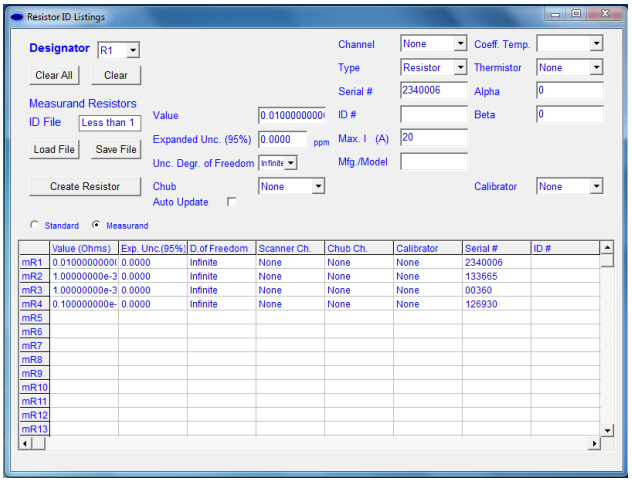

Figure 7.10: MI 6010C Resistor ID "Measurand" Listings Screen

Update UUT information fields and select "Create Resistor". Save the updated "Less than 1 ohm as a transfer.ids" file. Return to the main menu by closing the Resistance ID Listing menu screen. Select "Program Selection" from the main menu screen. To display the following "Program Selection and Creation" screen.

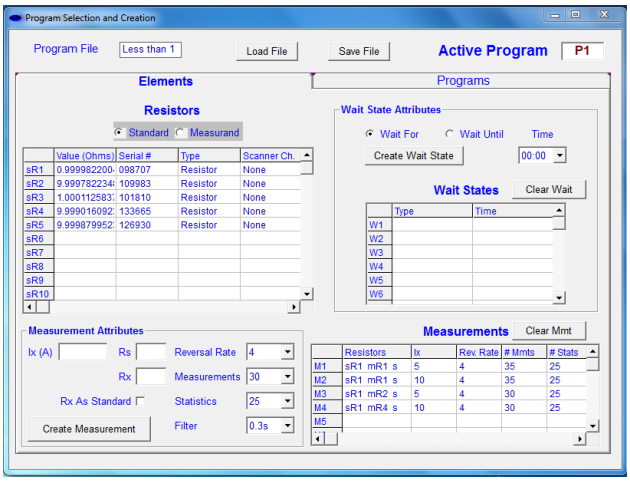

Figure 7.11: MI 6010C Creating and Editing a Measurement Program Screen

The operator can switch between "Standard" and "Measurand" by highlighting the required option. Select the "Elements" tab to display Elements window.

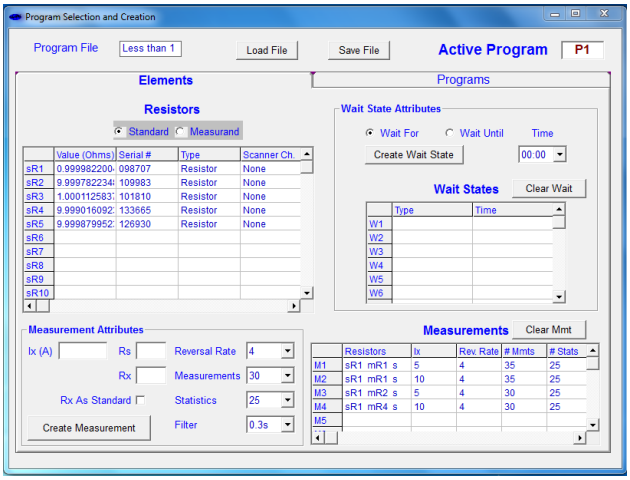

Figure 7.12: MI 6010C Elements Tab showing "Standard" Screen

Select "Standard" to display reference standard resistor listings above. Select and drag the required standard e.g. "sR1" to "Rs" Measurement Attributes box. Select "Measurand" tab to display UUT listings.

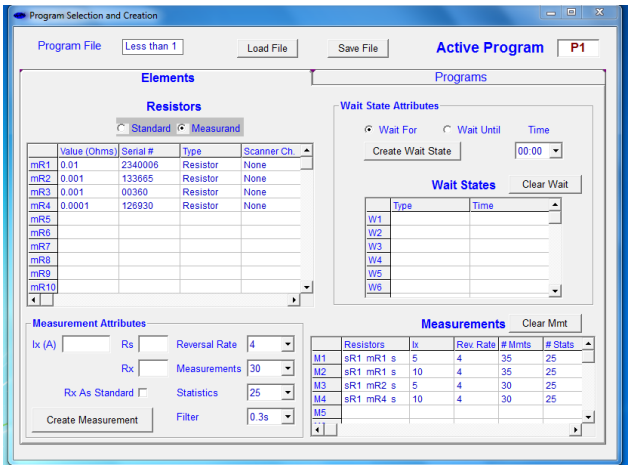

Figure 7.13: MI 6010C Elements Tab "Measurand" Screen

Select and drag the required UUT e.g. "mR1" to "Rx" Measurement Attributes box. Enter a required test current value in the in the "Ix" Measurement Attributes box. Enter the number of measurement reversals, maximum number of measurements and the number of measurements used to calculate the average measured value. Select "Measurements Attributes" destination e.g. "M1" in the "Measurements field". Select "Create Measurement" tab to create a measurement. Enter a required waiting time and select "Create Wait State" tab to create a waiting period before the start of measurements. The "wait for" states will delay the task for a specified amount of time, while the "wait until" states will delay until the system clock reaches the selected time. Select the "Programs" tab to display the "Program" window below:

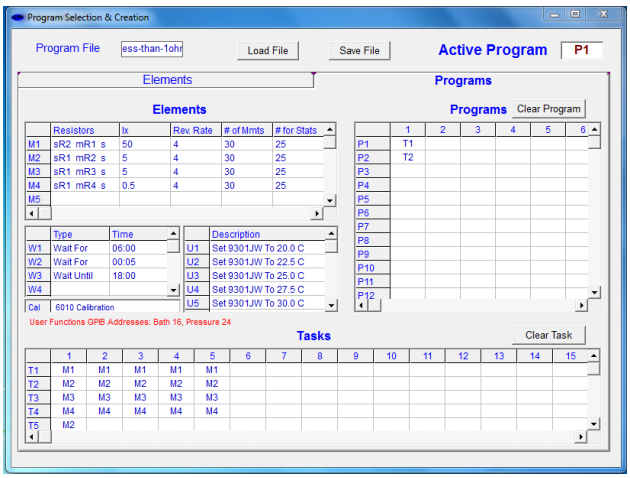

Figure 7.14: MI 6010C Creating Tasks and Programs Screen

Select and drag "Element" e.g. "M1" to destination "Task" e.g. "T1". Select and drag

"Task" e.g. "T1" to destination "Program" e.g. "P1" Save the updated "Less than 1 ohm transfer.prg" file. Return to the main menu by closing the "Program Creation and Selection" screen. Select "Measurement Options" from the main menu screen to display the following "Measurement Options" screen below:

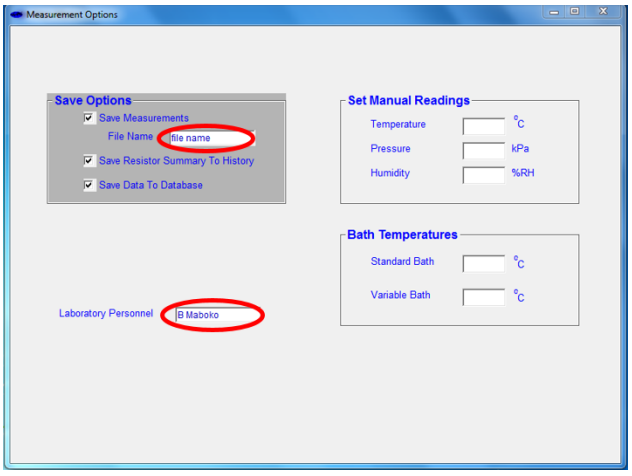

Figure 7.15: MI 6010C Measurement Options Screen

Select the "Save Measurements" box to save the results in a "*.mea" file. Type in the filename WITHOUT an extension (extension is already set to ".mea"). Enter the details of the metrologist and environmental conditions to be included in the measurement data file. Return to the main menu by closing the "Measurement Option" screen. Select "Diagnostic Check" from the main menu to open the following "6010 Calibration" window below:

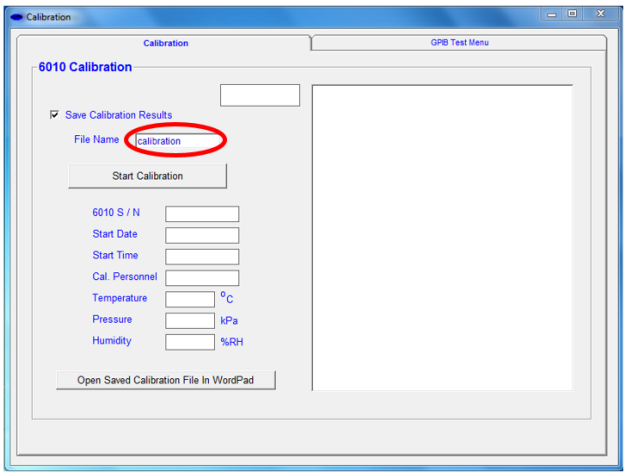

Figure 7.16: MI 6010C "Calibration Window" Screen

Enter a file name for the calibration results. Select "Save Calibration Results", then select

"Start Calibration" to start the self-calibration routine of the 6010C system. After the system self-calibration is completed, close the calibration screen to return to the main menu. Select "Program Selection" from the main menu screen. To display the following "Program Selection and Creation" screen below:

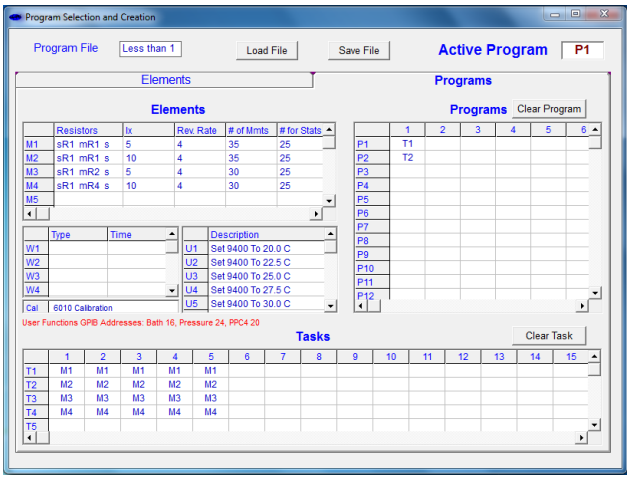

Figure 7.17: MI 6010C Programs Window to select "Active Program" Screen

Select the "Programs" tab. Double click on the program for required measurement to display it in the active program field. Close the "Program Creation and Selection" screen to return to the main menu. Select "Start Measurement" to run a selected measurement program. The system stops automatically at the end of the measurement. The measurement results are stored in the respective "*.meas" file.

4 Results and Analysis

To load a required calibration file onto an excel spreadsheet: double click "MI 6010 Output Macro" short-cut on the desktop. Select "Load Measurement Report" to display window below:

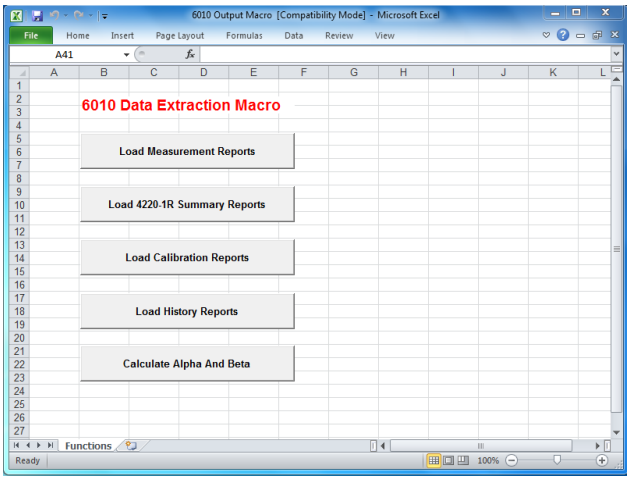

Figure 7.18: MI 6010C Data Extraction Macro Screen.

After select and open a required "mea" file, we are permitted to choose between the two "mea" files.

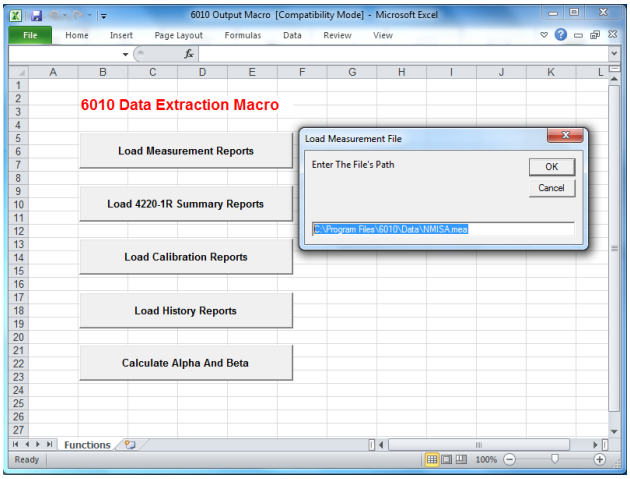

Figure 7.19: MI 6010 Data Extraction Macro showing the highlighted path in "blue" to load the results

Then following window will display below. Remove unwanted information from the spreadsheet.

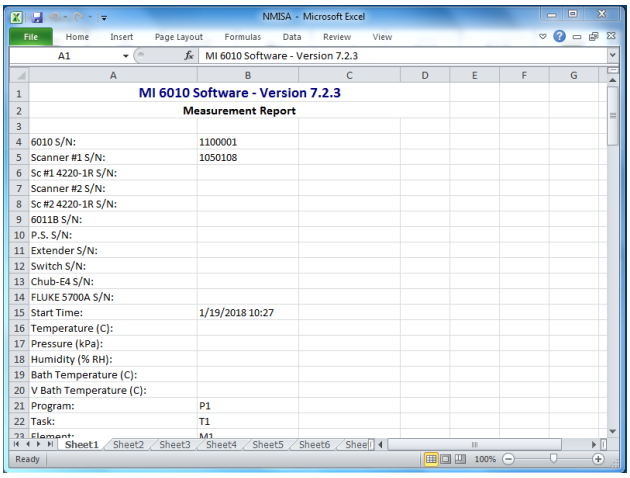

Figure 7.20: MI 6010 Measurement Report with information for Standard Resistor and the UUT.

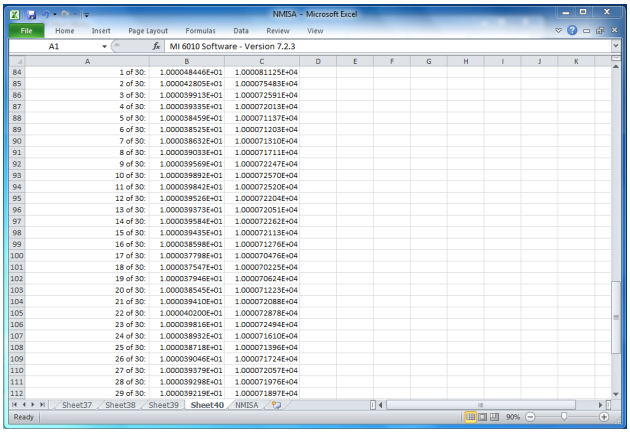

Figure 7.21: Screenshot of the results

From the results, Calculate the average for each measurement set and calculate the average of the five averages, standard deviation, and Experimental Standard Deviation of the Mean (ESDM). Convert the ESDM to ppm, then import the ESDM (ppm) into the Uncertainty budget spreadsheet template found on: (https://intranet.nmisa.org). The measurement results are then reported on a master certificate template titled "MC – 0008 – 0,001 Ohm to 0,1 Ohm 6010C – 6011B – 6100A system.doc" found on I:\laboratories\dc low frequency\reporting of results\master certificates or (https://intranet.nmisa.org).

5 Uncertainty Estimation

After the results have been to be processed they are imported in an uncertainty budget matrix (UBM) template in a spreadsheet. All these uncertainties discussed below were

taken into consideration when the UBM was created, the advantage of the UBM template is an automatic incorporation of all uncertainties during results analysis. The following sources of uncertainty are common in all the three measurement systems mentioned above:

0.1 Calibration of reference standard resistor:

- This uncertainty component is obtained from the calibration certificate of the reference standard resistor. This component is assigned a normal distribution and therefore divided by 2.

0.2 Drift of reference standard resistor:

- This uncertainty component is obtained from the control chart of the reference standard resistor. It is assigned a rectangular distribution and therefore divided by $\sqrt{3}$.

0.3 Temperature coefficient of standard resistor:

- The reference standards used to import traceability from the BIPM are calibrated at 23 °C and are kept in an oil bath that is controlled at 23 °C with all other reference standards. Uncertainty contribution by this component is negligible and is therefore ignored.

0.4 Power coefficient of reference standard resistor:

- The reference standards are used at the same nominal current to which they were calibrated. Uncertainty contribution by this component is negligible and therefore ignored.

0.5 Accuracy specifications of the 6010C Automatic Resistance Bridge:

- Manufacturer specifies a 95 % confidence level. It is assigned a normal distribution and therefore divided by 2.

0.6 Resolution of the 6010C Automatic Resistance Bridge:

- Manufacturer specifies a 95 % confidence level. It is assigned a normal distribution and therefore divided by 2.

0.7 Linearity of the 6010C Automatic Resistance Bridge:

- Manufacturer specifies a 95 % confidence level. It is assigned a normal distribution and therefore divided by 2.

0.8 6010C Automatic Resistance Bridge Ratio Error:

- This uncertainty component was determined experimentally by interchanging STD and UUT and comparing the difference between the two ratios. It is assigned a normal distribution and therefore divided by 1.

0.9 ESDM of the reported average result:

- The reported value is a calculated average of five sets of measurement results. The standard deviation of the reported average is therefore divided by $\sqrt{5}$.

The difference sources of uncertainty for the ($0.001\,\Omega$ to $0.1\,\Omega$) are extended to the following:

0.10 Accuracy specifications of the 6011B Range Extender:

- This uncertainty component is obtained from the manufacturer specifications. It is assigned a rectangular distribution and therefore divided by $\sqrt{3}$.

0.11 Linearity of the 6011B Range Extender:

- This uncertainty component is obtained from the manufacturer specifications. It is assigned a rectangular distribution and therefore divided by $\sqrt{3}$.

The difference sources of uncertainty for the ($10\,\mathrm{k}\Omega$ to $1\,\mathrm{G}\Omega$) are extended to the following:

0.12 Temperature coefficient of Reference Standard Resistor:

- The specifications for the $10\,\mathrm{k}\Omega$ are not available while for the $100\,\mathrm{k}\Omega$ to $10\,\mathrm{M}\Omega$ are available in [7] and for the $100\,\mathrm{M}\Omega$ in [8]. The uncertainty components are quantified as follows:

- USSR P321 10 k: This standard is kept in an oil bath that is temperature controlled. This standard is calibrated and used at the set oil bath temperature. The temperature variation of the oil bath is negligible and therefore the uncertainty contribution by temperature coefficient is negligible and therefore ignored.

- Fluke 742A - 100 k: The maximum error from a calibration value due to temperature coefficient for a 5 °C temperature variation is 2 ppm. Then for a worst case laboratory temperature variation of 2 °C is 0.8 ppm. It is assigned a rectangular distribution and therefore divided by $\sqrt{3}$.

- Fluke 742A - 1 M: The maximum error from a calibration value due to temperature coefficient for a 5 °C temperature variation is 2 ppm. Then for a worst case laboratory temperature variation of 2 °C is 0.8 ppm. It is assigned a rectangular distribution and therefore divided by $\sqrt{3}$.

- Fluke 742A - 10 M: The maximum error from a calibration value due to temperature coefficient for a 5 °C temperature variation is 2 ppm. Then for a worst case laboratory temperature variation of 2 °C is 1.2 ppm. It is assigned a rectangular distribution and therefore divided by $\sqrt{3}$.

- Guildline 9336 100 M: The resistor temperature coefficient at between 18 °C and 28 °C is < 5 ppm /°C. A worst case value of 10 ppm quantified for a worst case laboratory temperature variation of 2 °C. It is assigned a rectangular distribution and therefore divided by $\sqrt{3}$

0.13 Voltage coefficient of the Reference Standard Resistors:

- The specifications for the 10 kΩ are not available while for the 100 kΩ to 10 MΩ are available in [7] and for the 100 MΩ in [8]. The uncertainty components are quantified as follows:

- Fluke 742A - 10 k: This standard can handle a maximum test current of 3.2 mA. It is calibrated at a test current of 0.05 mA and used at test current of 0.09 mA. This means the resistor is operated at 1,6 % and 2,8 % of its power rating. The uncertainty contribution due to power coefficient will be negligible and therefore ignored.

- Fluke 742A - 100 k: This standard is calibrated with a nominal 9 V applied across it and used to calibrate a 1 MΩ standard with a nominal 9 V applied across it and

therefore the uncertainty contribution by voltage coefficient is negligible and therefore ignored.

- Fluke 742A - 1 M: This standard is calibrated with a nominal 91 V applied across it and used to calibrate a 10 MΩ standard with a nominal 9 V applied across it. This results in a nominal voltage difference of 82 V and therefore a nominal current difference of 82 µA. The error introduced by a current difference of 100 mA is 1 ppm and therefore the error introduced by a current difference of 82 µA will be 0.82 ppm. It is assigned a rectangular distribution and therefore divided by $\sqrt{3}$.

- Fluke 742A - 10 M: This standard is calibrated with a nominal 91 V applied across it and used to calibrate a 100 MΩ standard with a nominal 9 V applied across it. This results in a nominal voltage difference of 82 V and therefore a nominal current difference of 8.2 µA. The error introduced by a current difference of 200 µA is 1 ppm and therefore the error introduced by a current difference of 8.2 µA will be 0.41 ppm. It is assigned a rectangular distribution and therefore divided by $\sqrt{3}$.

- Guildline 9336 - 100 M: This standard is calibrated with a nominal 91 V applied across it and used to calibrate a 1 GΩ standard with a nominal 9 V applied across it. This results in a nominal voltage difference of 82 V. The resistor voltage coefficient is 0.5 ppm /V and therefore a worst case value of 41 ppm is quantified. It is assigned a rectangular distribution and therefore divided by $\sqrt{3}$.

- Guildline 9336 - 1 G: This standard is calibrated with a nominal 91 V applied across it and used to calibrate a 1 GΩ standard with a nominal 9 V applied across it. This results in a nominal voltage difference of 82 V. The resistor voltage coefficient is 0.5 ppm /V and therefore a worst case value of 41 ppm is quantified. It is assigned a rectangular distribution and therefore divided by $\sqrt{3}$.

0.14 Short term drift of the 6000B Automatic High Resistance Ratio Bridge:

- This uncertainty component is obtained from the manufacturer specifications. It is assigned a rectangular distribution at 95 % confidence level and therefore divided by 2.

0.15 System leakage resistance error:

- A method for determining this uncertainty component is still being investigated. At this point in time an assumed value is used in the uncertainty calculation. It is assigned a rectangular distribution and therefore divided by $\sqrt{3}$.

0.16 Error due to detector input impedance:

- The 3458A used has minimum input impedance of 10 GΩ the measurement range. The effect of the input impedance is calculated and is assigned a rectangular distribution and therefore divided by $\sqrt{3}$.

0.17 Insulation resistance error of the 4420A scanner:

- This uncertainty component is obtained from the manufacturer specifications. It is assigned a rectangular distribution at 95 % confidence level and therefore divided by 2.

0.18 Contact resistance error of the 4420A scanner:

- This uncertainty component is obtained from the manufacturer specifications. It is assigned a rectangular distribution at 95 % confidence level and therefore divided by 2.

Appendix C

ANNEXURE A

Facility Number: 1612
Date of Issue: 11 July 2016
Expiry Date: 10 July 2021

ITEM	NOMINAL RANGE	NOMINAL FREQUENCY	CALIBRATION AND MEASUREMENT CAPABILITY EXPRESSED AS AN UNCERTAINTY (±)
1.2	**DC voltage meters**		
1.2.1	Very low values (≤ 1 mV) Digital multimeter, nano voltmeters		
	0 mV 1 mV		10 nV $5 \cdot 10^{-5} \cdot U$
1.2.2	Intermediate values (> 1 mV to 1100 V) Digital multimeters, nano voltmeters		
	1 mV to 10 mV		$5 \cdot 10^{-5} \cdot U$
	10 mV to 100 mV		$2 \cdot 10^{-5} \cdot U$
	0,1 V to 1 000 V		$1 \cdot 10^{-5} \cdot U$
2	**DC resistance**		
2.1	**DC resistance standards and sources.**		
2.1.1	Low values (≤ 1 Ω) Fixed resistor, resistance box, multifunction calibrator		
	10 µΩ to 1 mΩ		$7 \cdot 10^{-6} \cdot R$
	1 mΩ to 10 mΩ		$2 \cdot 10^{-6} \cdot R$
	10 mΩ to 100 mΩ		$2 \cdot 10^{-6} \cdot R$
	100 mΩ to 1 Ω		$1 \cdot 10^{-6} \cdot R$
2.1.2	Intermediate values (> 1 Ω to 1 MΩ) Fixed resistor, resistance box, multifunction calibrator		
	1 Ω to 10 Ω		$2 \cdot 10^{-7} \cdot R$
	10 Ω to 100 Ω		$3 \cdot 10^{-7} \cdot R$
	100 Ω to 1 kΩ		$4 \cdot 10^{-7} \cdot R$
	1 kΩ to 10 kΩ		$5 \cdot 10^{-7} \cdot R$
	10 kΩ to 100 kΩ		$2 \cdot 10^{-6} \cdot R$
	100 kΩ to 1 MΩ		$4 \cdot 10^{-6} \cdot R$
2.1.3	High values (> 1 MΩ) Fixed resistor, resistance box, multifunction calibrator		
	1 MΩ to 10 MΩ		$6 \cdot 10^{-6} \cdot R$
	10 MΩ to 100 MΩ		$6 \cdot 10^{-6} \cdot R$
	100 MΩ to 1 GΩ		$9 \cdot 10^{-6} \cdot R$
	1 GΩ to 10 GΩ		$7 \cdot 10^{-5} \cdot R$
	10 GΩ to 100 GΩ		$3 \cdot 10^{-4} \cdot R$
	100 GΩ to 1 TΩ		$2 \cdot 10^{-3} \cdot R$

Original date of accreditation: 01 September 2005

Page 2 of 9

The CMC, expressed as an expanded uncertainty of measurement, is stated as the standard uncertainty of measurement multiplied by a coverage factor k = 2, corresponding to a confidence level of approximately 95%

Accreditation Manager

ANNEXURE A

Facility Number: 1612
Date of Issue: 11 July 2016
Expiry Date: 10 July 2021

ITEM	NOMINAL RANGE	NOMINAL FREQUENCY	CALIBRATION AND MEASUREMENT CAPABILITY EXPRESSED AS AN UNCERTAINTY (±)
2.2	**DC resistance meters**		
2.2.1	Low values (≤ 1 Ω) Micro-ohm meter, multimeter, resistance bridge		
	0 Ω		0,3 µΩ
	1 Ω		$1 \cdot 10^{-6} \cdot R$
2.2.2	Intermediate values (> 1 Ω to 1 GΩ) ohm meter, multimeter, resistance bridge		
	10 Ω to 100 Ω		$2 \cdot 10^{-6} \cdot R$
	100 Ω to 1 kΩ		$3 \cdot 10^{-6} \cdot R$
	1 kΩ to 10 kΩ		$3 \cdot 10^{-6} \cdot R$
	10 kΩ to 100 kΩ		$3 \cdot 10^{-6} \cdot R$
	100 kΩ to 1 MΩ		$5 \cdot 10^{-6} \cdot R$
	1 MΩ to 10 MΩ		$7 \cdot 10^{-6} \cdot R$
	10 MΩ to 100 MΩ		$9 \cdot 10^{-6} \cdot R$
	100 MΩ to 1 GΩ		$2 \cdot 10^{-5} \cdot R$
2.2.3	High values (> 1 GΩ) , multimeter, multifunctional transfer std teraohmmeter		
	1 GΩ to 10 GΩ		$7 \cdot 10^{-5} \cdot R$
	10 GΩ to 100 GΩ		$3 \cdot 10^{-4} \cdot R$
	100 GΩ to 1 TΩ		$2 \cdot 10^{-3} \cdot R$
3	**DC current (up to 100A)**		
3.1	**DC current sources.**		
3.1.1	Low values (≤ 0,1 mA) Current generator, multifunction calibrator.		
	0,1 µA to 1 µA	DC	$2 \cdot 10^{-4} \cdot I$
	1 µA to 10 µA	DC	$5 \cdot 10^{-5} \cdot I$
	10 µA to 100 µA	DC	$3 \cdot 10^{-5} \cdot I$
3.1.2	Intermediate values (> 0,1 mA to 20 A) Current generator, multifunction calibrator		
	0,1 mA to 1 mA	DC	$3 \cdot 10^{-5} \cdot I$
	1 mA to 10 mA	DC	$3 \cdot 10^{-5} \cdot I$
	10 to 100 mA	DC	$3 \cdot 10^{-5} \cdot I$
	0,1 A to 1 A	DC	$3 \cdot 10^{-5} \cdot I$
	1 A to 20 A	DC	$3 \cdot 10^{-5} \cdot I$
3.1.3	High values (> 20 A to 100 A) Current generator.		
	20 A to 100 A	DC	$2 \cdot 10^{-4} \cdot I$

The CMC, expressed as an expanded uncertainty of measurement, is stated as the standard uncertainty of measurement multiplied by a coverage factor k = 2, corresponding to a confidence level of approximately 95%

Accreditation Manager